

Characterization of snowfall  
using ground-based  
passive and active remote sensors

Inaugural-Dissertation  
zur Erlangung des Doktorgrades  
der Mathematisch-Naturwissenschaftlichen Fakultät  
der Universität zu Köln

vorgelegt von  
Stefan Kneifel  
aus Wolfratshausen

Köln 2011

Berichterstatter:

Prof. Dr. S. Crewell  
Prof. Dr. C. Simmer  
Prof. Dr. A. Illingworth

Tag der mündlichen Prüfung: 21.11.2011

*How full of the creative genius is the air  
in which these are generated!  
I should hardly admire more if real stars  
fell and lodged on my coat.  
Nature is full of genius, full of the divinity;  
so that not a snowflake escapes its fashioning hand.  
Nothing is cheap and coarse, neither dewdrops nor snowflakes.*

Henry David Thoreau (1817 – 1862)



# Abstract

Snowfall is a key quantity in the global hydrological cycle and has an impact on the global energy budget as well. In sub-polar and polar latitudes, snowfall is the predominant type of precipitation and rainfall is often initiated via the ice phase. Currently, the spatial distribution of snowfall is poorly captured by numerical weather prediction and climate models. In order to evaluate the models and to improve our understanding of snowfall microphysics, global observations of snowfall are needed. This can only be obtained by space-borne active and passive remote sensors. In order to be able to penetrate even thick snow clouds, sensors operating in the microwave frequency region are favoured. The challenge for snowfall retrieval development lies first in the complexity of snowfall microphysics and its interactions with liquid cloud water. Secondly, comprehensive knowledge is needed about the interaction of electromagnetic radiation with snowfall in order to finally relate the radiative signatures to physical quantities.

A general advantage of ground-based observations is that simultaneous measurements of in-situ and remote sensing instruments can be obtained. Such a six-month dataset was collected within this thesis at an alpine site. The instrumentation included passive microwave radiometers that covered the frequency range from 22 up to 150 GHz as well as two radar systems operating at 24.1 and 35.5 GHz. These data were complemented by optical disdrometer, ceilometer and various standard meteorological measurements.

State-of-the-art single scattering databases for pristine ice crystals and complex snow aggregates were used within this thesis to investigate the sensitivity of ground-based passive and active remote sensors to various snowfall parameters such as vertical snow and liquid water distribution, snow particle habit, snow size distribution and ground surface properties. The comparison of simulations with measurements within a distinct case study revealed that snow particle scattering can be measured with ground-based passive microwave sensors at frequencies higher than 90 GHz. Sensitivity experiments further revealed that ground-based sensors have clear advantages over nadir measuring instruments due to a stronger snow scattering signal and lower sensitivity to variable ground surface emissivity. However, passive sensors were also found to be highly sensitive to liquid cloud water that was frequently observed during the entire campaign. The simulations indicate that the uncertainties of sizes distribution and snow particle habit are not distinguishable with a passive-only approach.

In addition to passive microwave observations, data from a low-end radar system that is commonly used for rainfall were investigated for its capabilities to observe snowfall. For this, a snowfall specific data processing algorithm was developed and the re-processed data were compared to collocated measurements of a high-end cloud radar. If the focus can be narrowed down to medium and strong snowfall within the lowest 2–3 km height, the reflectivity and fall velocity measurements of the low-end system agree well with the cloud radar. The cloud radar dataset was used to estimate the uncertainty of retrieved snowfall rate and snow

accumulation of the low-end system. Besides the intrinsic uncertainties of single-frequency radar retrievals the estimates of total snow accumulation by the low-end system lay within 7% compared to the cloud radar estimates.

In a more general approach, the potential of multi-frequency radar systems for derivation of snow size distribution parameters and particle habit were investigated within a theoretical simulation study. Various single-scattering databases were combined to test the validity of dual-frequency approaches when applied to non-spheroid particle habits. It was found that the dual-frequency technique is dependent on particle habit. It could be shown that a rough distinction of snow particle habits can be achieved by a combination of three frequencies. The method was additionally tested with respect to signal attenuation and maximum particle size.

The results obtained by observations and simulations within this thesis strongly suggest the further development of simultaneous ground-based in-situ and remote sensing observations of snowfall. Extending the sensitivity studies of this study will help to define the most suitable set of sensors for future studies. A combination of these measurements with a further development of single-scattering databases will potentially help to improve our understanding of snowfall microphysics.

# Zusammenfassung

Schneefall spielt eine herausragende Rolle im globalen Wasserkreislauf und hat ebenfalls einen Einfluß auf die globale Energiebilanz. In den polaren Regionen ist Schneefall die dominierende Niederschlagsart. Ebenso wird Regen gerade in mittleren Breiten größtenteils über die Eisphase gebildet. Die tatsächliche räumliche Schneefallverteilung wird von aktuellen Wettervorhersage- und Klimamodellen nur sehr unzureichend wiedergegeben. Um diese Modelle zu evaluieren und um unser Verständnis der Schneemikrophysik zu verbessern, sind globale Beobachtungen unabdingbar. Dies kann nur von Satelliten aus mit aktiven und passiven Fernerkundungssensoren erreicht werden. Hierbei bieten sich gerade Sensoren im Mikrowellenbereich an, da diese selbst dicke Schneewolken durchdringen können. Die große Herausforderung für die Ableitung von Schneefallparametern aus solchen Messungen besteht in der komplexen Schneemikrophysik und den Wechselwirkungen von Schnee- und Eipartikeln mit flüssigem Wolkenwasser. Um schließlich aus den gemessenen Werten auf physikalische Größen schließen zu können, sind desweiteren umfassende Kenntnisse über die Wechselwirkung elektromagnetischer Strahlung mit den Schneepartikeln nötig.

Bodengebundene Stationen erlauben simultane Messungen mit in-situ und Fernerkundungsinstrumenten. Ein solcher sechsmonatiger Datensatz wurde während der hier vorgestellten Doktorarbeit an einer Messstation in den Alpen aufgenommen. Die Instrumentierung schloß sowohl passive Mikrowellenradiometer, im Frequenzbereich zwischen 22 bis 150 GHz, als auch zwei Radarsysteme bei 24.1 und 35.5 GHz ein. Ergänzt wurden diese Messungen noch durch Beobachtungen von optischen Distrometern, einem Ceilometer sowie verschiedener meteorologischer Standardgrößen.

Im Rahmen der Doktorarbeit wurden die momentan aktuellsten Streudatenbanken zur Simulation sowohl einzelner Schneekristalle, als auch komplexer Schneeaggregate eingesetzt. Damit wurden die Sensitivitäten der bodengebundenen passiven und aktiven Fernerkundungsmessungen gegenüber den verschiedenen Schneefallparametern untersucht. Dazu gehören im Besonderen die vertikale Verteilung von flüssigem Wolkenwasser und Schneegehalt, die Schneepartikelform, die Schneegrößenverteilung und strahlungsrelevante Eigenschaften der Erdoberfläche. Im Rahmen einer Fallstudie wurden Strahlungstransportsimulationen und Messungen verglichen. Dieser Vergleich ergab, dass Streusignale verursacht durch Schneefall bei Frequenzen oberhalb von 90 GHz mit bodengebundenen Mikrowellensensoren meßbar sind. Zusätzliche Sensitivitätsexperimente zeigten klare Vorteile bodengebundener Messungen gegenüber Messungen in Richtung des Erdbodens — beispielsweise von Satelliten aus. Zum einen ist das Schnee-Streusignal deutlich stärker, und zum anderen sind bodengebundene Messungen deutlicher weniger von variablen Bodenemissivitäten beeinflusst. Die Ergebnisse dieser Studie zeigen jedoch ebenso deutlich, dass passive Mikrowellenmessungen äußerst sensitiv gegenüber vorhandenem atmosphärischem Flüssigwasser sind, welches überraschend häufig in Schneewolken während des Messzeitraums gemessen wurde. Mit Hilfe

der Simulationsrechnungen konnte weiterhin gezeigt werden, dass sich die Unsicherheiten durch Schneegrößenverteilung und Schneepartikelform im gleichen Maße auf die Messungen auswirken, und somit diese sich mit passiven Methoden allein nicht unterscheiden lassen.

Zusätzlich zu den passiven Mikrowellenbeobachtungen wurden die Messungen eines einfachen Radarsystems, welches üblicherweise für Regen eingesetzt wird, auf sein Potenzial hinsichtlich Schneefallbeobachtung untersucht. Dazu wurde eine spezielle Schneefalldatenprozessierung entwickelt und die neu prozessierten Messwerte mit den zeitgleich gemessenen Daten eines leistungsfähigen Wolkenradars verglichen. Der Vergleich zeigte, dass wenn der Beobachtungsfokus auf die bodennahen Schichten unterhalb von ca. 2–3 km Höhe und auf mittlere bis starke Schneefallereignisse eingeschränkt werden kann, die Radarreflektivitäten und die gemessenen Fallgeschwindigkeiten des einfachen Systems gut mit dem Wolkenradar übereinstimmen. Mit Hilfe der Wolkenradardaten konnte ebenfalls abgeschätzt werden, welche Auswirkungen die begrenzte Sensitivität des einfacheren Systems auf die messbaren Schneefallraten, und damit auf die gesamt akkumulierte Schneefallmenge hat. Abgesehen von systembedingten Unsicherheiten, welche bei Ableitungen der Schneefallrate mittels eines Einfachfrequenzradars entstehen, wich die abgeleitete akkumulierte Schneemenge nur um etwa 7 % von der des Wolkenradars ab.

Im letzten Teil der Doktorarbeit wurde das Potenzial von Mehrfrequenzradarsystemen für die Ableitung von Schneegrößenverteilung und Schneepartikelform mit Hilfe einer Simulationstudie untersucht. Verschiedene Streudatenbanken wurden kombiniert, um die Gültigkeit des sog. Zweifrequenzansatzes zu untersuchen, welcher bislang auf Simulationen mit kugelförmigen oder ellipsoiden Partikelformen basierte. Es zeigte sich, dass dieses Verfahren durchaus abhängig von der Schneepartikelform ist, wenn komplexe Schneepartikel in die Betrachtung miteinbezogen werden. Mit einer Kombination von drei Frequenzen konnten jedoch verschiedene Schneepartikelklassen deutlich voneinander unterschieden werden. Die Methode wurde abschließend noch hinsichtlich ihrer Einsetzbarkeit bei Dämpfung des Radarsignals und verschiedener Schneepartikelgrößen untersucht.

Die Ergebnisse dieser Arbeit, basierend auf Beobachtungsdaten und Simulationsexperimenten, stellen klar heraus, dass simultane, bodengebundene Beobachtungen mittels in-situ und Fernerkundungsinstrumenten weiter entwickelt werden müssen. Eine Erweiterung der Sensitivitätsstudien dieser Arbeit kann dazu beitragen, die optimale Kombination von Sensoren zur Schneefallbeobachtung zu definieren. Ein solcher Messdatensatz zusammen mit weiterentwickelten Streudatenbanken, kann wesentlich dazu beitragen unser Verständnis der Schneefallmikrophysik zu verbessern.



# Contents

<b>1</b>	<b>Introduction</b>	<b>1</b>
1.1	Motivation . . . . .	1
1.2	State of the Art . . . . .	4
1.3	Focus of the present thesis . . . . .	9
<b>2</b>	<b>The TOSCA Campaign</b>	<b>13</b>
2.1	Passive microwave radiometers . . . . .	13
2.2	Radar systems . . . . .	16
<b>3</b>	<b>Snowfall Microphysics</b>	<b>21</b>
3.1	Snow size distribution . . . . .	21
3.2	Snow particle habit . . . . .	23
3.3	Mass – size relation . . . . .	27
3.4	Orientation . . . . .	29
<b>4</b>	<b>Radiative Transfer at Microwave Frequencies</b>	<b>31</b>
4.1	Basic concepts . . . . .	31
4.2	Absorption and thermal emission . . . . .	33
4.3	Scattering . . . . .	35
4.4	Radiative transfer equation for a plane–parallel atmosphere . . . . .	40
4.5	Effective radar reflectivity factor $Z_e$ and attenuation . . . . .	41
<b>5</b>	<b>The Radiative Transfer Model RT3 and the Definition of Input Fields</b>	<b>43</b>
5.1	Surface emissivity . . . . .	44
5.2	Thermal emissions by gases . . . . .	44
5.3	Liquid water emission . . . . .	45
5.4	Snow scattering . . . . .	45
<b>6</b>	<b>Passive Remote Sensing of Snowfall</b>	<b>55</b>
6.1	Case study: 08. February 2009 . . . . .	56
6.2	Statistical analysis of $T_B$ enhancement . . . . .	66
6.3	Outlook towards frequencies larger than 150 GHz . . . . .	68
<b>7</b>	<b>Active Remote Sensing of Snowfall between 20 and 95 GHz</b>	<b>71</b>
7.1	Intercomparison: Cloudradar MIRA36 vs. MRR during snowfall . . . . .	71
7.2	Single– and dual– frequency approach for snowfall . . . . .	84
7.3	Triple – frequency approach . . . . .	88

<b>8</b>	<b>Conclusions and Outlook</b>	<b>95</b>
8.1	Conclusions . . . . .	95
8.2	Outlook . . . . .	97
	<b>List of Acronyms</b>	<b>101</b>
	<b>Bibliography</b>	<b>103</b>

# Chapter 1

## Introduction

### 1.1 Motivation

Frozen water in the atmosphere influences the global energy budget by changing the radiative properties of clouds, as well as the global water cycle, within the complex precipitation formation process. While the small particles “floating” in a cloud are commonly denoted as cloud ice, the precipitating particles are usually called snow or graupel<sup>1</sup> (*Waliser et al., 2009*).

A quantitative estimate of the percentage of global precipitation falling as snow is just recently available with the upcoming of suitable satellite sensors. Earlier studies have mostly been based on ship observations (*Petty, 1995*). Those studies provided global frequency maps of snowfall that revealed snowfall to be a common precipitation type over the northern and southern oceans at latitudes higher than  $40^\circ$ . For a global estimate of snowfall, however, satellite observations are inevitable. Unlike rainfall, quantitative estimates of global snowfall amount can only be obtained by highly sensitive active and passive systems. The most comprehensive insight into global cloud ice and snowfall distribution is provided by the Cloud Profiling Radar (CPR) on CloudSat (*Stephens et al., 2002*), which was launched in 2006. Using a one year set of the CloudSat data, the first quantitative estimate of snowfall rate (SR) on a global basis was provided by *Liu (2008b)*. While the frequency distribution of snowfall agrees well with the earlier ship observations, this study reveals the predominance of snowfall compared to the total amount of precipitation at latitudes higher than  $\sim 40^\circ$  with slight differences between northern and southern hemisphere (Fig. 1.1). The maximum SR has been estimated to 1 mm/day at the northern and 2 mm/day in the southern hemisphere. In a similar study by *Kulie and Bennartz (2009)* the average global SR is estimated to be about  $0.28 \text{ mmh}^{-1}$ , while the authors note that snowfall retrievals are still affected by large uncertainties. By analyzing histograms of SR for different climatic regions they further found that the majority of snowfall events reveal light and medium SR in the range of  $0.05 - 1.0 \text{ mmh}^{-1}$ . The lowest SR were found over polar regions, particularly over Antarctica. These results implicate that for an accurate estimate of global snowfall amount, remote sensing instrument with a high sensitivity to capture even light snowfall events and shallow cloud structures are required.

Snowfall reaching the ground surface is presumably for most people of major relevance, due to its manifold impacts on public life: Modern transport infrastructure is highly de-

---

<sup>1</sup>Hail is neglected in this context due to its minor relevance for global precipitation.

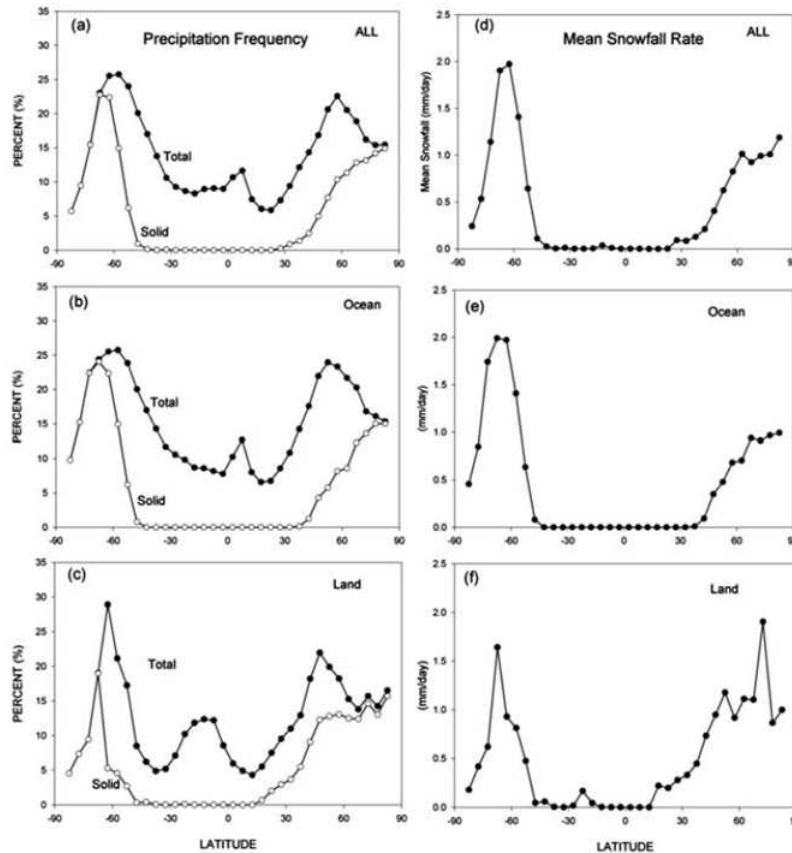


**Figure 1.1:** (left) Zonally averaged total (line with filled circles) and solid (line with open circles) precipitation (snowfall) and (right) mean snowfall rate for (top) all surfaces, (middle) over ocean, and (bottom) over land observations. The distinction between solid and liquid precipitation is based on near-surface temperature. [extracted from *Liu (2008b)*]

pendent on accurate prediction of hazardous weather events — like heavy snowfall — that can cause high economic costs. Snow isolates and therefore protects plants from cold air temperatures. The amount of snow may thus influence harvest time in agriculture since it hampers the warming of the soil in springtime. Particularly in mountainous regions like the Alps, accurate prediction and observation of snow accumulation are relevant not only for tourism but also for avalanche warning services. The amount of accumulated snowfall over land has also an important reservoir-function in the hydrological cycle. If melting occurs, the estimated snow accumulation is a crucial parameter for water resource management and flood prediction.

Besides the more regional impacts, surface snowfall influences the global hydrological and energy cycle. Snowfall is a key quantity in the mass balance of the polar ice caps. A comprehensive understanding of snowfall is thus essential to improve climate model predictions. Snowfall has further been found to influence the global oceans: As the predominant type of precipitation at high latitudes (Fig. 1.1) snowfall cools and freshens the upper water layers. Thus, it is assumed that snowfall can modify ocean surface buoyancy and deep water formation (*Liu and Curry, 1997*). As mentioned above snow covered surfaces isolate the underlying surface from the air above. In this respect, accurate prediction of snow cover — which is

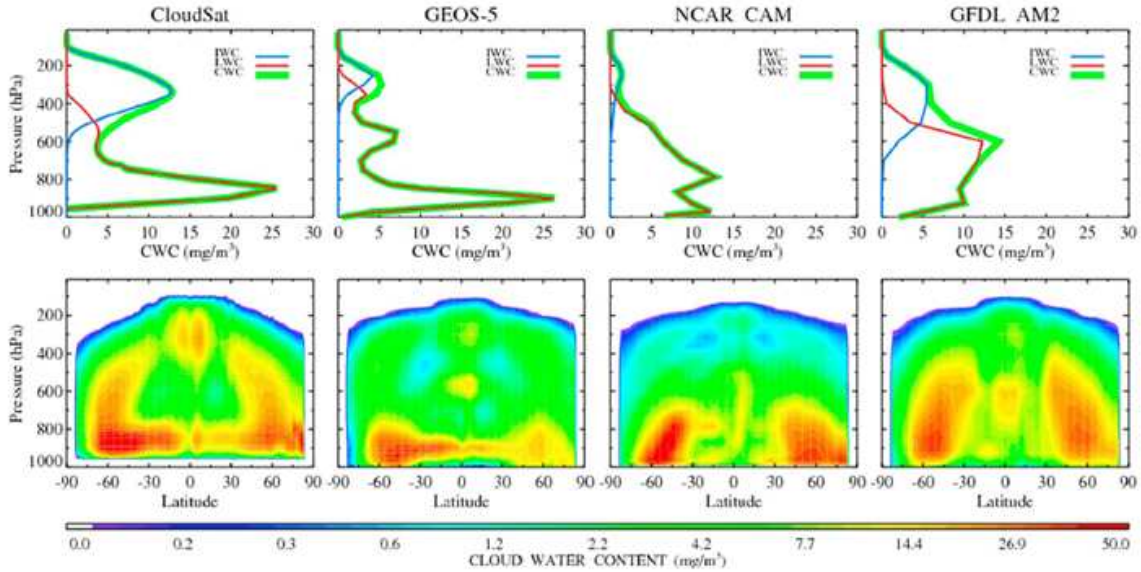


**Figure 1.2:** (top) Tropical-averaged and (bottom) zonal-averaged annual mean cloud water content (CWC in  $\text{mgm}^{-3}$ ) profiles from CloudSat (left) and three model simulations [extracted from *Su et al. (2011)*].

closely connected to accurate snowfall estimates — plays an important role in the potential warming of permafrost soils in a warmer climate (Chapter 4, *IPCC, 2007*).

A surface covered with snow has a higher albedo<sup>2</sup> (typically 0.8 to 0.9 for fresh fallen snow) than snow-free surfaces. Large areas covered by snow thus alter the global energy budget by reflecting more energy back into the atmosphere. The higher albedo of snow-covered surfaces results in slower warming of the air above and therefore yields in different heating rates at the lowest atmospheric layers (e.g. *Groisman et al., 1994*). A quantitative analysis of the global impact of terrestrial snow cover on temperature and atmospheric dynamics is given by *Vavrus (2007)*: In an experiment with a global climate model (GCM) all snowfall over land was converted into its liquid water equivalent before reaching the surface. The simulation without snow cover produced 5 K higher mean-annual surface air temperatures over North America and Eurasia and an 8–10 K rise in temperatures during wintertime, compared to the control run. The absence of snow on the earth’s surface also affected upper-air circulation patterns and the frequency of extreme weather events. Different snowfall amounts resulting in varying snow cover have also an impact on large scale precipitation systems: The Eurasian snow cover in the springtime has been found to be linked to the strength of Asian summer monsoon as well as to the atmospheric pressure field over Northern America (*Barnett et al., 1988*).

In addition to the various impacts of surface snowfall for regional and global climate, understanding snowfall also helps understanding the process of the formation of “cold cloud” rainfall. This rain formation process is particularly common for mid and high latitudes. The cloud region above the freezing level is characterized by exceedingly complex interactions of cloud liquid water droplets, floating ice particles and sedimenting snow. While first attempts have been made towards more sophisticated representation of ice microphysics in

<sup>2</sup>Albedo is the ratio of reflected to incoming (solar) radiation.

numerical weather prediction (NWP) models (*Lynn et al., 2005; Seifert and Beheng, 2006*), these complex mechanisms are currently still poorly represented in global climate models. In many of those models snowfall is neglected or only a diagnostic variable. Consequently, the spatial distribution and global average amount of cloud ice predicted by climate models has been found to deviate dramatically from satellite observations (*Waliser et al., 2009; Su et al., 2011*). The disregard of snowfall can have significant effects on the radiation balance as investigated by (*Waliser et al., 2011*). Their analysis of CloudSat observations (Fig. 1.2) reveals a high concentration of ice and snow particles at high latitudes as well as in equatorial regions at heights above 500 hPa. This high concentration of ice in the equatorial region is associated with anvils of mesoscale convective systems. The authors found that an exclusion of precipitating snow and graupel can result in an underestimation of reflective shortwave flux at the top of the atmosphere. Additionally, the vertical shortwave and longwave heating rates can deviate up to 10 %, particularly in the most convective areas.

## 1.2 State of the Art

Given the enormous uncertainties in the prediction of snowfall in NWP and climate models and then again, the importance of snowfall for the hydrological cycle and global energy budget, global and reliable observations of snow water distribution are essential. Accurate surface-based in situ measurements of snowfall are only sporadically available around the globe; most operational stations only provide cumulative amounts of snowfall over the range of hours. Even for these measurements many problems, such as wind-induced error, have been identified to be severe (*Sevruk et al., 2009*). In-situ measurements within ice and snow clouds provided by airborne observations give an insight into microphysical processes and the variability of particle habits, amount of super-cooled liquid water and particle size distributions for different cloud systems (e.g. *Heymsfield et al., 2002; Field et al., 2005*). However, such observations can only deliver “snapshots” with extremely limited spatial and temporal extent. As a matter of fact, remote sensing methods are the only means suited for the purpose of global snowfall data because they are able to provide continuous observations with high temporal resolution and broad spatial coverage.

### Common remote sensing techniques

While visible and infrared satellite remote sensing observations have been available for decades and also have been widely used to investigate cirrus clouds, they show poor accuracy for clouds with high amounts of integrated ice water path (IWP) (e.g. *Eliasson et al., 2011*). In fact, visible and infrared techniques tend to be most sensitive to the cloud top because of their intrinsic incapability of sounding deeply within the cloud structure (Fig. 1.3). Observations in the microwave (MW) region, however, usually defined as the frequency range between 0.3 and 300 GHz (i.e. wavelength of 1 m to 1 mm), are even able to penetrate a cloudy atmosphere. Frequencies along the wings of characteristic absorption lines are utilized to derive profile information of temperature and water vapor. Column integrated amounts of water vapor and liquid water can be derived due to their frequency dependent emissions. Within atmospheric window regions, i.e. frequency regions with comparably low atmospheric optical thickness, scattering effects of ice and snow particles, which are related to the total ice water content, can be observed. For this reason, many efforts have focused on passive and active MW

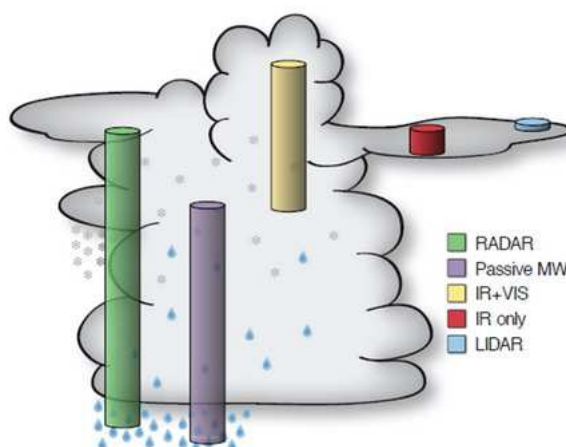


**Figure 1.3:** Schematic figure of a thick cloud. The columns indicate approximately where the different remote sensing techniques are sensitive [extracted from *Eliasson et al. (2011)*]

techniques for the observation of snowfall. Yet, only for the last few years observational data have been made available on a global scale.

Numerous remote sensing methods for deriving rainfall from satellite sensors using passive microwave radiometry have been developed over the years and are being routinely applied (e.g. *Kummerow et al., 1996; Weng et al., 2003*). A breakthrough for retrieving rainfall rates in the tropical regions was the launch of the Tropical Rainfall Measurement Mission (TRMM) satellite in 1997, which combines an active precipitation radar operating at 13.8 GHz and passive microwave sensors at 10.7, 19.4, 21.3, 37.0 and 85.5 GHz (*Iguchi et al., 2000*). In contrast, remote sensing methods for deriving snowfall are much less sophisticated and suffer from large uncertainties.

Since 2006 vertically resolved reflectivity data from the nadir-viewing 94 GHz radar CPR on the CloudSat (*Stephens et al., 2002*) satellite are available. In addition to rainfall observation the high sensitivity of the CPR allows deriving vertical profiles of frozen hydrometeor content. Passive observations (commonly shown as brightness temperatures,  $T_B$ ) at atmospheric window channels (e.g. 89 and/or 150 GHz) are provided by the Special Sensor Microwave Imager (SSM/I) flown on the Defense Meteorological Satellite Program (DMSP), the Microwave Humidity Sounder (MHS) onboard the NOAA 18 and MetOp-A satellites, the Advanced Microwave Sounding Units (AMSU-A/B) onboard the NOAA 15-17 satellite and the Advanced Microwave Scanning Radiometer EOS (AMSR-E) onboard the NASA AQUA satellite.

### Basic issues of snowfall retrievals

In fact, any snowfall retrieval based on passive, active or combined sensors is dependent on assumptions about crystal habit and snow size distribution (SSD) that have a large impact on the radiative properties and hence the quality of the retrieval. Following the argumentation given in *Petty and Huang (2010)*, two equally essential parts required for any snowfall retrieval approach can be specified: 1) A detailed and validated statistical description of the cloud microphysics is needed including the distribution of liquid water, snow particle sizes, habits and densities under varying atmospheric conditions; 2) The microphysical characteristics have

to be transferred into electromagnetic properties which allows to relate the physical quantities to the measured variables like radar reflectivity factor or  $T_B$ . While significant progress has been made regarding 2) there is still a lack of observations leading to large uncertainties for the requirement 1). It has to be considered that for the development of e.g. temperature and humidity retrievals a comprehensive global dataset of radio soundings and reanalyzes from NWP models exist. In contrast, in-situ measurements of vertical profiles of liquid and snow water as well as particle size distribution and particle habits are still rare. Existing datasets are mostly based on aircraft observations (e.g. *Heymsfield et al., 2002; Field et al., 2005*) however, suffering from the aforementioned problem of limited spatial and temporal coverage. Recently, existing aircraft in-situ datasets have been analyzed and found to contain spurious large amounts of small particles, while larger snow particles are underestimated (*Korolev and Isaac, 2005; Field et al., 2006; Korolev et al., 2011*). The effect has been explained by shattering of ice particles at the housing of the in-situ (mostly optically) probes which raises the question how reliable existing aircraft in-situ datasets are. NWP models are currently not an alternative to in-situ observations since they have been found to poorly represent spatial fields of ice and snow (e.g. *Reitter et al., 2011*) and do usually contain only rather simplified parameterizations of snow particle habit and SSD.

### **Snow particle habit and scattering properties**

The development of realistical snow particle models mentioned in point 2) is further dependent on the observational data summarized in point 1): A database of in-situ observations of various clouds is needed to derive e.g. realistical ice particle models. Such particle models can then be utilized to derive their specific scattering properties. Currently, existing scattering databases are under rapid development; recent progress in simulation of complex habits is mainly due to increasing available computational resources. In the last decades, it was common to use spheroids composed of solid ice or an ice-air mixture (“soft sphere”) (e.g. *Skofronick-Jackson et al., 2003; Hogan et al., 2006*) which allowed to efficiently compute scattering properties with Mie theory (Section 4.3.2). With the increase of available computational power, several efforts have been made to replace spherical approximations by more realistical ice crystals. The majority of these crystals were idealized and symmetrical (pristine) crystals such as hexagonal columns, plates, rosettes or dendrites (*Liu, 2004; Evans et al., 2005; Seo and Liu, 2005; Noh et al., 2006; Kim, 2006; Hong, 2007a; Grecu and Olson, 2008*). Ground-based and airborne observations, however, revealed (e.g. *Heymsfield et al., 2002; Brandes et al., 2007*) that natural snow is dominated by non-pristine particles and crystal aggregates. The maximum size range in most particle models was limited to 5–10  $\mu\text{m}$  while in-situ observations indicate a maximum size of 1–2  $\text{cm}$  (*Brandes et al., 2007; Kneifel et al., 2010*). These particles are especially relevant for radar applications since radar quantities are particularly sensitive to large particles. Even a few large particles in the observational volume have a significant influence on the radar signal. Consequently, first studies started quiet recently to investigate the scattering properties of large aggregate snowflakes consisting of fractals (*Ishimoto, 2008; Tyynelä et al., 2011*) or aggregates of pristine crystals like dendrites or needles (*Petty and Huang, 2010; Botta et al., 2010*). Even if there remain large uncertainties about the most appropriate particle habit model, the spheroid particle models have thoroughly been found to be incapable to represent scattering parameters of snow particularly with regard to its wavelength dependence and the backscatter-extinction ratio.



## Snow size distribution

Besides the particle habit which intrinsically includes the particle's density or mass–size relation, the SSD within a given volume is another critical parameter that needs to be specified. Analyses of several airborne datasets revealed that cloud temperature can be utilized to determine parameters of the SSD (*Field et al.*, 2005, 2007). In general, the findings indicate higher concentrations of small particles at cold temperatures compared to warmer temperatures. This temperature dependent parameterization of the SSD was found to improve modelled cloud properties if compared to fixed SSD parameterizations (e.g. *Böhme et al.*, 2011). For snowfall sampled at the ground it has been found that the *Field* parameterization tends to underestimate large snow particles (*Brandes et al.*, 2007; *Löhnert et al.*, 2011) which might be related to processes like sublimation of small crystals or continued aggregation below the cloud or — as mentioned before — due to shattering effects at the in-situ probes. Furthermore, the currently temperature dependent SSD parameterizations do not include a well known effect called secondary aggregation region which has been found between  $-10$  and  $-15$  °C (*Hobbs et al.*, 1974; *Hosler and Hallgren*, 1960; *Löhnert et al.*, 2011). In this temperature region supersaturation over ice with respect to liquid water reaches its maximum value (e.g. *Pruppacher and Klett*, 1997, 119 pp.) leading to effective diffusional growth of ice crystals from evaporating liquid water drops. Further, snow crystals within this temperature range are mostly of dendritic structure (e.g. *Libbrecht*, 2005) which leads to increasing sticking efficiency and thus larger aggregates. It can be expected that further development of the temperature dependent SSD including e.g. the secondary aggregation region will increase the accuracy of SSD parameterizations.

## Super-cooled liquid water

Observations of snow (e.g. *Hiley et al.*, 2011; *Löhnert et al.*, 2011) and ice clouds (e.g. *Boudala et al.*, 2004) revealed the frequent presence of super-cooled liquid water (SLW) — i.e. liquid water below  $0$  °C — that can be found at temperatures down to  $-37$  °C before spontaneous homogeneous freezing occurs. Particularly higher MW frequencies ( $>90$  GHz) that are used for snowfall retrievals are affected by SLW due to its increasing emissivity with frequency. Emission from SLW can partly mask snow scattering received by passive sensors while it also contributes to the total attenuation of radar signals — especially at increasing frequencies (e.g. the 94 GHz CPR at CloudSat). For a correct treatment of SLW the vertical profile of liquid water content (LWC) is needed in order to account for the temperature dependence of liquid water emission. However, even with a perfect knowledge of the LWC profile an accurate radiative transfer is difficult due to the still poorly known refractive index of SLW at MW frequencies (*Mätzler*, 2006, p. 431-455). The different refractive index models (e.g. *Ray*, 1972; *Liebe et al.*, 1991; *Stogryn et al.*, 1995; *Ellison*, 2007) are based on measurements in the positive temperature region. Thus, the values for temperatures below freezing are extrapolations except for single measurements at specific frequencies (*Bertolini et al.*, 1982). The uncertainties of refractive index models have been identified to be one of the major sources of uncertainties in retrievals of SLW especially if frequencies  $\geq 90$  GHz are considered (*Cadeddu and Turner*, 2011).

### Radar snowfall retrievals

Vertical profiles of snow cloud properties like snow water content (SWC) or snowfall rate (SR) have been usually derived using single frequency radars. Several recent studies (*Liu*, 2008b; *Kulie and Bennartz*, 2009; *Hiley et al.*, 2011) investigated the sensitivity of single frequency spaceborne radar retrievals to snow particle model and SSD parameters. These studies show that derived SR from single frequency radar observations exhibit a large range of uncertainty caused largely by the lack of knowledge of snow microphysical parameters. Derived SR uncertainties from single frequency radar data generally exceed 50–75 % depending on the microphysical assumptions employed. An improvement in deriving snow quantities by radar can be achieved using a dual frequency approach (*Matrosov*, 1998). For ice and mixed-phase clouds, several studies analyzed collocated in-situ and radar measurements and revealed clear improvements obtained by using dual frequency techniques (*Gosset and Sauvageot*, 1992; *Hogan et al.*, 2000; *Heymsfield et al.*, 2008). Usually the frequencies are chosen with one frequency in the Rayleigh scattering regime (4.3.1) (e.g., S-, C-, X-band) and the other in the Mie regime (4.3.2) (e.g., K<sub>a</sub>-, W-band). Various studies have used soft spheres to generate representative scattering properties of snow particles (*Matrosov*, 1992; *Liao et al.*, 2005, 2008). These dual-frequency investigations found a simple power law relation between the characteristic size of the SSD and the logarithmic reflectivity difference, also known as the dual wavelength ratio (DWR). This power law relation is almost independent of snow density. In an attempt to develop more realistic models as proxies for falling snow, spheres have been replaced by spheroids (*Matrosov*, 1998, 2007) with a certain aspect ratio (i.e. ratio of shortest to longest dimension) to represent snow scattering properties. It has been shown that the dual frequency approach is a clear improvement over the single frequency approach. However, as *Matrosov* (1998) points out, a priori knowledge of the snow density is still needed as a tuning parameter in order to derive mass related quantities like SR. These studies revealed that while DWR is insensitive to snow density for spheres, it is sensitive to the chosen aspect ratio (*Matrosov et al.*, 2005a), thus highlighting the importance of ice habit for DWR calculations. Recent studies (*Sekelsky et al.*, 1999; *Gaussiat et al.*, 2003; *Yoshida et al.*, 2006) have also employed triple-wavelength approaches to distinguish different crystal shapes in ice clouds. In *Yoshida et al.* (2006), the authors focus on non-precipitating ice and mixed-phase clouds and consider comparably small ice spheres and hexagonal ice particles (maximum equivalent ice spheres radius of 500  $\mu\text{m}$ ) with varying aspect ratios. Their modelling results show that a distinction between different ice crystal habits is possible with the triple-frequency approach, however, a very high accuracy of the DWR measurements (better than 0.1 dB) is needed. Admittedly, this accuracy is rather unrealistic to achieve with current cloud radar systems.

### Passive-only and combined passive-active snowfall retrievals

While the radar derived hydrometeor content is related to the signal strength of the backscattered radar pulse from hydrometeors, the passive signal is related to the vertically integrated scattering properties of the entire atmospheric column. In a cloud-free case the passive signal received by a spaceborne sensor is dominated by atmospheric gases and the upwelling thermal radiation from the earth's surface. Thick ice and snow clouds have been found to significantly reduce the signal of the thermal radiation at frequencies greater than  $\sim 90$  GHz (e.g. *Katsumata et al.*, 2000; *Bennartz and Petty*, 2001; *Bennartz and Bauer*, 2003). This  $T_B$  depression is caused by the increase of scattering by frozen hydrometeors with increasing frequency and hydrometeor size. Thus, the scattering effects can be used to derive integrated

snow water path (SWP) (e.g. *Noh et al.*, 2006), but are not able to provide any information about vertical ice distribution. Additionally, those passive-only retrievals suffer from large uncertainties exceeding 60% (*Kulie et al.*, 2010) mainly related to the microphysical uncertainties mentioned above.

Passive MW measurements and radar reflectivities show different sensitivities to microphysical snowfall parameters: While the sensitivity of the reflectivity signal on particle habit strongly increases at frequencies larger than  $\sim 35$  GHz, the passive  $T_B$  are in general more sensitive to the SWP (e.g. *Petty and Huang*, 2010). A combination of both techniques can thus be expected to reduce retrieval uncertainties while including vertical profile information. Radar data and passive MW observations have been combined in several studies: *Noh et al.* (2006) and *Seo and Liu* (2005) applied different radar reflectivity – SWC relations based on single-frequency radar data to ground-based and airborne datasets. The SWC profiles have been utilized to build realistic a priori datasets (i.e. characteristic profile and variability of the snow quantities) and to finally develop snowfall retrievals based on passive MW observations for frequencies between 89 and 220 GHz. *Kulie and Bennartz* (2009) used CloudSat observations and a comprehensive set of snow particle habits to simulate passive observations between 36 and 157 GHz. The simulated  $T_B$  have been compared to collocated satellite observations which allowed excluding particle habits with systematic higher/lower scattering properties. The authors applied solely the *Field et al.* (2005) SSD parameterization and thus the influence of potential errors introduced by the SSD could not be discussed. Combined retrieval algorithms of SWC and characteristic snow particle size have been derived based on airborne radar and passive observations by *Skofronick-Jackson et al.* (2003) for tropical convective clouds and by *Greco and Olson* (2008) for snowstorms over the ocean. A clear result of these studies is that a significant improvement of snowfall retrievals can be obtained by combining passive and active MW observations using multiple frequencies. The retrievals are, however, still highly sensitive to the a priori data, the microphysical assumptions and the scattering models used for simulating  $T_B$  and radar reflectivities.

A key problem hampering the development of both better particle scattering models and snowfall retrievals is the lack of simultaneous in-situ observations of snowfall microphysics combined with measurements of radiative properties. While in-situ observations are impossible to obtain with satellite sensors, airborne in-situ observations are difficult to match with ground-based or other aircraft remote sensing data. Although ground-based observations can not provide broad spatial coverage they allow collecting long-term datasets of both remote sensing observations and in-situ measurements — at least for the lowest cloud layers. Thus, ground-based observations can help to further constrain and improve snowfall retrievals that can finally be applied to satellite sensors. Most analyses within this thesis are based on such a ground-based dataset collected at an alpine site which will be described in the following chapters.

### 1.3 Focus of the present thesis

The majority of combined remote sensing and in-situ observations of snowfall and snow clouds have been obtained by airborne sensors. Similarly, most snowfall retrievals have been developed for the downward looking observation geometry of airborne or spaceborne sensor. The overall question of the present study is which information content about snow clouds can be gained by ground-based MW remote sensing observations. In order to answer this question

passive and active remote sensors have been deployed together with in-situ instruments within the **T**owards an **O**ptimal estimation based **S**now **C**haracterizing **A**lgorithm (TOSCA) project during winter 2008/2009 at the “Umweltforschungsstation Schneefernerhaus” (UFS) in the Bavarian Alps.

The unique atmospheric conditions at the UFS together with the considerably large frequency range from 22 to 150 GHz covered by the deployed passive microwave radiometers (MWR) make it possible to analyse potential signatures of snowfall in passive MW measurements. Similar to the well known  $T_B$  depression found in downward looking measuring sensors an analogous  $T_B$  enhancement at ground-based high frequency MW observation is expected but has not been reported yet by other authors. The large set of additional sensors like e.g. ceilometer, cloud radar, in-situ sensors and nearby radiosonde ascents will be used within a case study to reconstruct the atmospheric state. This information is then combined with state-of-the-art scattering databases of realistical snow particle habits to simulate ground-based  $T_B$  at the considered frequencies. This allows to quantify the snow scattering effect and to compare the signatures with nadir measuring geometry. The simulation results will further be tested with respect to their sensitivity to snow particle habit, SSD parameters, ground surface emissivity and vertical liquid water distribution. Within a statistical analysis of the entire TOSCA time period it will be investigated whether the  $T_B$  enhancement remains a robust effect even if completely different snowfall events are considered. Based on the observational and simulation results it will be theoretically investigated which information can be gained from ground-based observations at higher MW frequencies up to 340 GHz that are already used e.g. for aircraft campaigns. Herein, specific attention will be given to the relation of liquid water emission and snow particle scattering.

The other major focus of this study is active MW remote sensing. In contrast to ground-based passive MW observations several studies already presented single and dual-frequency cloud radar observations of snowfall. Therefore, this study concentrates on two new aspects of active remote sensing of snowfall: The first aspect is motivated by the simultaneous measurements of a small low-power radar together with a high-end cloud radar during TOSCA. High power systems that need frequent maintenance are often not suitable for remote areas like e.g. mountainous regions or arctic environments. However, measurements of snowfall and snow cloud structure from those regions are of particular scientific relevance. Thus, it will be investigated what information content about snowfall can be obtained by a low-end system that is usually applied for rainfall measurements. Specific algorithms for snowfall observations will be developed and applied to the available measurements. From the simultaneous measurements of the cloud radar the sensitivity level of the low-end radar can be derived and compared with a clear-sky technique. The impact of the limitations of the low-end system on estimates of accumulated snow amount and snowfall rate will be explored using the long-term data from the high-end cloud radar together with different standard radar reflectivity – SR relations. The second aspect regarding active MW remote sensing is related to the important question which microphysical information can be gained from multi-frequency radar observation. Dual-frequency techniques have already been developed with help of spheroid particle scattering models and their ability to derive SSD parameters like the characteristic particle size has been demonstrated. In a first step this “classical” dual-frequency technique will be repeated with a set of non-spheroid particle models that have become available, quiet recently. With the various particle habits the dual-frequency techniques will be examined with respect to their applicability to non-spherical particle habits. The theoretical study will be further extended towards a third frequency in order to investigate whether a triple-frequency

approach can be utilized to distinguish between different particle habits.

### Outline of the thesis

The present thesis is structured as follows: In Chapter 2 the measurement site UFS and the TOSCA campaign will be described. The available observation time periods during snowfall are summarized and the deployed instruments will be described in detail with a special focus on the passive microwave radiometers and radar systems. A compact summary of the microphysical properties of snowfall that have the largest influence on radiative transfer, namely SSD, snow particle habit, mass–size relation and snow particle orientation, will be given in Chapter 3. The subsequent Chapter 4 introduces the reader to the basic concepts of radiative transfer at MW frequencies including the description of typical scattering regimes and variables which are needed for the remaining chapters. The radiative transfer model for simulating passive  $T_B$  as well as the definition of various input fields is described in detail in Chapter 5. The radiative transfer simulations are compared to measurements within a case study in Chapter 6. The comparison includes several sensitivity experiments with varying SSD parameters, particle habits, ground surface emissivities and vertical liquid water distribution. The case study is followed by a short statistical analysis of the snow scattering effect and will be closed with a discussion about the benefit that can be expected from passive observations at increasing frequencies between 150 and 340 GHz. In Chapter 7 the focus shifts to active remote sensing techniques. In the first part of Chapter 7 a comparison of a low–power radar system and a high–end cloud radar is presented together with an analysis of the impact of the limitations on snowfall rate and total snow accumulation. The second part describes a theoretical study within the applicability of the dual–frequency approach to non–spherical particles is explored. Finally, a new approach is presented extending the dual–frequency approach towards a third frequency in order to potentially distinguish between different snow particle habits. A summary of the results of this thesis is given together with an outlook on future research in Chapter 8.

The analysis of snow scattering signals in ground–based passive MW observations Chapter 6 has been published in:

- Kneifel, S., U. Löhnert, A. Battaglia, and S. Crewell, and D. Siebler, Snow scattering signals in ground–based passive microwave radiometer measurements, *J. Geophys. Res.*, 115, D16214, 2010.

Radiative transfer simulations and statistical analyses of the TOSCA dataset (similar to the analysis presented in Chapter 6 have been contributed to:

- Löhnert, U., S. Kneifel, A. Battaglia, M. Hagen, L. Hirsch, and S. Crewell, 2011: A Multisensor Approach Toward a Better Understanding of Snowfall Microphysics: The TOSCA Project. *Bull. Amer. Meteor. Soc.*, 92, 613–628, 2011.

The capabilities of a low–power K–band radar for snowfall observations (Chapter 7) have been described in:

- Kneifel, S., M. Maahn, G. Peters, and C. Simmer: Observation of snowfall with a low–power FM–CW K–band radar (Micro Rain Radar), *Meteorol. Atmos. Phys.*, 113, 75–87, 2011.

A theoretical study of the applicability of the dual-frequency approach to non-spheroid snow particles together with an extension towards a triple-frequency approach (Chapter 7) has been published in:

- Kneifel, S., M. S. Kulie, and R. Bennartz: A triple-frequency approach to retrieve microphysical snowfall parameters, *J. Geophys. Res.*, 116, D11203, 2011.

## Chapter 2

# The TOSCA Campaign

The observational data used in this study have been collected during the TOSCA campaign (Löhnert et al., 2011). During TOSCA, a comprehensive set of ground-based instrumentation has been deployed at the Umweltforschungsstation Schneefernerhaus (UFS) in the winter season 2008/2009. The UFS is situated just  $\sim 310$  m below the peak of Germany's highest mountain (Zugspitze, 2969 m MSL) located at  $47.42^\circ\text{N}$  and  $10.98^\circ\text{N}$ . UFS is ideally located for snow observation thanks to the frequent occurrence of snowfall and to the presence of low water vapor amounts (typically integrated water vapor content (IWV)  $< 6 \text{ kgm}^{-2}$  during wintertime). The latter is of interest because the dry atmospheric conditions provide a cold background for scattering signals originating from snow particles.

The remote sensing instrumentation combined active radar systems at 24.1 and 35.5 GHz with passive microwave observations in the frequency range from 20 to 150 GHz. The dataset was complemented by optical disdrometers, nearby radiosonde ascents (Radio sounding station Innsbruck and München-Oberschleißheim) and several standard meteorological measurements provided by the German Weather Service (DWD). Table 2.1 gives an overview of the operation time periods for single instruments and also for instrument combinations. Further details about the TOSCA campaign, the instrumentation and available data periods can be found online <http://gop.meteo.uni-koeln.de/tosca/doku.php> or in the overview article by Löhnert et al. (2011). Since this study focuses on passive and active remote sensing, the passive microwave radiometers and the two radar systems will be described in more detail in the following subsections.

### 2.1 Passive microwave radiometers

Two MWR manufactured by Radiometer Physics GmbH (RPG) were deployed: a Humidity and Temperature PROfiler (HATPRO) (Rose et al., 2005) and the Dual Polarization Radiometer (DPR) (Turner et al., 2009) — comprising in total 17 channels in the frequency range from 22 to 150 GHz. The microwave profiler HATPRO (Fig. 2.1) was designed as a network-suitable low-cost radiometer, which can observe LWP, humidity and temperature profiles with high temporal resolution up to 1 s. HATPRO consists of total-power radiometers utilizing 14 direct detection receivers within two bands, 22.235–31.4 GHz and 51.26–58.0 GHz (Fig. 2.2). The measurements are averaged onto a one second temporal resolution. The seven channels of the lower frequency band contain information on the vertical profile of humidity through the pressure broadening of the optically thin 22.235 GHz  $\text{H}_2\text{O}$  line, and therefore also

**Table 2.1:** Instrument availability (quality controlled) during snowfall times of the TOSCA 2008/2009 measurement campaign. About 1218h of snowfall were registered, corresponding to about 25% of the total campaign time [after *Löhnert et al. (2011)*]

Instrument(s)	No. of hours	% of total snowfall time
Total hours of snowfall	1218	100
HATPRO + DPR	361	30
MIRA36	1118	92
2D-Video Disdrometer (2DVD)	348	29
HATPRO + DPR + MIRA36	340	28
HATPRO + DPR + 2DVD	132	11
MIRA36 + 2DVD	336	28
HATPRO + DPR + 2DVD + MIRA36	132	11

about the vertical IWV content. Simultaneously, LWP can be derived from cloud water emission which increases with frequency (Fig. 2.2). Using multi-linear regression (*Löhnert et al., 2001*) IWV and LWP can be derived with accuracies better than  $0.7\text{kgm}^{-2}$  and  $20\text{gm}^{-2}$ , respectively. For the retrieved humidity profile it has been found that the vertical profile contains only two to three independent layers mainly due to the relatively weak water vapor line at 22.235 GHz (*Löhnert et al., 2009*). The seven channels of the higher frequency band contain information on the vertical profile of temperature due to the homogeneous mixing of  $\text{O}_2$  throughout the atmosphere. At the opaque center of the  $\text{O}_2$  absorption complex at 60 GHz, most of the information originates from near the surface, whereas further away from the line, the atmosphere becomes less opaque. Therefore, an increasing amount of information also originates from higher atmospheric layers. The accuracy of the derived temperature profile can significantly be improved to less than 1 K at heights below 1.5 km, if elevations scans are included in the retrieval (*Crewell and Löhnert, 2007*). In order to ensure that measurements at low elevation angles (down to  $5^\circ$ ) are not contaminated by surface emissions, HATPRO has antenna half power beam widths (HPBW) of  $3.5^\circ$  ( $2^\circ$ ) at the lower (higher) frequency channels with a side lobe suppression better than 30 dB.

The DPR (Fig. 2.1) is a three-channel system that performs observations at the window frequencies 90 and 150 GHz (Fig. 2.2), also frequently used by satellite instruments. It uses direct detection at 90 GHz, whereas the 150 GHz channels are heterodyne systems<sup>1</sup>. A wire grid is used to separate the polarizations at the latter frequency, so both the vertical and the horizontal polarization can be measured separately and simultaneously. In order to conserve the plane of polarization during elevation scanning, the DPR is mounted on a rotating horizontal axis. The DPR performs continuous zenith observations at a temporal resolution of 1 s that are interrupted by elevation scans every ten minutes including nine elevation angles between zenith and  $15^\circ$  elevation angle. The HPBW of the DPR antenna is slightly smaller compared to HATPRO with  $1.8^\circ$  and  $1.5^\circ$  at 90 and 150 GHz, respectively. Besides the ability of the DPR to detect snow scattering signals which will be discussed later in this study, it has been shown that the combination of HATPRO and DPR can

<sup>1</sup>In a heterodyne receiver, the received frequency is mixed with a constant frequency from an oscillator to a lower frequency before detection.





**Figure 2.1:** Overview over instruments deployed at (middle) UFS located  $\sim 300$  m below the summit of mountain Zugspitze in the German Alps during the TOSCA campaign in the winter season 2008/2009: (middle left) Microwave profiler HATPRO; (bottom left) – (bottom right) 10-m meteorological mast, 2DVD, Ceilometer, MRR, PARSIVEL disdrometer; (middle right) 35.5 GHz cloud radar MIRA36; (top right) 90/150 GHz dual-polarization microwave radiometer DPR. [from *Löhnert et al.* (2011)]

significantly enhance the accuracy of LWP retrieval especially for LWP values lower than  $100 \text{ gm}^{-2}$  (*Crewell and Löhnert, 2003; Zink, 2010*).

Both radiometers are occasionally calibrated by viewing a liquid–nitrogen target, and the observations from this target and the internal blackbody are used to determine the noise source temperature (in case of HATPRO), system noise temperature, and the gain. Since the noise source and the system noise temperature are assumed to be highly stable, RPG recommends liquid–nitrogen calibration at the beginning of a deployment and every few months after that. However, the gain is updated every few minutes by interrupting the atmospheric observations and viewing an internal blackbody target at ambient temperature. HATPRO also performed regularly scheduled tipping scans (*Han and Westwater, 2000*) for its channels in the range from 22.24 to 31.4 GHz. These were automatically evaluated by the operational radiometer software to update the calibration in case the sky was determined to be homogeneous and cloud free. The resulting absolute  $T_B$  accuracy of HATPRO and DPR is estimated to be 1 K, while the radiometer noise is 0.2 K for HATPRO and 0.7 K for the DPR.

To ensure a high quality of the measured MWR data, it is essential not only to have precise calibrations but also to keep the radome completely free of liquid or frozen water. For that purpose, both radiometers are regularly equipped with heated blower systems. The curved shape of the HATPRO radome, together with the continuous sideward airflow, avoids the accumulation of snow on the radome and is able to evaporate any liquid residuals of former rain or heavy snow showers. Unlike HATPRO, the shape of the DPR radome is a plane circle of 18 cm diameter and thus, precipitation can more easily accumulate. During the campaign, the original axial blower system (Fig. 2.3) of the DPR was found to be insufficient during snowfall. As a consequence a completely new blower concept has been designed and

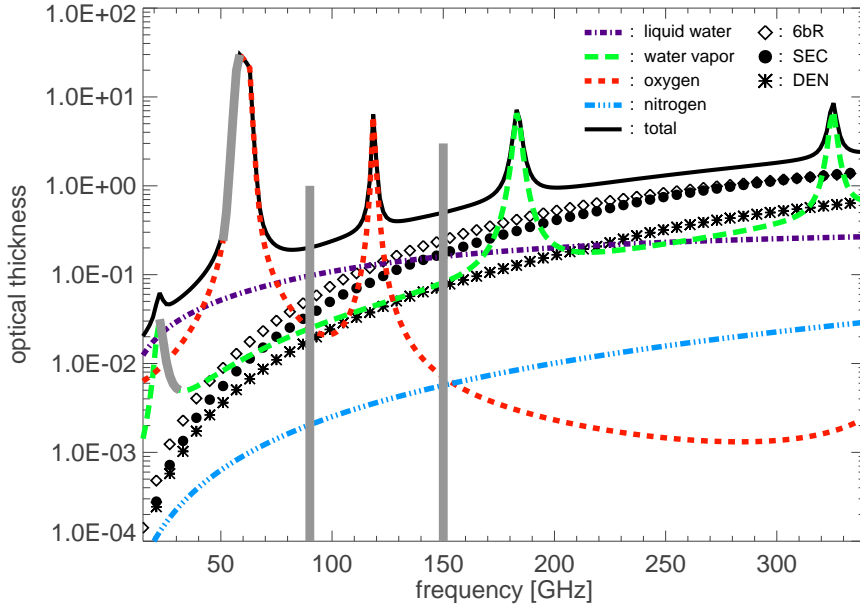


**Figure 2.2:** Microwave spectrum between 10 and 340 GHz: Total optical thickness (bold black) as a function of frequency calculated for a winter snowfall condition (08. Feb. 2009, Section 6.1): The assumed LWP is  $0.1 \text{ kgm}^{-2}$ , whereas the SWP is set to  $0.2 \text{ kgm}^{-2}$ . Contribution due to  $\text{O}_2$  (red short-dashed),  $\text{H}_2\text{O}$  (green long-dashed),  $\text{N}_2$  (blue dashed-triple-dotted) and liquid water (violet dashed-dotted). The different symbols indicate the contribution due to snowfall, assuming different snow particle habits: six-bullet rosettes (open diamond), sector snowflakes (filled circle) and dendrites (asterisk). The thick grey lines show the frequency range covered by the passive microwave radiometers.

installed in collaboration with the University of Munich (Fig. 2.3). The new system consists of an industrial high-pressure blower (AIRPACK) and a heating unit (LHS 60S) manufactured by LEISTER AG, Switzerland, located in a separate box close to the radiometer. The compressed and heated air was lead into a blow-off nozzle providing a concentrated airflow of  $\sim 2 \text{ m}^3/\text{min}$  over the DPR radome. With this new system, measurements were possible even during heavy snow storms. Only in freezing rain or melting snow showers the system reaches its limits. In order to quality control the data and thus to flag disturbed data, cameras were installed at each radiometer for permanent observation of the radome conditions. For this study only data that passed a visual inspection have been used.

## 2.2 Radar systems

### 2.2.1 Cloud radar (MIRA36)

The MIRA36 cloud radar system (manufactured by METEK GmbH, Elmshorn, Germany) is a pulsed, vertically pointing, coherent  $K_a$ -band (35.5 GHz,  $\lambda = 8.4 \text{ mm}$ ) cloud radar (e.g. Melchionna et al., 2008). The radar provides vertical profiles of effective radar reflectivity factor ( $Z_e$ ), the mean vertical Doppler velocity ( $W$ ), the Doppler spectral width ( $\sigma$ ), and the linear depolarization ratio (LDR). The system at the UFS was operated with a temporal resolution of 10 s and a range resolution of 30 m (lowest usable range gate at 300 m) which leads



**Figure 2.3:** Upper line: DPR with old blower system and ice/snow on the radome; Lower line: (left) Tilted DPR with new blower system, (middle) open blower box, (right) new blower system during snowfall.

to a maximum measurement height of 15 km above ground. A sensitivity of  $-44$  dBz at 5 km range allows detecting even high-level ice clouds. The complete MIRA36 system was installed in a thermally stabilized container to ensure optimal performance during harsh weather conditions (Fig. 2.1). Additionally, the radar dish was equipped with a 1.5 kW heating system to avoid snow accumulation on the antenna.

Several empirical relations exist to derive physical quantities like SWC (a detailed discussion about derivation of physical quantities from radar measurements will follow in Chapter 7) from the vertical  $Z_e$ -profiles. In this study, SWC has been derived with a temperature dependent  $Z_e$ -SWC relation given in *Hogan et al. (2006)*:

$$SWC = \exp(2.42 \times 10^{-3} Z_e T + 0.0699 Z_e - 0.0186 T - 1.63). \quad (2.1)$$

The variables in Eq. 2.1 have units of dBz for  $Z_e$ ,  $^{\circ}\text{C}$  for the temperature  $T$  and  $\text{gm}^{-3}$  for SWC. The temperature dependence takes into account that with increasing distance from the cloud top in general diffusional growth and aggregation lead to larger particles and broader SSD (see also Section 3.1). However, it should be noted that  $Z_e$ -SWC relation are in general extremely dependent on the assumed particle habit and SSD (e.g. *Kulie and Bennartz, 2009*).

### 2.2.2 Micro rain radar (MRR)

The Micro Rain Radar MRR-2 (METEK GmbH) (Fig. 2.1) is a vertically pointing, low-cost, Frequency Modulated Continuous Wave (FMCW) coherent Doppler radar operating at K-band (24.1 GHz,  $\lambda = 12.4$  mm) (*Peters et al., 2002*). The system was originally designed to derive microphysical properties of rainfall like vertical profiles of rain rate, drop size distribution and mean fall velocity. Thus, the requirements for the MRR were originally much

**Table 2.2:** Main technical specifications of the 24.1 GHz MRR and the 35.5 GHz MIRA36 [after *Kneifel et al. (2011b)*]

Parameter	MRR	MIRA36
Frequency (GHz)	24.1	35.5
Radar type	FM–CW	Pulsed
Transmit power	50 mW	30 kW (peak power)
Receiver	Single Polarization	Dual Polarization
Power consumption (radar)	25 W	1 kW
Total power consumption	525 W	3.4 kW
Max. range (km)	6	30
Range resolution (m)	10–200	15–60
No. of range gates	30	500
Antenna diameter (m)	0.5	1.0
Beam width (2–way, 6 dB)	1.5°	0.6°

lower compared to the MIRA36 system. A direct comparison of the mean technical specifications of MIRA36 with the MRR are given in Tab. 2.2: Unlike MIRA36, the MRR is not able to distinguish between different states of polarization in the backscattered signal which is needed e.g. to determine LDR. The CW–operation allows the use of a low–power transmitter (50 mW), since the sensitivity of a coherent radar depends on the average and not on the peak transmit power. The instrument consists of a parabolic offset dish antenna with a 0.5 m effective aperture diameter and a resulting beam width (2–way, 6 dB) of 1.5°. The height resolution can be varied from 10 to 200 m which determines, together with the fixed 30 range gates, the system’s maximum height range of 300–6000 m. The sensitivity of the instrument has been found to be 1 dBz at 2500 m range (see Chapter 7) which is sufficient for rain observations but much lower than of the MIRA36. The whole system, containing receiver and data analysis unit, has a comparably low power consumption of 25 W. Optionally, it is possible to heat the dish which increases the total power consumption up to ~525 W. The heater is particular useful in case of wet snowfall and low wind speed conditions that favor the accumulation of snow on the dish. During TOSCA, the MRR was continuously heated to ensure optimal performance.

### 2.2.3 2D–Video disdrometer (2DVD)

The 2D–Video Disdrometer (2DVD) (*Kruger and Krajewski, 2002*) developed by Joanneum Research supplies important information about shape and intensity of snowfall close to the ground. In contrast to standard optical disdrometers, the 2DVD illuminates the hydrometeors with two cameras from two orthogonal sides allowing the determination of size, shape and fall velocity of the particle. Large ambient wind speeds have been identified by *Nešpor et al. (2000)* and *Brandes et al. (2007)* to be responsible for potential undersampling, particularly of smaller particles. To exclude 2DVD data possibly disturbed by wind effects, only 2DVD measurements in low wind speed conditions ( $v < 5\text{ms}^{-1}$ ) were considered. For the derivation of snow related parameters an exponential SSD is assumed

$$N(D) = N_0 e^{-\Lambda D}, \quad (2.2)$$

with  $N(D)$  [ $\text{m}^{-4}$ ] the particle number density in a given particle size range,  $N_0$  [ $\text{m}^{-4}$ ] the intercept parameter and  $\Lambda$  [ $\text{m}^{-1}$ ] the slope coefficient. From the two 2DVD views of the particle first the image with the largest particle extension is selected and then the maximum particle dimension  $D$  is defined as the largest axis of the circumscribed ellipse. To estimate the two parameters  $N_0$  and  $\Lambda$  for the SSD, it is important (1) to have a sufficiently large sample size (*Smith and Kliche, 2005*) and (2) to ensure that the sample originates from a single SSD, i.e. the same microphysical process, requiring a sufficiently short time period. As a compromise between both demands,  $N_0$  and  $\Lambda$  are calculated with the moment method described in (e.g. *Field et al., 2005*) for every 1000 particles within a maximum allowed time period of five minutes. According to the analysis made by *Hanesch (1999)*, snow particles with unrealistically high fall velocities of  $> 4\text{ms}^{-1}$  and height to length ratios lower (greater) than 0.1 (10) are probably artificially generated by the 2DVD software due to wrong particle image matching and are thus discarded.

The moment of order  $n$  is defined as

$$M_n = \int_0^\infty D^n N(D) dD. \quad (2.3)$$

Combining Eq. 2.2 and Eq. 2.3 gives

$$M_n = \frac{N_0}{\Lambda^{n+1}} \Gamma(n+1). \quad (2.4)$$

The two parameters of the SSD  $\Lambda$  and  $N_0$  can be obtained by relations of different moments e.g.:

$$\Lambda = 3 \frac{M_2}{M_3} \quad N_0 = 13.5 \frac{M_2^4}{M_3^3} \quad (2.5)$$

From the approximated particle volume provided by the 2DVD software (e.g. *Brandes et al., 2007*) and a density–maximum size relation (*Muramoto et al., 1995*) it is further possible to calculate a liquid equivalent snowfall rate. Since the particle volume approximation is based on only two projections, it cannot fully account for the "fluffiness" of the snow aggregates and therefore, the derived snowfall rate should be interpreted with care.



## Chapter 3

# Snowfall Microphysics

Everyone might once have observed the fascinating, seemingly endless diversity of snow habits when being outside during snowfall. For the single particles one might be able to develop some coarse classification into plates, needles or dendrites. But once the smaller particles start to aggregate, the variety of possible combinations seems to be infinite. The question how snow particles can be classified and which particle habits and mixtures occur under which meteorological conditions is still an important, but unsolved scientific question. The habit information is implicitly connected to essential important relations implemented in numerical weather prediction and climate models: How is the particle size and its mass related and how can the terminal fall velocity be related to the particle size? While the first relation connects the SSD with the SWC of a certain volume, the second relation determines how fast the snow mass sediments into lower vertical layers.

A comprehensive description of snow microphysics (e.g. *Pruppacher and Klett, 1997*) would include the entire snow forming process chain of ice nucleation, crystal diffusional growths from water vapor, aggregation of single crystals as well as riming of ice particles by liquid cloud droplets. Since the focus of this work lies on the radiative interaction of microwave radiation and snow particles, the following description concentrates on microphysical properties that have the largest direct influence on the radiative transfer: The mathematical description of SSD, particle habits and their dependence on temperature and humidity, mass-size relation and finally, a short discussion about particle orientation.

### 3.1 Snow size distribution

In order to derive a SSD from observations one has to define what is exactly meant by “snow size”. Looking into scientific literature about SSD observations, a large variety of definitions can be found: maximum geometric size of the circumscribed sphere or ellipse, radius of the liquid equivalent sphere, radius of the equivalent volume sphere, particle mass, etc. (*Petty and Huang, 2011*). One of the reasons for the varying definitions are the varying measuring principles of the instruments that were used to observe snow particles. From a physical standpoint, the best defined quantity would be particle mass. However, since most ground-based and airborne in-situ instruments are based on 2D projections of the snow particle (e.g. *Braham, 1990; Field et al., 2005; Brandes et al., 2007; Woods et al., 2008*), it seems reasonable to use the truly “observed” size definition. So even if mass would be the preferred SSD variable, in this study all SSDs are defined as function of the maximum

geometric diameter  $D$  of the particles 2D projection.

The most commonly used model for atmospheric particle size distributions is the four-parameter modified gamma distribution<sup>1</sup>:

$$N(D) = N_0 D^\mu \exp(-\Lambda D^\gamma). \quad (3.1)$$

The particle number density in a given particle size range  $N(D)$  [ $\text{m}^{-4}$ ] is parameterized with four parameters: the intercept parameter  $N_0$  [ $\text{m}^{-4}$ ], the slope parameter  $\Lambda$  [ $\text{m}^{-1}$ ] and the dimensionless parameters  $\mu$  and  $\gamma$ . Setting  $\mu = 0$  and  $\gamma = 1$  the simpler two-parameter exponential size distribution (Eq. 2.2, Section 2.2.3) is obtained.

In several studies (*Gunn and Marshall*, 1958; *Houze et al.*, 1979; *Brandes et al.*, 2007; *Siebler*, 2010), the exponential distribution has been found to be a good approximation for snowfall. Even if snowfall events with slightly over- or under-exponential SSD can be found (*Brandes et al.*, 2007; *Siebler*, 2010), the majority of the observed SSD follow the exponential distribution. In the following parts of this study, the SSD is always assumed to be exponential. The observed range for the two exponential SSD parameters varies depending on whether they were measured by airborne systems (e.g. *Woods et al.*, 2008) or sampled at the ground (*Brandes et al.*, 2007; *Löhnert et al.*, 2011). The airborne measurements reveal in general higher values for both  $N_0$  and  $\Lambda$ . This can be explained by the fact that in higher cloud regions particles are generally less aggregated as in the cloud regions close to the ground. On the one hand, a well known issue with aircraft measurements is that particle shattering at the optical probes (*Korolev et al.*, 2011) can affect the measured SSD in the way that large particles are underestimated and smaller particles are overestimated. SSDs measured at the ground, on the other hand, can be affected by sublimation in the layers below the cloud base and by wind induced turbulence at the disdrometer (*Nešpor et al.*, 2000).

It has also been found that SSD parameters are temperature dependent most likely due to the temperature dependent aggregation processes (Section 3.2). One of these temperature dependent relations which is based on a large number of aircraft in-situ observations is given by *Field et al.* (2005):

$$N_0 = 7.63 \times 10^6 \exp(-0.107 T_C). \quad (3.2)$$

Assuming cloud temperatures  $T_c$  in  $^\circ\text{C}$  to be ranging from 0 to  $-20^\circ\text{C}$ , one yields, according to Eq. 3.2, a  $N_0$  which varies from  $7.63 \times 10^6$  to  $1.1 \times 10^8 \text{ m}^{-4}$  (Fig. 3.1). While there is no doubt that in general  $N_0$  and  $\Lambda$  increases toward lower temperatures (*Houze et al.*, 1979; *Ryan*, 2000; *Brandes et al.*, 2007), the large scattering of measured SSD parameters reflects both the natural variability of snow sizes and the aforementioned uncertainties of the derived SSD due to observational errors. Also, the ground-based in-situ data collected during TOSCA revealed a slight temperature dependence of both  $N_0$  and  $\Lambda$  in the range of  $10^5$ – $10^8 \text{ m}^{-4}$  for  $N_0$  and 300 to  $2500 \text{ m}^{-1}$  for  $\Lambda$  (*Siebler*, 2010; *Löhnert et al.*, 2011) (Fig. 3.1). For instance, at 2m-temperatures lower than  $-15^\circ\text{C}$ , the derived  $N_0$  values are found in the range of  $10^7$  and  $10^8 \text{ m}^{-4}$ . For the temperature region between 0 and  $-15^\circ\text{C}$ , the 2DVD data do not show a clear temperature dependence, while there is a tendency for lower  $\Lambda$ -values

---

<sup>1</sup>A comprehensive review of particle size parameterizations and their relations to each other can be found in *Petty and Huang* (2011).



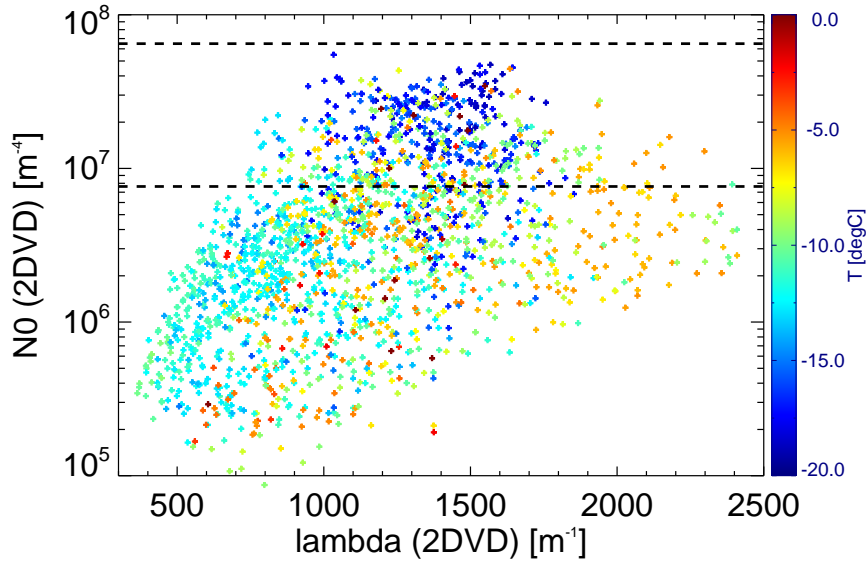


**Figure 3.1:** Parameters  $N_0$  and  $\Lambda$  for an exponential SSD derived from 2DVD measurements (colored plus signs) during TOSCA using the moment–method described in Section 2.2.3. The color of the signs represents the 2m–temperature in  $^{\circ}\text{C}$ . The horizontal dashed lines indicate the  $\Lambda$  range if the 2m–temperatures measured at the UFS during TOSCA are inserted into the temperature dependent *Field et al. (2005)* parametrization (Eq. 3.2).

(broader SSDs) between  $-10$  and  $-15$   $^{\circ}\text{C}$  potentially related to the “secondary growth” region (Section 3.2). The  $N_0$  values estimated using Eq. 3.2 yield by 1–2 orders of magnitude higher  $N_0$  values. These  $N_0$  –differences can have several reasons: The 2DVD potentially undersamples the actual SSD, since mismatched particles are discarded by the 2DVD algorithm. Another explanation for the deviations in  $N_0$  might come from the special orographic conditions at the UFS. *Kusunoki et al. (2005)* reported increasing snow aggregation due to stronger up–winds and turbulence in a mountainous orography. These larger particles would consequently result in lower values for  $N_0$  and  $\Lambda$ , i.e. a broader SSD. *Field et al. (2005)* defined  $D$  as the particle size parallel to the flight direction. Due to the measurement system, the usable size range was limited to 0.1–4.4 mm. In contrast,  $D$  has been derive in this study from the 2DVD’s two particle projections and particle sizes from 0.5–40 mm have been considered. In addition to the different definition and range of  $D$  the aforementioned shattering effects on aircraft probes can potentially affect the empirical relations in Eq. 3.2. The temperature dependent SSD parameterizations should thus be interpreted as averaged relations that include the possibility that real SSD can significantly deviate from the estimated  $N_0$ .

## 3.2 Snow particle habit

Besides the wide span of snow sizes from a tenth of a millimeter up to a few centimeters, the complexity of possible snow particle habits is the reason why the description of snowfall microphysics is more challenging than e.g. the description of rainfall. Sophisticated classification schemes (e.g. *Magono and Lee, 1966*) allow a detailed characterization of the manifold snow particle habits. The aim of this section is not a thorough discussion of the complexity

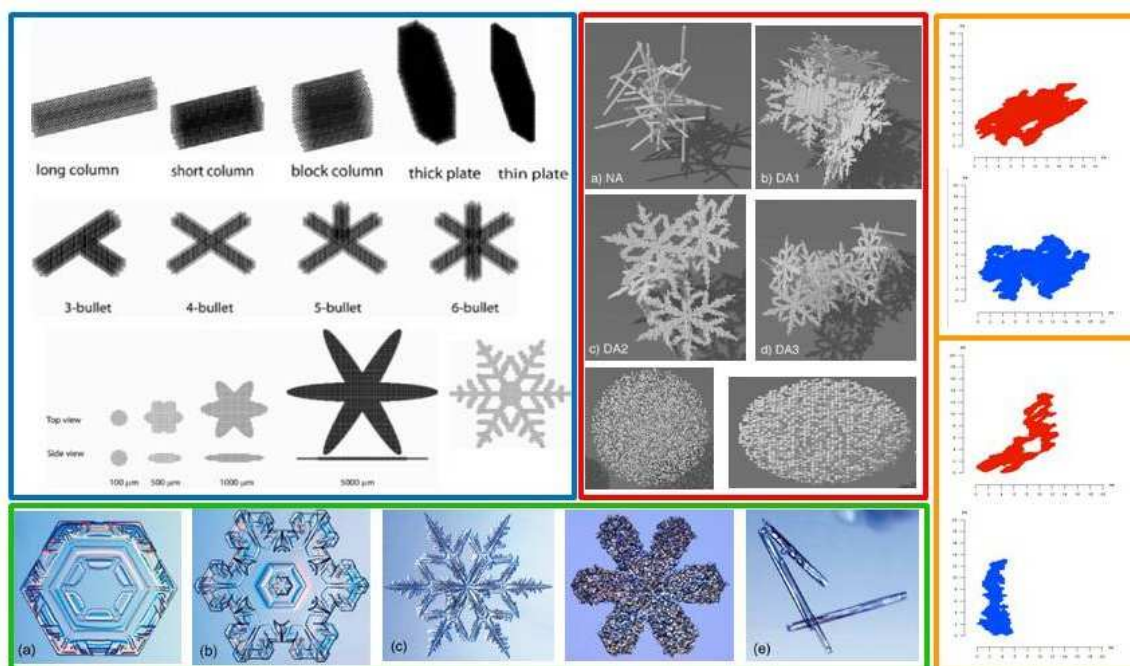


**Figure 3.2:** Impressions of snow particle habits used for scattering computations and measured during snowfall: (blue box) Snow particle habits used in the scattering database by *Liu* (2008a), (first line) hexagonal columns and plates, (second line) 3 to 6–bullet rosettes, (third line) sector snowflakes and (third line, right) dendrite [extracted from *Liu* (2008a)]; (red box) Snow particle habits from calculations made by *Petty and Huang* (2010), (upper left) needle aggregate NA, (upper right) dendrite aggregate DA1, (middle left) dendrite aggregate DA2, (middle left) dendrite aggregate DA3, (lower left) “soft” sphere, (lower right) “soft” ellipsoid [extracted from *Petty and Huang* (2010)]; (green box, from left to right) ice plate, sector snowflake, dendrite, rimed dendrite and needles [from <http://www.snowcrystals.com> and *Libbrecht* (2005)]; (orange boxes) 2D sideview of two snowflakes (camera A in red, camera B in blue) by the 2DVD during TOSCA (total scale in the images is 20 mm).

of snow particles habits but rather to focus on basic pristine habits and their relation to atmospheric variables as well as on the principal process of aggregation. Figure 3.2 gives an impression about observed snow habits and the theoretical snow particle habits that represent the most recent snow particle models for radiative transfer simulations that are also used in Chapter 5.

Single, pristine particles are generally found at lower sizes ( $< 5\text{mm}$ ) of the snow particle size spectrum (*Auer and Veal*, 1970, e.g.). The particle habit was found by observations (e.g. *Magono and Tazawa*, 1966; *Heymsfield et al.*, 2002) and cloud chamber experiments (*Takahashi et al.*, 1991; *Libbrecht*, 2005) to be a distinct function of temperature and super-saturation (Fig. 3.3): Between  $0^\circ\text{C}$  and  $-4^\circ\text{C}$  plate-like crystals grow and develop dendritic structures at high super-saturations. Between  $-4^\circ\text{C}$  and  $-8^\circ\text{C}$  particle growth changes into columns and thin needles. At lower temperatures between  $-8^\circ\text{C}$  and  $-22^\circ\text{C}$  plate-like crystals dominate again, with enhanced branching and dendritic structures towards higher super-saturations. Finally, below  $-22^\circ\text{C}$  thick plates grow at low and columns at high super-

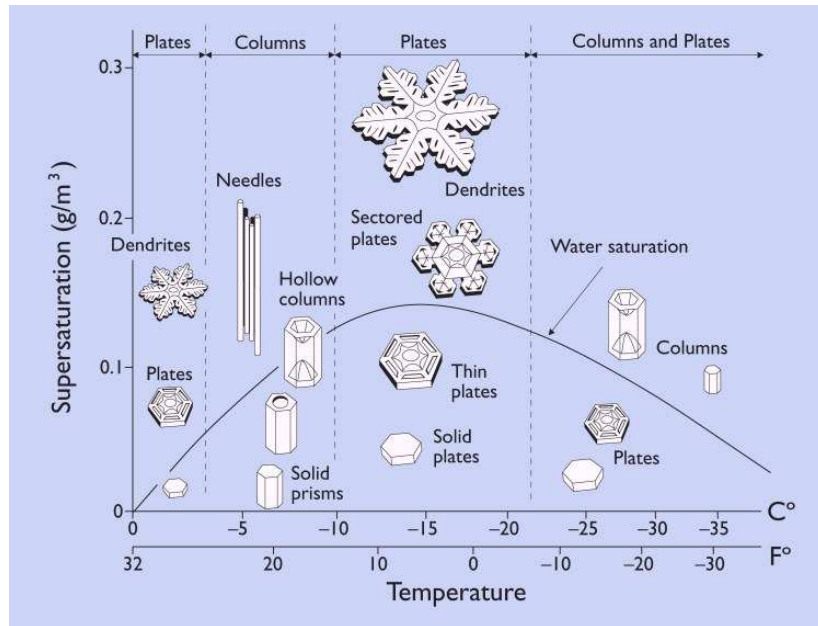


**Figure 3.3:** Snow crystal morphology diagram: Typical snow crystals growing in the atmosphere at different temperatures and water vapor super-saturations relative to ice. The water saturation line shows the super-saturation of super-cooled water. [Extracted from *Libbrecht* (2005)]

saturation. It is important to consider that the final habit depends on the “growth history” of the particle while falling through the cloud. For instance, a particle grows as a hexagonal plate at  $-15^{\circ}\text{C}$  and relatively dry conditions. When it falls into a region with higher super-saturation, it develops branches at the edges of the plate and becomes a dendrite. Falling through a layer of super-cooled droplets leads to freezing of the liquid drops on the ice particle and the particle becomes a rimed dendrite or even graupel. While the dependence of a single particle habit growing at a given temperature and super-saturation can be explained by vapor diffusional growth (e.g. *Libbrecht*, 2005), the question under which conditions single particles are forming aggregates is less clear. In general, two temperature regions have been identified to favour aggregation:

### Primary growth region above $-5^{\circ}\text{C}$

Disdrometer observations like the comprehensive study conducted with a 2DVD by *Brandes* et al. (2007) show a sharp increase of particle size at temperatures above  $-5^{\circ}\text{C}$ . They note that this “primary aggregation growth region” can most probably be explained by a quasi-liquid film on the surfaces of ice surfaces (*Hosler* et al., 1957; *Rosenberg*, 2005), leading to an increased “stickiness”, i.e. higher collection efficiency. Unfortunately, it was not possible to observe this strong increase during TOSCA because only a small part of the observations took place above  $-5^{\circ}\text{C}$ .

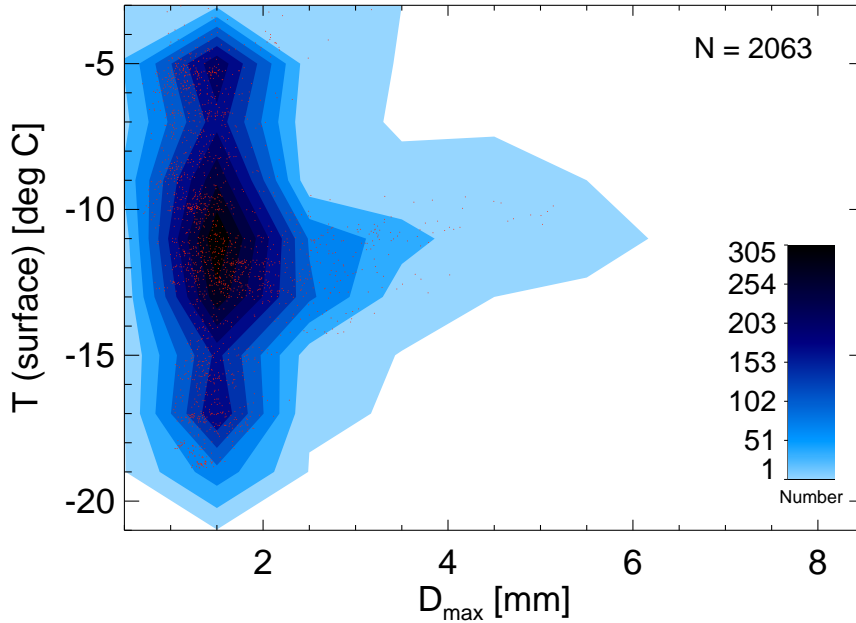


**Figure 3.4:** 2m-temperature as a function of snow particle maximum geometric diameter  $D_{max}$  measured with the 2DVD during TOSCA. The actual measurements corresponding to 10-min averages are shown as orange points. [from *Löhnert et al. (2011)*]

### Secondary “dendritic” growth region

While the first growth region depends on the “wetness” of the snow particles, the second growth region has a more structural reason. In the temperature range between  $-10^{\circ}\text{C}$  and  $-15^{\circ}\text{C}$ , the super-saturation over ice with respect to liquid water reaches its maximum value so that the Wegener-Bergeron-Findeisen process (e.g. *Pruppacher and Klett, 1997, 119 pp.*), i.e. the transformation of liquid drops to ice crystals via the gas phase, may be especially effective (Fig. 3.3). Additionally, snow crystals are found to evolve dendritic structures in this temperature range, especially in combination with high super-saturations (*Libbrecht, 2005*). The branched structure seems to lead to a very effective stickiness when single particles collide. This so-called “secondary growth region” of preferred aggregation growth has been observed by *Hobbs et al. (1974)* and *Hosler and Hallgren (1960)*. The 2DVD data of the TOSCA campaign confirm the existence of this effect: The histogram of maximum particle size dimension  $D_{max}$  and surface temperature (Fig. 3.4) reveals an almost temperature independent  $D_{max}$ , except for the temperature range between  $-10$  and  $-15^{\circ}\text{C}$  where the more frequent occurrence of much larger snow crystals can be observed. At this point it should be noted that the sticking efficiency of ice particles is in state-of-the-art cloud models often parameterized as a simple function of temperature (e.g. *Seifert and Beheng, 2006*). This might lead to significant model errors in the representation of snow particle sizes and habits.

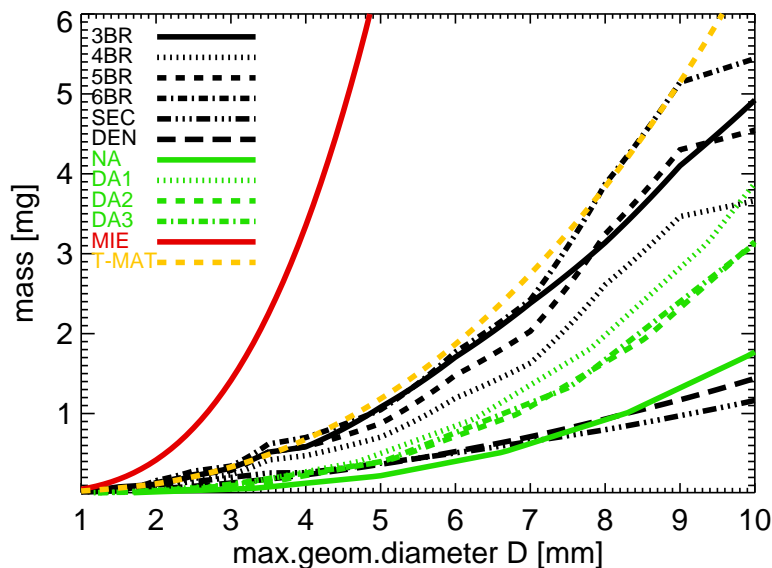


**Figure 3.5:** Particle mass [mg] as a function of maximum geometric diameter  $D$  [mm]. The different particle models are color coded (see also Fig. 3.2): Liu database (*Liu, 2008a*) (black) 3 to 6–bullet rosettes (3BR–6BR), sector snowflakes (SEC), dendrites (DEN); Aggregates (*Petty and Huang, 2010*) (green) needle aggregate (NA), different aggregates composed of dendrites (DA1–3); Soft sphere (red) with assumed snow density of  $100 \text{ kg m}^{-3}$ ; Soft ellipsoid (yellow) with aspect ratio of 0.6. [from *Kneifel et al. (2011a)*]

### 3.3 Mass – size relation

The relation between the particle size and mass — generally called mass–size relation (m–D relation) — is an essential property of snow particles and one of the main sources of uncertainty in current snowfall retrievals. Commonly, the particle mass  $m(D)$  is approximated with a power law in the form

$$m(D) = a D^b. \quad (3.3)$$

The dimensionless coefficients  $a$  and  $b$  depend on the specific particle properties, have to be derived from observations or are given by a theoretical particle model. The m–D parameters  $a$  and  $b$  from the theoretical snow particle models that are later used for radiative transfer simulations (Section 5.4) are summarized in Table 3.1. A comparison of the different relations is shown in Figure 3.5. The variability found in in–situ observations (e.g. *Locatelli and Hobbs, 1974*) is well covered by the theoretical particle models, since observational mass–size relations are the basis of most of the theoretical particle models.

The naturally large variability of m–D relations is caused by the fact that particle habit and m–D relation are closely connected: An example shall be given for a plate–like crystal such as a dendrite and a graupel particle (Fig. 3.2): For the approximately spherical graupel grain the particle volume and its mass increase roughly proportional to  $D_{max}^3$  and thus,  $b$  is close to three. The volume of the dendrite, however, increases much slower with size resulting in  $b$ –values between two and three. If the dendrite falls through a layer of super–cooled water

**Table 3.1:** Parameters  $a$  and  $b$  for different mass–size relations applied to Eq. 3.3 in SI units [from *Kneifel et al. (2011a)*]. The references for the different particle habits are: *Liu (2008a)* (LIU08), *Petty and Huang (2010)* (PH10), *Matrosov (2007)* (MA07)

Particle model	$a$	$b$	Reference
3b–rosette (3BR)	$1.830 \times 10^{-1}$	2.274	LIU08
4b–rosette (4BR)	$1.287 \times 10^{-1}$	2.264	LIU08
5b–rosette (4BR)	$1.680 \times 10^{-1}$	2.274	LIU08
6b–rosette (4BR)	$2.124 \times 10^{-1}$	2.285	LIU08
Sector snowflake (SEC)	$1.191 \times 10^{-3}$	1.511	LIU08
Dendrite (DEN)	$5.666 \times 10^{-3}$	1.820	LIU08
Needle aggregate (NA)	$8.863 \times 10^{-1}$	2.830	PH10
Dendrite aggregate (DA1)	2.121	2.853	PH10
Dendrite aggregate (DA2)	1.498	2.821	PH10
Dendrite aggregate (DA3)	1.761	2.849	PH10
Ellipsoid (T–MAT) ( $0.1\text{mm} < D \leq 2\text{mm}$ )	$3.0 \times 10^{-2}$	2	MA07
Ellipsoid (T–MAT) ( $2\text{mm} < D \leq 20\text{mm}$ )	$6.7 \times 10^{-1}$	2.5	MA07
Soft sphere (MIE)	$\rho_{snow}\pi/6$	3.000	/

droplets, the dendrite becomes more and more rimed (until it becomes a graupel grain) and its habit changes as well as the corresponding m–D relation.

Besides the natural variability of snow particle habits, the lack of combined measurement of particle size and mass can introduce errors in the derived m–D coefficients. In addition to a relatively small number of manually measured m–D relations (e.g. *Locatelli and Hobbs, 1974*; *Mitchell et al., 1990*), snow particle size and habit are mostly obtained by optical disdrometers or airborne particle probes that use 2D projections of the particle. Usually, the corresponding particle mass is not directly measured but rather estimated by the approximated particle volume which is reconstructed from the 2D projections (e.g. *Brandes et al., 2007*). Another method is to measure simultaneously the particle size and habit with optical instruments and integrated mass-related quantities. Such integrated quantities can be obtained by measuring the total snow accumulation at the ground or the SWC with a second airborne instrument (e.g. hot wire probes).

The relevance of the m–D relation can be further understood considering that it connects an assumed SSD with the total mass of the distribution (SWC):

$$SWC = \int_0^{\infty} N(D) m(D) dD. \quad (3.4)$$

In order to derive mass related quantities like SWC, it is thus essential to carefully constrain both  $N(D)$  and  $m(D)$ .

### 3.4 Orientation

The question if snow particles fall with a preferential orientation has many implications for snow radiative transfer as well as for cloud microphysical parameterizations: Oriented particles with a high/low aspect ratio<sup>2</sup> can dramatically change e.g. backscattering cross section (*Sun et al., 2011*) or the scattering signature observed by passive microwave instruments (*Xie et al., 2011*). Particle orientation can also be a critical factor for size dependent relations like terminal fall velocity — size assumptions that are found to have an enormous influence on the snow mass distribution in numerical weather prediction models (*Reitter et al., 2011*). The effect of particle orientation on terminal fall velocity can easily be imagined, if, for example, a plate-like particle is assumed to fall with its longest axis horizontally or vertically aligned.

The orientation of single ice particles strongly depends on particle habit and its size (e.g. *Pruppacher and Klett, 1997*). In-situ observations (*Zikmunda and Vali, 1972*) as well as polarized radar measurements (*Matrosov et al., 2005b*) confirmed that symmetrical planar particles (e.g. plates, dendrites, stellar plates) tend to fall with their major axis horizontally aligned. Reaching a certain size (strongly depending on particle habit), secondary motions and “fluttering” are caused by shedding of eddies from the rear of the falling crystal (*Kajikawa, 1992*). For complex aggregates reaching cm-sizes it is currently unclear if they have a distinct orientation. However, in-situ observations made by *Hanesch (1999)* and passive remote sensing observations of polarization differences originating from scattering by snow particles at 150 GHz (*Xie et al., 2011*) indicate that there is a significant fraction of aggregates falling with their major axis orientated parallel to the ground.

---

<sup>2</sup>Defined here as the ratio of their minimal to maximum dimension





## Chapter 4

# Radiative Transfer at Microwave Frequencies

Remote sensing applications in atmospheric sciences make use of the specific interaction of electromagnetic waves with atmospheric constituents like gases, aerosols or hydrometeors. This chapter presents a short overview about the interacting processes and how they can finally be integrated into a radiative transfer equation (RTE) that can be solved numerically. The considerations will focus on the microwave region, usually defined as the frequency range between 3 and 300 GHz, that corresponds to wavelengths of 1 m down to 1 mm. The theory presented in this chapter is partly drawn from (*Petty, 2006*) and (*Bohren and Huffman, 1983*).

### 4.1 Basic concepts

The amount of energy that is transported by an electromagnetic wave with wavelength  $\lambda$  through a unit area  $A$  and per unit time is expressed by the flux density, or often called electromagnetic flux,  $F_\lambda$  in units of  $\text{W m}^{-2}$ . To fully characterize the radiation field, the directional information is needed. This leads to the definition of radiant intensity, radiance or short intensity. The monochromatic intensity  $I_\lambda$  — i.e. valid only for an infinitesimal small wavelength range — is defined as the flux per effective area  $\cos(\theta) dA$  and unit solid angle  $d\omega$ :

$$I_\lambda = \frac{dF_\lambda}{d\omega \cos \theta dA}. \quad (4.1)$$

The solid angle  $d\omega$  can be expressed in polar coordinate as follows:

$$d\omega = \sin(\theta) d\theta d\phi. \quad (4.2)$$

Figure 4.1 illustrates the relation of polar coordinates given as  $\phi$  and  $\theta$  angles and the solid angle (in units of steradian, sr) that can be interpreted as an infinitesimal “angular area” of the hemisphere. Given the above definitions, it is clear that  $I$  has units of  $\text{W m}^{-2} \text{sr}^{-1} \text{m}^{-1}$ .

Another important property of radiation besides its “strength” and direction of propagation is its state of polarization. Polarization in general describes the electric field vector of

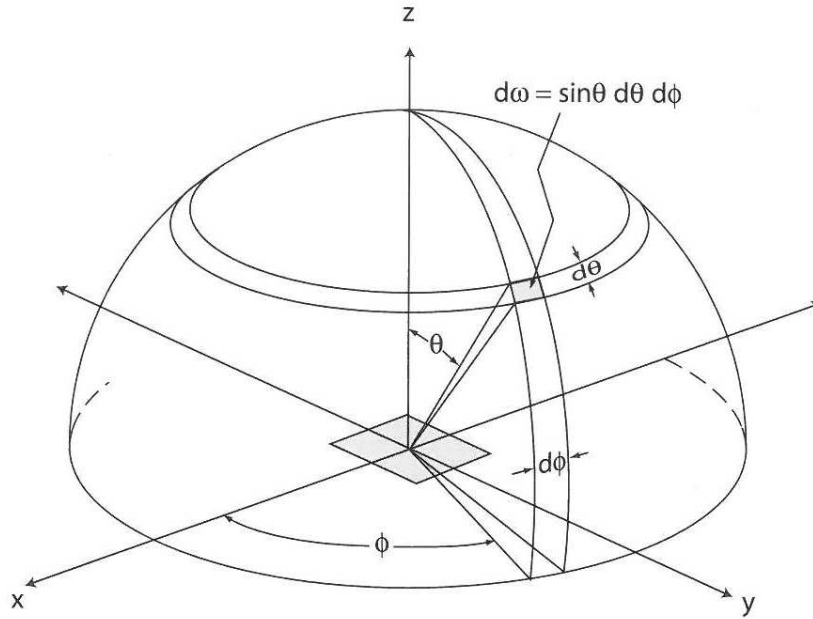


**Figure 4.1:** The relationship between solid angle and polar coordinates. [extracted from *Petty* (2006, p. 39)]

the electromagnetic wave that lies in a plane, the normal to which is parallel to the direction of propagation. A detailed description of polarization can be found in (e.g. *Bohren and Huffman*, 1983, 44 pp). If the complete information of the state of polarization is needed, it is convenient to define radiant intensity as a four element vector of the form:

$$\vec{I} = \begin{pmatrix} I \\ Q \\ U \\ V \end{pmatrix}. \quad (4.3)$$

The elements of  $\vec{I}$  are called the Stokes parameters and  $\vec{I}$  is often called the Stokes vector. The first element  $I$  is the scalar intensity as defined before. The other elements contain information about the degree of polarization, preferred orientation and the type of polarization i.e. linear, circular or a mixture of both. For example,  $I = [1, 1, 0, 0]$  describes completely horizontally polarized radiation while  $I = [1, 0, 0, -1]$  represents a left circularly polarized beam.

The degree of polarization is defined as the ratio  $\sqrt{Q^2 + U^2 + V^2}/I$  ranging from zero (completely unpolarized) to one (fully polarized). This leads to the general relation

$$I^2 \geq Q^2 + U^2 + V^2, \quad (4.4)$$

which illustrates that the four Stokes elements are not independent. With this formal description of electromagnetic radiation, the different interactions of radiation with matter will be discussed in the following parts of the chapter. If not noted explicitly, polarization is

neglected in the following description, since only unpolarized radiation is considered in this study and thus the intensity vector  $\vec{I}$  reduces to the scalar  $I$ .

## 4.2 Absorption and thermal emission

The ability of matter to absorb electromagnetic energy is dependent on the type of the matter and frequency of the radiation. Given a homogenous medium, the “strength” of absorption can be expressed with the absorption coefficient  $\beta_a$ :

$$\beta_a = \frac{4\pi n_i}{\lambda}. \quad (4.5)$$

$\lambda$  is the wavelength of the radiation in m, and  $n_i$  is the complex part of the dimensionless refractive index  $n = n_r + in_i$  that can be interpreted as a specific property of the interacting medium. In general,  $n$  is dependent on temperature and frequency as well as on medium-specific variables like conductivity.  $\beta_a$  is the corresponding volume absorption coefficient in units of  $\text{m}^{-1}$ . With  $\beta_a$  it is possible to express the change of intensity  $dI_a$  of the original intensity  $I_0$  due to propagation through the medium along the infinitesimal path  $ds$ :

$$dI_a = -\beta_a(s)I_0 ds. \quad (4.6)$$

The volume absorption coefficient  $\beta_a$  can also be expressed as the product of the density of a certain media  $\rho$  and the corresponding mass absorption coefficient  $\kappa_a$  [ $\text{m}^2\text{kg}^{-1}$ ]:

$$\beta_a = \kappa_a \rho. \quad (4.7)$$

If the absorber can be represented by a size distribution  $N(D)$  [ $\text{m}^{-4}$ ] of particles (e.g. aerosols, cloud droplets, ice crystals) with a specific size  $D$ ,  $\beta_a$  can be obtained by the integral

$$\beta_a = \int_0^\infty \sigma_a(D) N(D) dD, \quad (4.8)$$

where  $\sigma_a(D)$  is the size specific absorption cross section in  $\text{m}^2$ .

Given a body or medium that is a perfect absorber or often called “black body”, the emitted radiation from this body is a unique function of frequency and the black body temperature. This relation is expressed by the so called *Planck function*:

$$B_\lambda(T) = \frac{2hc^2}{\lambda^5(e^{hc/k_B\lambda T} - 1)}. \quad (4.9)$$

Here  $c = 2.998 \times 10^8 \text{ ms}^{-1}$  is the speed of light in vacuum,  $h = 6.626 \times 10^{-34} \text{ Js}^{-1}$  is Planck’s constant,  $k_b = 1.381 \times 10^{23} \text{ JK}^{-1}$  is Boltzmann’s constant and  $B_\lambda(T)$  is the emitted monochromatic intensity.

The Planck function  $B_\lambda(T)$  relates the emitted monochromatic intensity directly to the body’s temperature (Fig. 4.2). The intensity at different wavelengths in general increases at

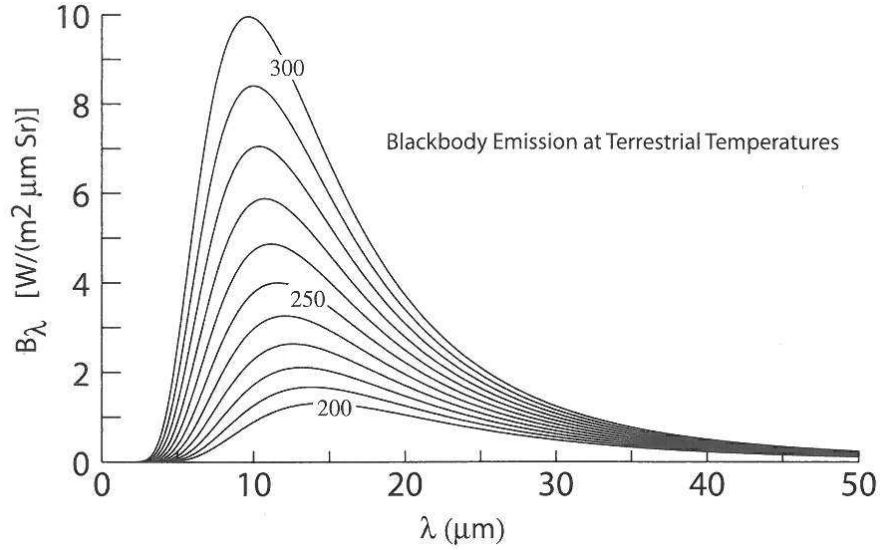


**Figure 4.2:** Planck function  $B_\lambda(T)$  at typical atmospheric temperatures. [extracted from *Petty* (2006, p. 119)]

higher temperatures, while the maximum of the curve moves towards shorter wavelength. It is particularly important to consider that  $B_\lambda(T)$  is always related to a perfect black body and thus,  $B_\lambda(T)$  describes the maximum radiation a body can emit at a given temperature and frequency.

For some applications it is convenient to use the black body temperature or commonly called brightness temperature ( $T_B$ ) as an equivalent measure of its monochromatic intensity.  $T_B$  can be derived, if the Planck function is solved for  $T$ :

$$T_B = B_\lambda^{-1}(I_\lambda), \quad (4.10)$$

where  $B_\lambda^{-1}$  is the inverse Planck function applied to the radiance  $I_\lambda$ . Note that if the emissivity of the source is less than one,  $T_B$  will be less than the source's physical temperature.

When expanding the term  $e^{hc/k_B\lambda T}$  in Eq. 4.9 as a power series it can be shown that under the condition that  $hc \ll k_B\lambda T$  the higher order terms can be neglected and the calculation of  $B_\lambda(T)$  can be simplified using the *Rayleigh-Jeans* approximation:

$$B_\lambda(T) \approx \frac{2ck_B}{\lambda^4}T. \quad (4.11)$$

In the microwave region, the Rayleigh-Jeans approximation (Eq. 4.11) can deviate up to a few percent from the exact inverse Planck function (Eq. 4.10) at low temperatures e.g. when measuring zenith with a ground-based radiometer in one of the window channels (e.g. 40 or 90 GHz). Thus, the  $T_B$  considered in this study are always calculated with the inverse Planck function (Eq. 4.10).

In reality, most particles or media are far from being perfect black bodies. The ratio between the actually emitted monochromatic intensity  $I_\lambda$  of a body and its maximum radiation given by the Planck function  $B_\lambda(T)$  is denoted as emissivity  $\epsilon_\lambda$ :

$$\epsilon_\lambda \equiv \frac{I_\lambda}{B_\lambda(T)}. \quad (4.12)$$

According to (Eq. 4.12)  $\epsilon_\lambda$  can range from  $\epsilon_\lambda = 0$  (“white body”) to  $\epsilon_\lambda = 1$  (black body). Note that  $\epsilon_\lambda$  can also depend on other variables like temperature or the direction  $\vec{\Omega}$ .

The emissivity  $\epsilon_\lambda$  of a body is closely related to its absorptivity i.e. the relation of absorbed radiation to incident radiation. *Kirchhoff's Law* reveals that emissivity and absorptivity are equal for a specific viewing direction  $\vec{\Omega}$  and wavelength  $\lambda$ :

$$\epsilon_\lambda = \alpha_\lambda. \quad (4.13)$$

Again considering radiation propagating along a path  $ds$ , the enhancement due to emission by media along the path can be written as:

$$dI_{emit} = \beta_a(s) B_\lambda(T(s)) ds. \quad (4.14)$$

### 4.3 Scattering

So far only absorption has been considered as a physical process that changes a beam of radiation while propagating through a medium. The other important interaction of an electromagnetic wave with matter is called scattering. In contrast to absorption, the loss of radiation along the path due to scattering is always associated with increased radiation along other directions. Thus, the scattering process is not depleting the incoming energy — unlike absorption — but re-emits it into different directions. A common view on the scattering process is that the electric field of the wave excites the elementary dipoles of the medium (for some medias the dipoles are induced by the external field) that leads to secondary electromagnetic waves transmitted from the oscillating dipole charges.

Scattering properties are in general strongly dependent on the wavelength of the incident radiation and the “dimension”  $r$  of the scattering particle e.g. air molecules, cloud droplets, aerosols and precipitating hydrometeors. The relation of  $r$  to  $\lambda$  can be expressed with the dimensionless size parameter  $x = 2\pi r/\lambda$ .

The size parameter  $x$  can be utilized to identify three main “scattering regimes”:

- For  $x \ll 1$  scattering processes are in the so-called *Rayleigh regime*. Since the wavelength is much larger than the particle, the elementary dipoles are excited by the same electric field at a certain time. As a result, scattering can be described in a simplified way that will be shown in section 4.3.1. An example for Rayleigh scattering in the atmosphere is the scattering of visible light at air molecules.
- *Mie Scattering* is related to  $x$  in the range  $10^3 \gg x \gg 1$ . The main difference to the Rayleigh regime is that the spatially distributed dipoles of the scattering particle experience a different phase of the electric field vector at a certain time. This leads to complex interferences between the secondary transmitted dipole waves and thus, to overall very complex scattering properties. This specific size parameter range should

not be confound with *Mie theory*. Mie theory describes the interaction of radiation with a sphere which can be exactly solved due to the specific symmetry of the sphere (section 4.3.2). A typical example of scattering in the Mie regime is the scattering of mm-sized microwaves at large hydrometeors like snowflakes.

- For  $x > 10^3$ , the wavelength is several orders of magnitude smaller than the particle dimension and geometric optics or ray tracing methods can be applied. An atmospheric example for this region is the scattering of visible light on ice or liquid cloud particles. Unlike the other two scattering regimes this region will be neglected in this study.

The loss of intensity by scattering out of the propagation path can be described similar to the absorption process by a scattering coefficient  $\beta_s$ . Analogous to the absorption (Eqs. 4.7, 4.8), mass or volume related quantities i.e. the scattering cross section  $\sigma_s$  and mass scattering coefficient  $\kappa_s$  can be defined for scattering.

The reduction of incident radiation  $I_0$  after scattering along the path  $ds$  is

$$dI_s = \beta_s(s) I_0 ds. \quad (4.15)$$

The two processes that extinguish radiation along the path — namely absorption and scattering — are commonly summarized as extinction:

$$\beta_e = \beta_a + \beta_s. \quad (4.16)$$

$\beta_e$  is the extinction coefficient in  $\text{m}^{-1}$ . Analogously to absorption and scattering, the extinction cross section  $\sigma_e$  and mass extinction coefficient  $\kappa_e$  can be defined.

A dimensionless quantity that describes the ability of a particle to extinguish radiation is the extinction efficiency  $Q_e$  defined as

$$Q_e = \frac{\sigma_e}{A}, \quad (4.17)$$

where  $A$  is the cross sectional area [ $\text{m}^2$ ] of the particle. Analogously to  $Q_e$  absorption and scattering efficiencies  $Q_a$ ,  $Q_s$  can be defined.

To characterize the relative importance of scattering versus absorption, the single scatter albedo  $\tilde{\omega}$  is defined as

$$\tilde{\omega} = \frac{\beta_s}{\beta_s + \beta_a} = \frac{\beta_s}{\beta_e}. \quad (4.18)$$

For purely absorbing media  $\tilde{\omega} = 0$ , while for only scattering processes  $\tilde{\omega} = 1$ .

After discussing the loss of intensity due to scattering, for a full description of the effects of scattering, one also has to consider that radiation coming from other directions can be scattered into the path of propagation. The information on how much radiation from a wave that propagates in the direction  $\vec{\Omega}'$  will be scattered into the direction  $\vec{\Omega}$  is described by the phase function  $p(\vec{\Omega}', \vec{\Omega})$ . If the phase function satisfies the normalization condition

$$\frac{1}{4\pi} \int_{4\pi} p(\vec{\Omega}', \vec{\Omega}) d\omega = 1, \quad (4.19)$$

the phase function can be interpreted as the probability density function that a photon coming from the direction  $\vec{\Omega}$  is scattered into the direction of interest  $\vec{\Omega}'$ .

For some remote sensing applications like radar and lidar (**L**ight **D**etection and **R**anging) the partition of radiation that is scattered “back” into the direction of the emitting source is especially important. Defining  $\theta$  as the angle between the incident and the scattered wave, the amount of backscattered radiation can be described with the backscattering cross section  $\sigma_b$  [m<sup>2</sup>] which is defined as

$$\sigma_b \equiv \sigma_s p(\theta)|_{\theta=180^\circ}. \quad (4.20)$$

Coming back to the scattered radiation from the entire hemisphere and assuming that Eq. 4.19 is valid, the enhancement  $dI_{ss}$  of  $I_0$  on the path  $ds$  due to scattering from any direction into the path of propagation  $\vec{\Omega}$  can be written as:

$$dI_{ss} = \frac{\beta_s(s)}{4\pi} \int_{4\pi} p(\vec{\Omega}', \vec{\Omega}) I(\vec{\Omega}') d\omega ds. \quad (4.21)$$

It is important to note that if the scattering medium is composed of a distribution of scattering particles (e.g. ice or snow particles), Eq. 4.21 has to be considered for every single particle  $i$  and its specific phase function  $p_i$ . The final scattering properties of the volume are achieved by integrating the single particle contributions. This is justified by the common assumption that the different scattering processes are not interacting with each other.

As mentioned before, only unpolarized radiation is considered in most parts of this study. Since the radiative transfer model (RTM) that is used in the later chapters includes polarized radiation, it is worth to mention the formal differences when including polarization. However, this might be helpful to understand how the original RTE in the RTM reduces to the simplified RTE given in this theoretical section. (For a more detailed description that is out of the scope of this work the reader is referred to (e.g. *Bohren and Huffman, 1983*))

As already defined in section 4.1, information about polarization can be included by using the Stokes vector representation instead of the scalar intensity  $I$ . The relation between the incident and scattered Stokes parameters are described with the  $4 \times 4$  scattering matrix  $\mathbf{S}$ :

$$\vec{I}_{ss} = \mathbf{S} \vec{I}_0. \quad (4.22)$$

From Eq. 4.22 follows that if only the unpolarized components of the scattering process are considered, the matrix element  $S_{11}$  is equivalent to the phase function  $p$ . It is also worth to note that even if the incident radiation is unpolarized, the scattered wave can be partly polarized. Thus, scattering can be seen as an important process in the polarization of former unpolarized radiation. Since the first Stokes component always fulfils the relation in (Eq. 4.4), no radiant energy is “lost”, if only the first Stokes component is considered.

As introduced at the beginning of the section, scattering processes are usually subdivided into different regimes based on the size parameter  $x$ . The two most important regimes for this study are the Rayleigh and Mie regime. The following subsections will thus present the most relevant description and characteristics of these regimes.

### 4.3.1 Rayleigh scattering

As mentioned before, Rayleigh scattering is based on the assumption that all parts of the scattering particle experience the same externally imposed electric field at a certain time. In other words, the wavelength of the incident radiation has to be “much larger” than the particle dimension that can be expressed with the condition  $x \ll 1$ .

From electromagnetic scattering theory it can be shown ([e.g. *Bohren and Huffman*, 1983, 130 pp) that under the restriction  $x \ll 1$  the scattered radiation  $I_{Rs}$  at distance  $d$  by  $N$  small particles with diameter  $2r$  and complex refractive index of the particles  $n$  is

$$I_{Rs} = \frac{8\pi N r^6}{\lambda^4 d^2} \left| \frac{n^2 - 1}{n^2 + 2} \right|^2 (1 + \cos^2 \theta) I_0. \quad (4.23)$$

If  $\left| \frac{n^2 - 1}{n^2 + 2} \right|^2$  is only dependent on the wavelength, the intensity scattered by any sufficient small particle is proportional to  $1/\lambda^4$ . For unpolarized incident radiation the phase function for Rayleigh scattering is given by

$$p(\theta) = \frac{3}{4} (1 + \cos^2 \theta) \quad (4.24)$$

From Eq. 4.24 it follows that Rayleigh scattering is symmetric i.e. the same amount of energy is scattered in the forward and backward directions. The maximum of the phase function is at  $\theta = 0^\circ$  or  $\theta = 180^\circ$ , while the minima are perpendicular to the incident wave. The efficiencies for scattering ( $Q_s$ ), absorption ( $Q_a$ ) and backscattering ( $Q_b$ ) in the Rayleigh limit can be written as (e.g. *Petty*, 2006, p. 355 and p. 377):

$$Q_s = \frac{8}{3} x^4 \left| \frac{n^2 - 1}{n^2 + 2} \right|^2 \quad (4.25)$$

$$Q_a = 4x \Im \left\{ \frac{n^2 - 1}{n^2 + 2} \right\} \quad (4.26)$$

$$Q_b = 4x^4 \left| \frac{n^2 - 1}{n^2 + 2} \right|. \quad (4.27)$$

If the conditions for Rayleigh scattering are fulfilled, the Rayleigh approximation extremely simplifies the RT computations and is especially independent on the particle habit.

### 4.3.2 Mie scattering

The Rayleigh approximation breaks down if  $x \geq 1$ , which implicates that the interactions of every elementary dipole of the particle with the incident wave and with the surrounding dipole fields have to be taken into account. However, if highly symmetric particles like spheres are assumed, it is possible to derive suitable approximations for those particles as well. *Lorenz* (1890) and *Mie* (1908) derived a solution of the wave equations for electromagnetic



radiation for homogenous spheres that is commonly called *Mie-Theory*. Based on the Maxwell equations the wave equation for a planar electromagnetic wave is expressed in spherical polar coordinates. The solution of this separable partial differential equation can be written as an infinite series of products of orthogonal basis functions (sines and cosines), spherical Bessel functions and Legendre polynomials. A complete derivation of the theory is out of the scope of this work and is given e.g. in *Bohren and Huffman* (1983, p. 82-104). The scattering and extinction properties of a sphere can be expressed in a series of length  $i$ :

$$Q_e = \frac{2}{x^2} \sum_{i=1}^{\infty} (2i + 1) \Re(a_i + b_i) \quad (4.28)$$

$$Q_s = \frac{2}{x^2} \sum_{i=1}^{\infty} (2i + 1) (|a_i|^2 + |b_i|^2) \quad (4.29)$$

The complex Mie scattering coefficients  $a_i$  and  $b_i$  are functions of  $x$  and the relative refractive index  $m$  i.e. the ratio of the refractive index of the particle and the surrounding medium.

$$a_i = \frac{m\Psi_i(mx)\Psi'_i(x) - \Psi_i(x)\Psi'_i(mx)}{m\Psi_i(mx)\xi'_i(x) - \xi_i(x)\Psi'_i(mx)} \quad (4.30)$$

$$b_i = \frac{\Psi_i(mx)\Psi'_i(x) - m\Psi_i(x)\Psi'_i(mx)}{\Psi_i(mx)\xi'_i(x) - m\xi_i(x)\Psi'_i(mx)} \quad (4.31)$$

The prime indicates differentiation with respect to the argument in parenthesis.  $\Psi$  and  $\xi$  are the *Ricatti-Bessel functions*,

$$\Psi_i(x) = x j_n(x), \quad \xi_i(x) = x h_i(x) \quad (4.32)$$

where  $j_n$  and  $h_n$  are the *Bessel function* of second and third kind (sometimes called *Hankel function*), respectively.

Usually  $a_i$  and  $b_i$  are calculated numerically, while the length  $i$  of the series that is needed to sufficiently approximate the scattering properties before numerical uncertainties begin to degrade the results. *Wiscombe* (1980) has found  $i$  to depend on  $x$  in the following way:

$$i \sim x + 4x^{\frac{1}{3}} + 2. \quad (4.33)$$

Besides the Mie approximation for spheres, there also exists an approximation for other rotational symmetric particles like ellipsoids or cylinders called *T-Matrix* approach (*Barber and Yeh*, 1975). In later sections, the T-Matrix results will be used and compared to other approaches. However, for a theoretical description of the T-Matrix approach we refer the reader to the related literature. For completely irregular particles (like e.g. snowflakes) the interaction of the incoming field with the single dipoles has to be solved numerically. A common approach called the discrete dipole approximation (DDA) (*Draine and Flatau*, 1994) represents the particle with a matrix of point dipoles and calculates the resulting scattered radiation field. Although this method is by far the most computational expensive, it allows simulating scattering properties of almost any particle geometry given a sufficient number of dipoles.

## 4.4 Radiative transfer equation for a plane-parallel atmosphere

In the previous sections, the sources and losses of radiation due to emission, absorption and scattering were discussed. The different processes can be summarized within the so-called radiative transfer equation (RTE). Combining Eq. 4.6, 4.14, 4.15, 4.21 yields the change of radiation along an infinitesimal path  $ds$  and thus the differential form of the RTE:

$$dI = -\beta_e(s) I_0 ds + \beta_a(s) B(T(s)) ds + \frac{\beta_s(s)}{4\pi} \int_{4\pi} p(s, \vec{\Omega}', \vec{\Omega}) I(s, \vec{\Omega}') d\omega ds. \quad (4.34)$$

The RTE in its differential form illustrates that the intensity along an infinitesimal path  $ds$  is changed by: 1) The extinction of the original radiation  $I_0$  due to absorption and scattering out of the path (first term, right side), 2) the additional radiation originating from emissions of matter along the path (second term) and 3) the enhancement of  $I_0$  due to photons that are scattered into the path from other directions (third term). It is important to note that the RTE is only valid for a state of thermodynamic equilibrium and for an infinitesimal wavelength region (monochromatic). For simplicity, the index  $\lambda$  in Eq. 4.34 and in the following sections will be omitted.

The assumption of a horizontally homogenous atmosphere without any earth curvature is usually called the *plane parallel assumption*. An advantage of this simplification in particular for radiative transfer is that all variables, e.g.  $\beta_e$  that are usually dependent on all three coordinates  $(x, y, z)$ , can be assumed to only depend on height and thus reduces to  $\beta_e(z)$ . This strongly reduces the complexity and therein computational costs of radiative transfer calculations. However, if clouds are considered, the limitations of this assumption become evident: Especially convective clouds with usually strong horizontal gradients of water vapor and high small-scale variability of hydrometeor content and type can not be well represented by the plane parallel assumption. It is important to keep these limitations in mind when comparing later radiative transfer simulations with real observations.

Under the assumption of a plane parallel atmosphere the so far used infinitesimal path length  $ds$  can be reduced to its vertical component  $dz$

$$dz = ds \cos \theta, \quad (4.35)$$

where  $\theta$  is the zenith angle. Introducing  $\mu \equiv \cos \theta$  yields

$$\mu = \frac{dz}{ds} \quad (4.36)$$

For radiative transfer calculations it is convenient to use the optical thickness or optical depth  $\tau$ , measured in this context from the top of the atmosphere, as vertical coordinate,

$$\tau(z) = \int_z^\infty \beta_e(z') dz'. \quad (4.37)$$

With Eq. 4.36 and Eq. 4.37 and using  $\mu$  and  $\phi$  to express  $\vec{\Omega}$  the RTE in the form Eq. 4.34 can be written as

$$\mu \frac{dI(\tau, \mu, \phi)}{d\tau} = I(\tau, \mu, \phi) - (1 - \tilde{\omega}(\tau)) B(T(\tau)) - \frac{\tilde{\omega}(\tau)}{4\pi} \int_{4\pi} p(\tau, \mu, \phi, \mu', \phi') I(\tau, \mu', \phi') d\mu' d\phi'. \quad (4.38)$$

The RTE is usually solved numerically, since an analytical solution exists only for special cases. Under the assumption that the plane parallel assumption is valid and the input parameters are defined correctly, Eq. 4.38 provides the intensity that would be received e.g. by a passive microwave radiometer.

## 4.5 Effective radar reflectivity factor $Z_e$ and attenuation

The sources of radiation received by a MWR are usually the cosmic background radiation and the thermal emissions by the atmosphere and the earth's surface — scattering processes into the measuring direction are not considered as extra sources in this respect, since they only redirect radiation that originates from the aforementioned sources. Actively remote sensing techniques like radar transmit additional radiation into the atmosphere and measure the signal that is scattered back — mainly by hydrometeors. The resulting signal at the radar receiver is thus a superposition of the “natural” radiation field and the backscattered signal. Principally, the backscattered radiation (i.e.  $I(\mu = -1)$  if the radar transmits in zenith direction  $\mu=1$ ) could be calculated with Eq. 4.38, if a further source term expressing the radar transmission would be included.

If the natural signal is small compared to the backscattered signal, however, the RT can strongly be simplified. In order to ensure a comparably low impact of the natural signal, the operational frequencies of radar systems are normally chosen within atmospheric window frequencies (e.g. 35 or 90 GHz) i.e. at frequencies that are minimally affected by gaseous absorption and are mostly transparent. If the radar is measuring towards the “cold” space the contributions of thermal emissions to the received signal can be neglected since in standard radar systems they are below the noise level of the radar receiver.

The total received signal is always composed of a superposition of the backscattered radiation by the hydrometeors within a certain volume that is penetrated by the radar beam:

$$\eta = \int_0^\infty \sigma_b(D) N(D) dD. \quad (4.39)$$

The integral of the backscattering cross sections  $\sigma_b$  multiplied with the particle size distribution  $N(D)$  [ $\text{m}^{-4}$ ] gives the backscatter cross section per unit volume or often called reflectivity  $\eta$  [ $\text{m}^{-1}$ ]. It can be shown (e.g. Petty, 2006) that in the Rayleigh regime  $\sigma_b(D)$  can be expressed in terms of  $D^6$ .  $\eta$  can therefore be written as

$$\eta = \frac{\pi^5}{\lambda^4} |K|^2 \int_0^\infty N(D) D^6 dD, \quad (4.40)$$

$$\text{with } |K|^2 = \left| \frac{n^2 - 1}{n^2 + 2} \right|.$$

The complex refractive index  $n$  is related to the material of the hydrometeors (usually liquid water is assumed in radar applications) at a specific radar wavelength  $\lambda$ . The integral in Eq. 4.40 is the sixth moment of the particle size distribution which defines the radar reflectivity factor  $Z$ :

$$Z \equiv \int_0^{\infty} N(D) D^6 dD. \quad (4.41)$$

In order to express  $Z$  in common units of  $\text{mm}^6\text{m}^{-3}$   $Z$  has to be multiplied by  $10^{18}$ . For radar applications outside the Rayleigh regime,  $\eta$  has to be calculated according to Eq. 4.39. In order to express the received signal in terms of the radar reflectivity factor, the *effective reflectivity factor*  $Z_e$  is introduced with

$$Z_e = 10^{18} \frac{\lambda^4}{\pi^5 |K|^2} \eta. \quad (4.42)$$

Inserting Eq. 4.40 into Eq. 4.42 again yields the radar reflectivity factor  $Z$  as defined in Eq. 4.41. The large dynamic range of the quantities  $Z$  and  $Z_e$  leads to the convention to express them in logarithmic dB-scale:

$$Z_e[\text{dB}] = 10 \log_{10}(Z_e[\text{mm}^6\text{m}^{-3}]). \quad (4.43)$$

In order to account for attenuation of the radar signal, the extinction of every atmospheric constituent  $i$  has to be integrated into a volume extinction coefficient  $\beta_e^{\text{tot}}$

$$\beta_e^{\text{tot}} = \sum_i \int_0^{\infty} \sigma_{e,i}(D) N_i(D) dD. \quad (4.44)$$

With  $\beta_e^{\text{tot}}$  the two-way attenuation coefficient  $\alpha$  [dB] along the path  $s$  (i.e. between 0 and  $s$ ) can be calculated with

$$\alpha(s) = 10 \log_{10} \exp(-2 \int_0^s \beta_e^{\text{tot}}(s') ds'). \quad (4.45)$$

The argument of the exponential function contains the optical thickness along the path  $s$  multiplied by factor two in order to take into account that the radar signal is attenuated twice - at the transmitted and received path. Given a non-attenuated profile of  $Z_e$  along the path  $s$  (e.g. derived from an assumed hydrometeor distribution), the attenuated  $Z_e$  profile can be derived by

$$Z_e^{\text{atten}}(s) = Z_e(s) - \alpha(s). \quad (4.46)$$

All variables are assumed to be in dB; in practical applications  $s$  usually denotes the distance from the radar.

## Chapter 5

# The Radiative Transfer Model RT3 and the Definition of Input Fields

Several numerical models have been developed to solve the RTE (Section 4.4, Eq. 4.38), since an analytical solution of the RTE can only be obtained for special cases. In this study the “RT3” model developed by *Evans and Stephens* (1991) is used. The RT3 solves the polarized, monochromatic RTE for a plane parallel scattering atmosphere containing randomly oriented particles with a plane of symmetry<sup>1</sup>. As already mentioned in Chapter 4, just the unpolarized component of the radiation is considered in this study. Thus, the polarized RTE implemented in the RT3 model is reduced to the one-dimensional RTE (Eq. 4.38). In the RT3, the atmosphere is divided into layers with arbitrary thicknesses that are assumed to be uniform and infinite in horizontal extent. The RT3 solves the RTE with the doubling and adding technique described in detail in *Evans and Stephens* (1991): The input layers are divided into a number of homogenous sublayers. Each sublayer is proven to be thin enough to ensure that the finite difference initialization is accurate. The sublayers are then integrated with the doubling algorithm. For each output level the transmission, reflection, and source of the layers above and below the level are combined with the adding algorithm. The internal radiances are computed from the properties of the layers above and below as well as the incident radiance from the boundaries.

The input parameters are read from a layer-file which contains height and temperature defined at the interfaces between the layers (levels), while gaseous extinction and all scattering properties are defined at the layers between the height levels. The scattering properties of each layer are read in from separate scattering files that contain volume extinction and scattering coefficient as well as the coefficients of the Legendre polynomial expansions of each element of the scattering matrix (only the first element of the matrix is non-zero in this study, since polarization is neglected). As further input parameters solar and/or thermal sources of radiation as well as ground surface properties have to be defined. In this study, the cosmic background radiation is the only non-terrestrial source of radiation that can be approximated by  $B(2.73\text{ K})$ . The thermal emission and reflection from a ground surface can be treated as a Lambertian or Fresnel surface.

In the following subsections, the most relevant input fields and the employed models of absorption and scattering properties for different gases and hydrometeors are described in

---

<sup>1</sup>For the modelling of oriented particles an extension of RT3 is available called RT4 (*Evans and Stephens*, 1995).

more detail<sup>2</sup>.

## 5.1 Surface emissivity

The ground surface (lower model boundary) for the simulations within snowfall is treated as a Lambertian surface i.e. emission is assumed to be isotropic (diffuse) and thus independent of the observation angle. This assumption is backed by experimental observations for snow-covered land surfaces (*Hewison and English, 1999; Harlow, 2009*): Surface emissivity  $e_s$  strongly depends on frequency and snowpack properties. A surface covered by fresh snow has a very high emissivity ( $e_s > 0.9$ ) at frequencies from 24–150 GHz, while crusty snow can have low emissivity values at high frequencies (e.g. even below 0.5 above 90 GHz) (*Yan et al., 2008*). A layer of deep dry snow has values in-between, with 0.6–0.7 being typical values at 90 and 150 GHz. In this study, a constant surface snow emissivity of 0.9 for the considered frequency range 20–150 GHz is assumed for fresh snow. This assumption is justified, since all later model-measurement comparisons are performed for precipitating snow clouds. The constant emissivity of 0.9 is similar to the results found by *Yan et al. (2008)* using satellite measurement retrievals, while it should be noted, that more recent studies by *Harlow (2009)* using airborne measurements found lower emissivity values between 0.6 and 0.8, particularly for 90 and 150 GHz. In order to estimate the impact of the surface emissivity on the passive  $T_B$  measurements during snowfall, a sensitivity experiment is performed in Chapter 6, Section 6.1.3. For the surface temperature the 2m-temperature measured by the DWD at the UFS has been used.

## 5.2 Thermal emissions by gases

The microwave absorption spectrum (equivalent to the emissivity spectrum according to Kirchhoff's law (Eq. 4.13) between 10 and 340 GHz has already been shown in (Section 2.1, 2.2): Besides the comparably low contribution from nitrogen in that frequency region, the most significant emissions by gases originate from the water vapor absorption lines at 22.235, 183.31 and 325.15 GHz, as well as the oxygen absorption complex at 60 GHz and the absorption line at 118.75 GHz. Absorption properties at the window frequency regions are usually obtained by continuum models in addition to the line strength and shape information included in standard gas absorption models. Considering the HATPRO and DPR frequencies, it is found that particularly the 31, 90 and 150 GHz channels are located in regions simulated with continuum absorption models. For the RT simulations in the microwave region, the gas absorption model of *Rosenkranz (1998)* is used, which accounts for the absorption by H<sub>2</sub>O, O<sub>2</sub> and N<sub>2</sub> gases. The line width modification according to the High-resolution TRANsmission molecular absorption database (HITRAN) (*Rothman and Coauthors, 2009*) of the 22.235 GHz H<sub>2</sub>O line as proposed by *Liljegren et al. (2005)* has been taken into account. The accurate description of the continuum absorption is still a challenge in MW radiative transfer and can lead to model-observation differences of a few Kelvin, depending on frequency and water vapor content (*Turner et al., 2009*). Based on long-term 150 GHz observations *Turner et al. (2009)* developed a new description of the water vapor continuum absorption that has been included in this study as well.

---

<sup>2</sup>A complete package of IDL routines has been developed during TOSCA for generating appropriate input fields, running the Fortran RT3 code and converting the output to NetCDF-data files.

## 5.3 Liquid water emission

Cloud droplets are assumed to be mono-dispersely distributed with a radius of  $10\ \mu\text{m}$  and their liquid water refractive index was simulated with a recent model from Ellison (in *Mätzler*, 2006, pp. 431–455). Larger precipitating rain or drizzle drops were not considered in the following calculations, since the simulations are focused on snowfall at 2m-temperatures far below  $0^\circ\text{C}$ . It is important to note that the modelled values of the refractive index for super-cooled water in the microwave region are primarily based on extrapolations from higher temperature regions (*Mätzler*, 2006). Since laboratory measurements for super-cooled water only exist at 9.6 GHz (*Bertolini et al.*, 1982), a large frequency and temperature range has not been verified by laboratory measurements and should be interpreted with care. The most recent observational studies suggest that the model presented by *Stogryn et al.* (1995) is preferable to the Ellison model at 21.38 and 31.5 GHz (*Mätzler et al.*, 2010) and also at 90 and 150 GHz (*Cadeddu and Turner*, 2011) and thus, this model should be implemented in future studies.

## 5.4 Snow scattering

In this section, the state-of-the-art snow particle models used in this study will be described. Their single scattering properties will be discussed in detail, since the snow-MW radiation interactions is the main focus of this study.

### 5.4.1 Snow particle models

#### Rayleigh approximation (RAYL)

It has already been mentioned that for the observation of snow particles at microwave frequencies the Rayleigh approximation (4.3.1) is not valid any more. In order to illustrate the transition from still-Rayleigh scattering regime into Mie-regime dependent on frequency and particle size, the single scattering properties assuming Rayleigh conditions (Section 4.3.1, Eq. 4.25–4.27) are added to the single scattering comparisons of the different snow particle models.

#### Spherical models (MIE)

The easiest and most cost effective way to represent highly complex snow particles is to use spheres and to calculate their scattering properties with Mie theory (Chapter 4.4.3.2). The sphere consists either of solid ice (e.g. *Lhermitte*, 1987, 1990; *Gasiewski*, 1992), equalizing the mass of the snow particle, or is realized with an ice-air mixture (*Liu*, 2004; *Petty*, 2001; *Bennartz and Petty*, 2001) with a bulk snow density similar to in-situ observations. Recently, *Petty and Huang* (2010), investigated the potential of soft spheres with variable density to represent scattering properties of realistic snow aggregates. They constructed four different aggregate structures based on photographic snow observations (Section 3.2, Fig. 3.2) and performed scattering calculations with those particles. Their results show that no soft sphere approximation is able to represent the complete scattering properties of the aggregated snowflakes. While it is possible to construct a soft sphere that matches specific scattering variables of an aggregate, e.g. extinction cross section, the soft sphere approximation can

significantly deviate, if compared to the backscattering properties of the aggregate. The motivation to include soft spheres in these comparisons is due to the fact that they have been widely used (*Petty, 2001; Bennartz and Petty, 2001; Liu, 2004; Surussavadee and Staelin, 2006*) and because they are still implemented in retrievals such as the CloudSat ice water path retrieval (*Austin et al., 2009*) or in MW forward operators like the radar simulator package QuickBeam (*Haynes et al., 2007*).

A slightly different approach is to use oblate spheroid particles consisting again of an ice–air mixture with a certain aspect ratio (i.e. ratio of shortest to longest dimension) (*Matrosov, 2007*). The calculations of the scattering properties are achieved by using the *T–Matrix* method (*Barber and Yeh, 1975*). This method, however, has certain limitations, particularly for very low aspect ratios. Since an aspect ratio of 0.6 has been shown by *Matrosov (1998)* to best represent backscattering by low–density snowflakes, these assumptions were followed in this study and calculations for oblate ellipsoids with aspect ratios between 0.5 and 0.7, together with a horizontal orientation of their longest axis and a standard deviation of their canting angle of  $9^\circ$  were performed. For both soft spheres and ellipsoids we calculate the refractive index of snow using the mixing formula by *Garnett (1904)*:

$$\frac{n_{snow}^2 - n_{air}^2}{n_{snow}^2 + 2n_{air}^2} = P_{ice} \frac{n_{snow}^2 - n_{air}^2}{n_{ice}^2 + 2n_{air}^2}. \quad (5.1)$$

$P_{ice}$  is the ice volume fraction,  $n_{ice}$ ,  $n_{air}$ , and  $n_{snow}$  the complex refractive index of ice, air and snow, respectively. For the refractive index of ice the model by *Warren and Brandt (2008)* has been used. It should be noted that there exist different mixing formulas for ice–air mixtures that reveal significant differences when compared to discrete soft sphere calculations with the DDA (*Petty and Huang, 2010*). For this study, the Maxwell Garnett formula (Eq. 5.1) was chosen in order to be consistent with results of the referred literature about scattering of soft spheres and soft spheroids.

### Pristine ice particles (LIU)

The most common way to simulate more complicated shapes is the DDA (*Draine and Flatau, 1994*). An arbitrary particle is represented by a cubic array of  $N$  point–like polarizable dipoles. To avoid numerical errors, the distance between the single dipoles  $d$  has to be small relative to the wavelength; it is specifically recommended by *Draine and Flatau (2010)* that the particle satisfies the condition  $|n|kd < 0.5$ , where  $n$  is the complex refractive index of the particle and  $k = 2\pi/\lambda$ . The method has been applied to pristine particles like plates, columns, rosettes, dendrites or sector snowflakes (*Liu, 2004, 2008a; Hong, 2007a,b; Kim et al., 2007*) as well as recently to very complex aggregate structures (*Petty and Huang, 2010*) — both sets of studies assume randomly oriented particles. The DDA calculations need the highest computational power, especially if large particles at high frequencies are simulated. It is also important to note that the DDA is an approximation rather than an exact solution like the Mie or T-Matrix theory. The DDA does e.g. not consider multipole–moments or magnetic dipoles. Comparison of DDA calculations for spheres with exact Mie theory revealed that if a sufficiently large number of dipoles is used, the remaining error in scattering properties is less than 10% (*Draine and Flatau, 1994; Liu, 2008a*).



### Snow aggregates (AGG)

It was already mentioned in Chapter 3 that in-situ observations reveal single, pristine ice crystals only to be observed at the lower size limits of the snow size spectrum. Depending on the environment (temperature, humidity, turbulence, etc.), those primary crystals form snow aggregates — also commonly called snowflakes. Due to their large sizes, snowflakes dominate the radiative scattering signatures of snowfall, especially at frequencies above 90 GHz and for radar applications even above  $\sim 24$  GHz (see Chapter 7). It is thus important to include the more realistic snow aggregates in radiative transfer calculations.

Considering the calculation of single scattering properties, two main questions can be identified: 1) How does the mixing ratio of pristine crystals and aggregates change as a function of particle size? 2) Is it possible to find a typical aggregate habit and thus typical single scattering properties of aggregates?

While it is clear regarding the first question that above a size of  $\sim 5$  mm snow is composed of aggregates, it is currently unknown how the mixing of pristine and aggregated snow can be described. Consequently, no particle habit mixtures have been assumed in this study. Unlike for pristine habits it is unclear what the characteristic microphysical properties of aggregates are, since a typical aggregate habit has not yet been defined. The most evident property of aggregates that was found in model studies (*Westbrook et al.*, 2004) and observations (*Field et al.*, 2005) is that the fractal dimension of aggregates is close to two — a variable that is closely related to the exponent in classical mass-size relations for snow (Section 3.3, Eq. 3.3). Thanks to the steadily increasing available computing power, it becomes possible to approximate aggregate scattering properties by simulating them with the DDA method. Two most recently published aggregate scattering properties are based on in-situ measurements: *Ishimoto* (2008) generated fractal aggregates and studied their backscattering properties at 9.8, 35 and 95 GHz using the finite time domain method (FTDM, e.g. *Taflove and Hagness* (2005)). *Petty and Huang* (2010) performed single scattering calculations for different realistic aggregates consisting of dendrites and needles at 13.4, 18.7, 35.6, 36.5 and 89.0 GHz. The two single scattering datasets are both assuming randomly oriented particles. This implicates that the scattering properties of a specific particle have to be averaged over several particle orientations. For numerically stable results it is important to average over a sufficiently large number of particle orientations (*Liu*, 2008a). The aggregate calculations in *Petty and Huang* (2010) are averaged over 125 orientations, while in *Ishimoto* (2008) the averaging was limited to six different orientations. It is likely that particularly the backscattering properties of the results from *Ishimoto* (2008) are affected by the low number of orientation and hence, only the aggregate results from *Petty and Huang* (2010) have been selected here.

In this study, four different particle models are compared including soft spheres (MIE), soft spheroids (T-MAT), pristine crystals (LIU) (*Liu*, 2008a) and snow aggregates (AGG) (*Petty and Huang*, 2010) of maximum particle sizes between  $100 \mu\text{m}$  and 10 mm (for images of the different particle models see Section 3.2, Fig. 3.2). The upper particle size limit of 10 mm was chosen due to current particle size restrictions in the *Liu* (2008a) scattering database. Including different maximum particle sizes would hamper the interpretation of the different habit dependent scattering properties.

#### 5.4.2 Single scattering properties

The absorption and scattering process of an incident radiation field with a single particle is described by the particle's single scattering properties. In this section, mass absorption, mass

extinction and mass backscattering properties — for simplicity the explicit term “mass” is omitted in the following — for the different particle models are compared as a function of particle mass for an exemplary temperature of 268 K. Mass-related quantities give the advantage to use a clearly defined physical property of the particle, in contrast to more ambiguous particle properties such as maximum geometrical size. The single scattering properties are shown for the frequencies: 13.4, 36.5, 89.0 and 160 GHz. These frequencies have been chosen to cover the frequency range considered in this study. Due to a limited available frequency range in some scattering databases (especially AGG) the frequencies in this comparison do not always exactly fit the instrument channels: For example the DPR uses 150 GHz but for AGG only 160 GHz is available. It is, however, assumed that the addition of the most recent AGG calculations gives an important insight in the scattering behaviour of realistic snow aggregates and thus, the frequency mismatch can be accepted for this comparison. It is also important to note that for the LIU and AGG models, calculations exist only for a distinct number of sizes or masses respectively, and linear interpolations are used for values between those discrete points.

### Absorption

In the Rayleigh regime absorption (Section 4.3.1) is independent of particle size or mass, respectively. The values in (Fig. 5.1) for the Rayleigh approximation, soft sphere and T-MAT agree well with this assumption. The models calculated with the DDA (LIU and AGG) and the solid sphere are at all frequencies close together with the Rayleigh approximation for the lowest mass range. With increasing particle mass they increasingly deviate from RAYL with up to a factor of two higher absorption values at the largest masses. The mass dependent increase of absorption of the solid ice sphere indicates that the increasing size parameter and thus, the deviation from the Rayleigh regime is the main reason for the increasing absorption with particle mass. The remaining differences between spherical and DDA models could be due to the process of the random orientation in LIU and AGG: The particle habits are assumed to consist of a defined 3D lattice of solid ice cubes. The final scattering properties (including absorption) for randomly oriented particles are obtained by averaging over the various orientations that can introduce numerical errors due to the limited number of orientations. The orientation independent numerical uncertainties of the DDA compared to MIE theory have been found to be smaller than 10% (*Petty and Huang, 2010*). Even if the discrepancies of the DDA based models and the spherical models especially at the lowest frequency of 13.4 GHz, can not be completely explained, their impact on the particle’s extinction — which is the variable most affecting  $T_B$  changes — is comparably low.

### Extinction

Adding scattering to the former absorption properties of the snow particles one obtains their extinction (Fig. 5.2). In general, extinction increases with increasing particle mass or size, respectively, and higher frequencies. Comparing the absolute values of absorption and extinction, it can be found that scattering reaches 50% of total extinction (i.e. a single scattering albedo of 0.5) at particle masses of 0.2, 0.03, 0.004 and 0.0015 mg for 13.4, 36.5, 89.0 and 160 GHz. This confirms that the strong increase of extinction with mass and frequency is dominated by scattering processes. The slight deviations in extinction of the DDA and spherical models at 13.4 and 36.5 GHz can be explained with the former differences in absorption (Fig. 5.1). In general, extinction can well be approximated by the Rayleigh approximation

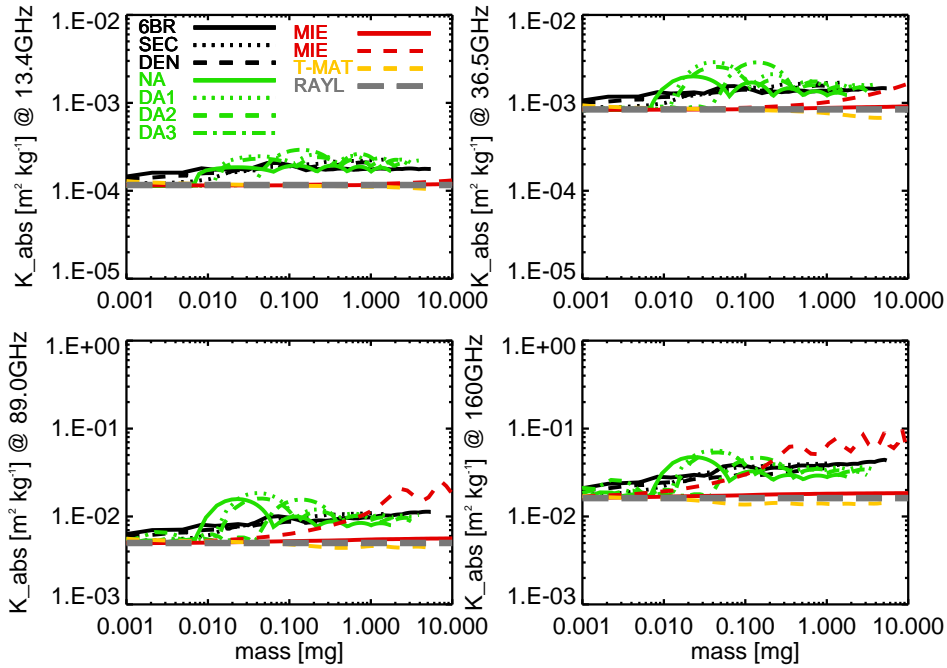


**Figure 5.1:** Mass absorption  $\kappa_a$  [ $m^2 kg^{-1}$ ] of single particles as a function of particle mass [mg] for (top left) 13.4 GHz, (top right) 36.5 GHz, (bottom left) 89.0 GHz, and (bottom right) 160 GHz. The particle models are indicated by the line- and color coding: (black, solid) 6-bullet rosettes (6BR), (black dotted) sector snowflakes (SEC), (black, dashed) dendrites (DEN); (green, solid) needle aggregate (NA), (green, dotted, dashed, dashed-dotted) different aggregates composed of dendrites (DA1–3); (red, solid) Soft sphere with assumed snow density of  $100 kg m^{-3}$ , (red, dashed) Solid sphere with density of solid ice ( $917 kg m^{-3}$ ); (yellow, dashed) Soft ellipsoid (T-MAT) with aspect ratio of 0.6; (grey, dashed) Rayleigh approximation (RAYL).

up to 36.5 GHz. Only at the largest particle masses at 36.5 GHz first deviations from the Rayleigh approximation can be found for T-MAT. The non-Rayleigh behaviour increases further at 89.0 GHz where all particle models at masses larger than 0.1 mg show a slower increase of extinction, compared to the Rayleigh approximation. At 160 GHz all models begin to deviate from the Rayleigh regime already at a particle mass of 0.01 mg. Interestingly, all four aggregates, DEN and the fixed density soft sphere almost perfectly coincide at 89 and 160 GHz while 6bR and SEC have significant higher extinction values and the T-Matrix model constantly shows the lowest values. It is rather surprising that even if a sphere with a constant density for the entire size range is a microphysically unrealistic assumption for snow particles (Section 3.3), Fig. 5.2 clearly reveals that the soft sphere approximates extinction properties very well up to 160 GHz. It is, however, important to note at this point that the soft sphere fails to approximate other single scattering parameters — especially backscattering properties (Chapter 7).

If future snow particle models show a similar coincidence with AGG and DEN and if the deviating particle models (6bR, SEC and T-MAT) can be shown to be not representative for real snowfall, it would imply that mass extinction of a single particle up to 160 GHz is independent on its habit and only a function of particle mass and frequency. Following the

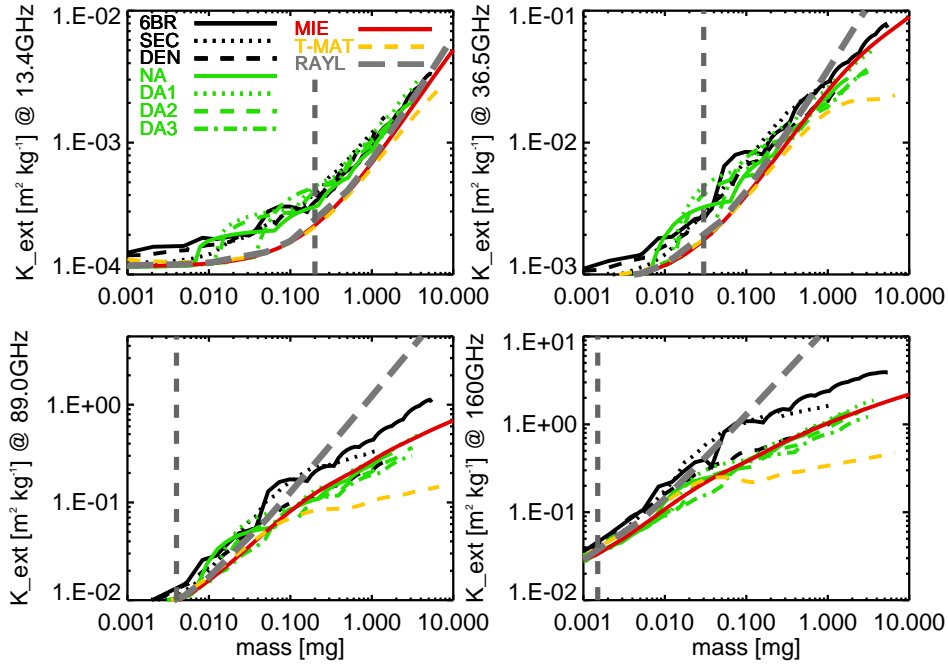


**Figure 5.2:** Same as Fig. 5.1, but for mass extinction  $\kappa_e$  [ $m^2 kg^{-1}$ ] and without solid ice spheres. The dashed vertical line indicates the approximate particle mass where  $\tilde{\omega} = 0.5$ .

**Table 5.1:** Coefficients  $A$  and  $B$  for the average power-law fits (Eq. 5.2) to mass extinction of particle habits NA, DA1-3, and DEN.

Frequency [GHz]	$A$	$B$
13.4	0.001	0.657
36.5	0.022	0.557
89.0	0.226	0.456
160.0	0.951	0.424

approach in *Petty and Huang* (2010), a power law fit has been derived for the overlapping particle habits (NA, DA1-3, DEN) for all four frequencies. The coefficients  $A$  and  $B$  for the power law fit in the form

$$\kappa_e = A m^B, \quad (5.2)$$

for  $m$  in mg and  $\kappa_e$  in  $m^2 kg^{-1}$  are summarized in Table 5.1. The derived coefficients for 36.5 and 89 GHz agree reasonable well with the values derived for AGG in *Petty and Huang* (2010).

### Backscattering

A further common single scattering property besides absorption and scattering is backscattering (Section 4.3). It should be noted that backscattering properties are not needed for the input of the RT3 model. However, they are essential for the later discussion of active

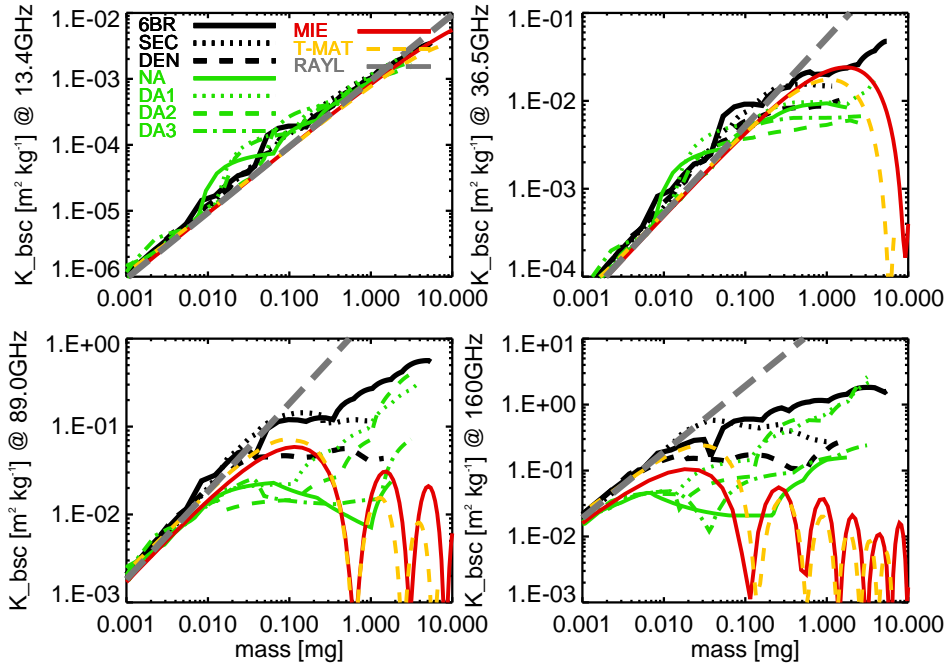


**Figure 5.3:** Same as Fig. 5.1, but for mass backscattering  $\kappa_b [m^2 kg^{-1}]$  and without solid ice spheres.

remote sensing of snowfall in Chapter 7 and thus it is reasonable to move the discussion of backscattering here within the context of other single scattering properties.

Backscattering properties are generally known to be more sensitive to the particle habit than extinction (*Liu, 2004; Hong, 2007b*). Beginning at the lowest frequency of 13.4 GHz, backscattering of the different particle models follows the Rayleigh approximation well and is merely a function of the particle mass (Fig. 5.3). It should be noted that non-Rayleigh behavior occurs at 13.4 GHz only for very large ice particles. However, the results shown in Fig. 5.3 are limited to a maximum particle dimension of 10 mm which is a factor of two smaller than the wavelength of 2.2 cm.

At 36.5 GHz, some models first display Mie resonance effects. As one might expect, the highly symmetric particle models (T-MAT, MIE) show the strongest resonance effects rather than the more irregular AGG and less symmetric bullet rosettes. The backscattering values reveal differences up to two orders of magnitude at the largest mass range. The range of variability due to particle habit in terms of backscattering dramatically increases at 89.0 GHz. MIE and T-MAT reach several new resonance regions with continuously decreasing maximum amplitudes due to the just slightly increasing backscattering cross sections (see also *Matrosov, 2007, Figure 1*) and their quickly increasing particle mass (Fig. 3.5). All LIU particles, on the other hand, almost monotonically increase with particle mass without clear resonance signatures. Similar to most of the LIU particles, the AGG model results do not contain significant resonance “dips”, except for the aggregate type NA that shows a slight dip, but less pronounced than in MIE and T-MAT. Backscattering deviations of more than three orders of magnitude at the largest mass range were also found. The separation of the spherical models (MIE, T-MAT) from the pristine and aggregate models (LIU, AGG) further increases at 160 GHz. While for AGG and LIU a variability of the backscattering properties

of up to one order of magnitude is found, T-MAT and MIE show lower backscattering values by a factor of 10–100 compared to LIU and AGG.

The results of the single scattering comparison of the different snow particle models can be summarized as follows:

- As expected, absorption contributes significantly to extinction at the lower mass range and low frequencies, while scattering dominates extinction at higher frequencies and the larger mass range.
- Absorption is slightly increasing with particle mass for AGG, LIU and solid ice spheres due to non-Rayleigh effects.
- AGG, DEN and constant density soft sphere coincide almost perfectly at the considered frequency and particle mass range.
- At 89 and 160 GHz 6BR and SEC show the highest extinction values, while T-MAT reveals the lowest.
- The deviation from RAYL can be detected for extinction at 36.5 GHz and particle masses larger than 1 mg.
- The backscattering properties, however, deviate at 36.5 GHz even at 0.1 mg from the Rayleigh approximation.
- Variability between the different particle models increases with particle mass and frequency.
- Backscattering properties of the spherical models (MIE, T-MAT) systematically deviate from the complex models (LIU, AGG) with several orders of magnitude lower backscattering values.

The single scattering properties of the single hydrometeor types and extinction of atmospheric gases have to be converted for the RT3 into layer specific properties. For the RT it is assumed that a photon entering a layer of the plane parallel atmosphere scatters just once before leaving the layer. This “single scattering” assumption is in general valid for small measuring volumes and low optical thicknesses (*Battaglia et al., 2010*). These requirements are fulfilled for the cloud systems analyzed in this study and for the beamwidths of the instruments used (Chapter 2). Therefore, multiple scattering effects can be neglected. The single scattering assumption thus allows a simple integration over the individual scattering properties in order to calculate the layer emission, absorption and scattering properties. The derivation of the layer properties are demonstrated for extinction of the hydrometeors:

By integrating the single particle extinction cross sections of the different hydrometeor types  $i$  over the corresponding particle size distribution  $N_i(D_i)$ , one obtains the volume extinction coefficient  $\beta_{e_{lay}}$  for the considered layer:

$$\beta_{e_{lay}} = \sum_i \int_0^\infty N_i(D_i) \sigma_{e,i}(D_i) dD_i. \quad (5.3)$$

$N_i(D_i)$  is assumed to be constant within the layer. The other layer specific properties are derived analogously. The integration over hydrometeor size in Eq. 5.3 is principally from zero

---

to infinity. It is, however, clear that for the numerical integration an upper integration limit has to be chosen. This has been done in a mass-conserving approach and is illustrated here for snow:

$$\int_0^{D^*} N(D) m(D) dD \geq 0.999 \int_0^{\infty} N(D) m(D) dD. \quad (5.4)$$

The upper integration limit  $D^*$  is chosen under the restriction that 99.9% of the hydrometeor mass content is composed by particles smaller or equal to  $D^*$ . If  $D^*$  is larger than the maximum particle size in the scattering database (for snow i.e. LIU and AGG), the scattering properties of the largest available particle in the database is used instead of extrapolating scattering properties. It should be noted that this assumption might lead to potential underestimation of derived radiative (e.g. scattering) properties of the hydrometeor layer.





## Chapter 6

# Passive Remote Sensing of Snowfall

Depending on the measurement geometry, thermal emission by the earth's surface, atmospheric gases and hydrometeors together with the cosmic background radiation are the main sources of radiation received by a MWR. However, the RTE (Chapter 4, Eq. 4.38) demonstrates that not only thermal emission but also scattering of radiation out or into the line of sight of the radiometer can significantly influence the total received intensity. As already shown in Chapter 4, the ability of particles to scatter radiation is always dependent on their size parameter and the real part of its refractive index (Section 4.3.2, Eq. 4.29). For atmospheric gases, the size parameters are lower than  $10^{-6}$  and scattering effects can be neglected in the microwave region. The contribution of liquid cloud droplets and ice crystals with sizes smaller than  $100 \mu\text{m}$  can also be neglected, if size parameters are lower than  $10^{-4}$  at frequencies below 150 GHz. The main contribution to scattered radiation at the considered frequencies in this study belongs to hydrometeors much larger than  $100 \mu\text{m}$  like rain drops, hail, graupel and snowflakes.

Considering a MWR measuring downward under cloud-free conditions — e.g. towards the ocean — it receives the upwelling thermal emission of the ocean and the atmosphere. Adding a snow cloud consisting of liquid water and snowflakes (Fig. 6.1) modifies the signal: First, the signal will be changed due to the emission of the cloud's liquid water. The second influence is more complicated and is related to the frozen water within the cloud. While emission by snow particles is negligible due to the comparably low imaginary refractive index of ice (in the order of  $10^{-3}$ ), the real part of the refractive index is in the order of 1.7–1.8 which leads to non-negligible scattering effects. The snowflakes scatter the emitted radiation from the atmospheric volume below the snow layer out of the measuring direction. As a result, the MWR observes a lower  $T_B$  than it would measure without the snow cloud. This effect is often called  $T_B$  depression. From the previous discussion it is clear that the  $T_B$  depression is strongly dependent on the number, size and habit of the snow particles as well as on the observing frequency used. Several observational studies (e.g. *Katsumata et al., 2000; Bennartz and Petty, 2001; Bennartz and Bauer, 2003*) revealed that the  $T_B$  signals at frequencies greater than  $\sim 90$  GHz are significantly reduced due to thick ice and snow clouds. *Noh et al. (2006)* further showed, that these scattering effects can be used to derive SWP given certain assumptions about size distribution and particle habits.

Satellite observations provide great advantage in terms of a global coverage, while ground-based stations are less affected by the accurate characterizing of surface emissivity. Motivated by the satellite observations, TOSCA addressed as one of its major scientific objectives the question, if the snow scattering effect can be measured in a similar way from a ground-based

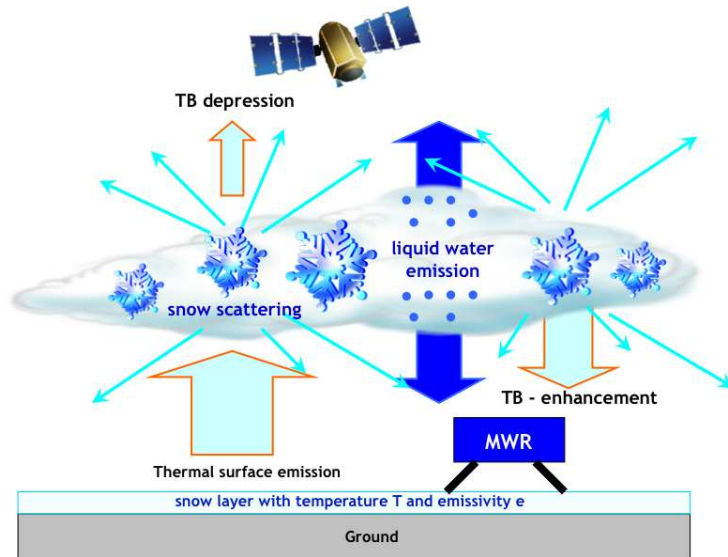


**Figure 6.1:** Illustration of the effects of liquid water and snow crystals on microwave  $T_B$  for a ground-based and a nadir measuring MWR [from Löhnert et al. (2011)].

radiometer in form of a  $T_B$  enhancement (Fig. 6.1). Similar to the  $T_B$  depression observed by a satellite sensor, it is expected that snow scatters thermal emission back into the line of sight of an upward measuring ground-based MWR. With the TOSCA dataset, it was for the first time possible to observe the assumed  $T_B$  enhancement and to validate the effect with other observations.

In this chapter, the effect of  $T_B$  enhancement is first presented for a snowfall case study. The simultaneous measurements during the case study are used to reconstruct the atmospheric state as accurately as possible. The interpretation of the measurements is supported by several sensitivity experiments regarding different snow particle habits, SSD parameterizations, observation geometry and ground emissivities. The case study is supplemented by a statistical analysis of the entire TOSCA dataset in order to illustrate that the discussed  $T_B$  enhancement and sensitivities to other parameters shown for an individual case are in general agreement with other snowfall cases. Finally, the advantage of passive measurements at frequencies up to 340 GHz is shortly discussed with a particular focus on the separability of cloud liquid water from snowfall.

## 6.1 Case study: 08. February 2009

The 8<sup>th</sup> February 2009 was chosen for a detailed analysis because it is characterized by a long-lasting snow event and temperatures between  $-9$  and  $-15$  °C at the surface (Fig. 6.2). This ensures that melting layer effects do not influence the measurements. The data for this time period reveal the presence of super-cooled liquid water in combination with snowfall, which was frequently observed during the entire TOSCA campaign (Löhnert et al., 2011).

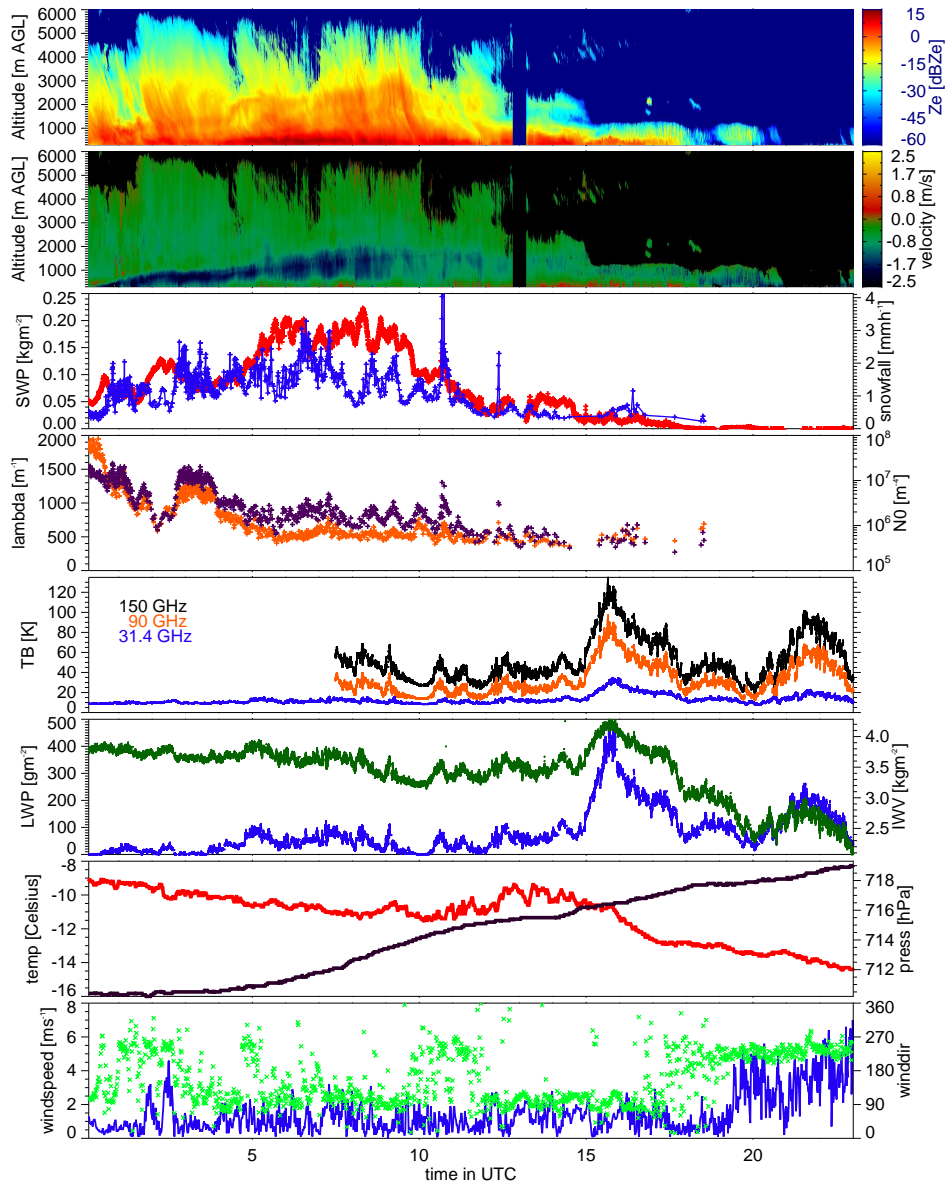


**Figure 6.2:** Selected measurements from a strong snow event on 08. Feb. 2009. From the top: Equivalent  $K_a$ -band effective radar reflectivity factor  $Z_e$  in  $\text{dBZ}_e$ , radar Doppler velocity in  $\text{ms}^{-1}$  (negative values = towards the radar), radar derived SWP in  $\text{kgm}^{-2}$  (red), 2DVD liquid equivalent snowfall rate in  $\text{mmh}^{-1}$  (blue),  $N_0$  in  $\text{m}^{-4}$  (orange) and  $\lambda$  in  $\text{m}^{-1}$  (violet) for exponential SSD from 2DVD, MWR  $T_B$  at 150 (black), 90 (orange) and 31.4 (blue) GHz in K, IWV in  $\text{kgm}^{-2}$  (green) and LWP in  $\text{gm}^{-2}$  (blue) derived from HATPRO, temperature in  $^{\circ}\text{C}$  (red) and air pressure in hPa (black), windspeed in  $\text{ms}^{-1}$  (blue) and direction in degree (light green) [from Kneifel et al. (2010)].

The synoptic situation was characterized by two low pressure systems over Scandinavia and the northern Mediterranean Sea, respectively, leading to a weak flow from the north over the alpine region. Both systems moved slowly eastward during the day, which caused the slight pressure increase seen in Fig. 6.2. The first part of the day, between 0–15 UTC, was

dominated by strong snowfall with a total snow depth increase of  $\sim 25$  cm (manual observation at the summit of the mountain Zugspitze). In this time period the air temperature decreased only slightly from  $-9$  to  $-11$  °C, while between 15 and 24 UTC the temperature declined to  $-15$  °C. The temperature change was accompanied by a decrease of the atmospheric IWV from 4 to  $2 \text{ kgm}^{-2}$  interrupted by a short increase ( $\sim 1 \text{ kgm}^{-2}$ ) between 15 and 17 UTC. The LWP was below  $100 \text{ gm}^{-2}$  until 15 UTC and showed a strong increase up to  $450 \text{ gm}^{-2}$  at 16 UTC, followed by a second peak of  $200 \text{ gm}^{-2}$  at 22 UTC. Cloud radar and ceilometer measurements revealed, those later LWP maxima were due to shallow clouds producing negligible amounts of snowfall. The most distinctive changes in surface wind speed and direction could be seen after 15 UTC, when wind speed increased from  $1\text{--}3 \text{ ms}^{-1}$  to  $3\text{--}6 \text{ ms}^{-1}$  after 19 UTC and the wind direction changed from fluctuating easterly to westerly direction. In brief, the standard meteorological parameters like temperature, humidity and wind speed indicated changing air-masses, particularly around 15 UTC.

Considering the *vertical hydrometeor distribution*, the cloud radar MIRA36 showed a mainly stratiform snow cloud with some remarkable structures: The cloud radar measured the cloud tops at  $3\text{--}5.5$  km altitude AGL from 0–12 UTC, while they decreased down to  $1\text{--}2.5$  km from 12–18 UTC. The cloud bottom was detected by the ceilometer in the lowest layer; also the webcam observations clearly indicated a cloud at ground level. In the first period from 1–12 UTC, the Doppler velocity from MIRA36 showed a region with enhanced fall velocities of  $2.5 \text{ ms}^{-1}$  slightly moving to higher altitudes with time. Since riming is known to strongly influence the fall velocity of snow particles, these higher fall velocities could be an evidence for the presence of super-cooled liquid in that cloud region (Zawadzki et al., 2001).

The *radar derived SWP* values (Fig. 6.2, third panel) ranged between 0.05 and  $0.23 \text{ kgm}^{-2}$  in the most active snow period from 0–13 UTC. The contribution of cloud droplets to the radar reflectivity signal is negligible compared to the contribution of snow: For an equal SWC/LWC of  $2 \times 10^{-5} \text{ kgm}^{-3}$  (e.g.  $\text{SWP/LWP} = 0.1 \text{ kgm}^{-2}$  distributed over a 5 km thick cloud) the reflectivities would be  $-35$  dBz for liquid cloud water and  $\sim 10$  dBz for snow (depending on shape and SSD assumptions). Thus, the influence of liquid water on the observed SWC is lower than 1 % and therefore significantly lower than other uncertainties in Z–SWC relations.

Similar to the radar data, the *liquid equivalent snowfall rate* derived from 2DVD measurements revealed the strongest snow activity between 0–13 UTC with maximum snow rates of  $1.2 \text{ mmh}^{-1}$  (Fig. 6.2, third panel). Radar derived SWP values and 2DVD snowfall rate showed some structural agreement, e.g. in the increasing snow activity from 0 to 8 UTC. It is, however, difficult to directly compare these variables due to the large uncertainties in both the radar Z–SWC relations and the 2DVD derived snow rates as good as wind shear effects, which always cause spatial and temporal shifts.

The *time series of the passive MWR  $T_B$*  for the frequencies 31.4, 90 and 150 GHz (Fig. 6.2, panel 5) represent a superposition of signals from liquid water, snow particles, water vapor and temperature. Thus, in general no simple estimation of hydrometeor contents can be made from the passive microwave measurements alone. Unfortunately, no DPR data (90 and 150 GHz) are available before 7:30 UTC due to software problems, while HATPRO data exist for the whole day. As described in Section 2.1, HATPRO’s low frequency channels (22–31 GHz) can be used to retrieve integrated values of liquid water and water vapor (Fig. 6.2, panel 6). The influence of snow scattering on the total signal is lower than 0.5 K for SWP values below  $0.2 \text{ kgm}^{-2}$  and therefore within the instrument noise level. In combining the cloud radar and 2DVD observations, the significant  $T_B$  enhancements at 90 and 150 GHz around 15 and 22 UTC are identified mainly to originate from liquid water in shallow cloud

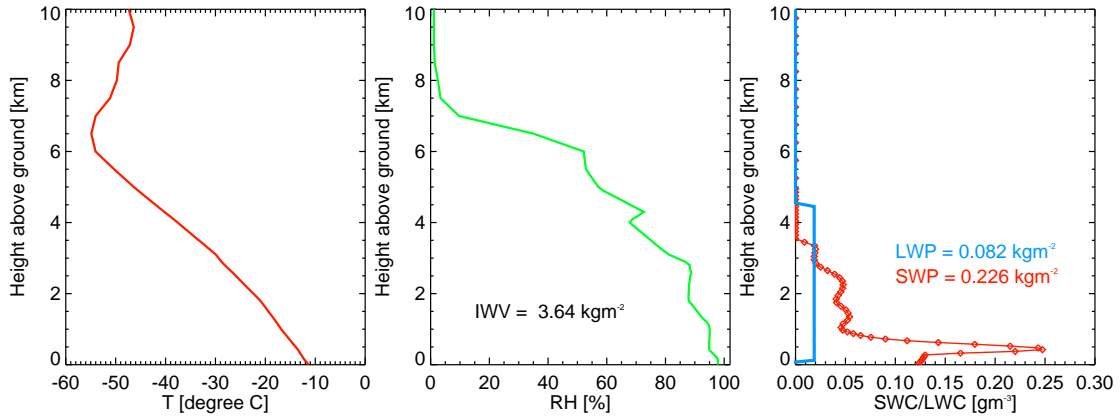


**Figure 6.3:** Reconstructed atmospheric profiles of (left) temperature, (middle) relative humidity, and (right) SWC (red) and LWC (blue) in  $\text{gm}^{-3}$ . (A detailed description of the derivation of the profiles can be found in the text.)

structures (cloud tops  $< 1$  km) with almost negligible amounts of snowfall at ground level.

Based on the available measurements, the state of the atmosphere during the snow event (ten minute temporal resolution) is reconstructed in the following sections as well as possible. Due to lack of better knowledge, several realistic scenarios for snow crystal properties were generated and used as RT model input in an effort to constrain the snow characteristics.

### 6.1.1 Reconstruction of the atmospheric state

Atmospheric profiles and cloud structures used for the RT model input were mainly derived from radiosonde ascents (RS) and MIRA36 measurements. RS ascents from Munich (00, 12, 24 UTC, distance  $\sim 90$  km, height 489 m MSL) and Innsbruck (03 UTC, distance  $\sim 30$  km, height 593 m MSL) were used to reconstruct the profiles of temperature, humidity and pressure. For this purpose, the different RS measurements above the UFS station height were interpolated to ten minute time intervals. This simple procedure was justified because UFS was located above the atmospheric boundary layer and horizontal gradients were weak during the investigated time period. With the RS profiles, the finer vertical structure can be resolved which is not possible to achieve using HATPRO retrievals. On the other hand, HATPRO provides IWV measurements with relatively high accuracy (Section 2.1) and fine temporal resolution. Thus, the humidity profiles were scaled with the ten minute averaged IWV derived from HATPRO to combine the RS highly resolved vertical structure with the high temporal resolution of HATPRO. The resulting temperature profile (Fig. 6.3) reveals the absence of temperature inversions below the tropopause which is located at approximately 6 km height above the UFS. The scaled relative humidity profile shows values larger than 80% up to 3 km height which corresponds well to the height region with reflectivity values larger than  $-10$  dBz (Fig. 6.2, panel 1). However, the cloud radar indicates the cloud top at 5.5 km for the specific time period (08:20 UTC) while the relative humidity values of 55 to 80% between 3 and 5.5 km indicate a lower cloud top height. The lower humidity values of the RS might be explained by a horizontal variability of the cloud top heights between UFS and Munich which can also be seen in the time–height cross section of radar reflectivity factor (Fig. 6.2, panel 1).

For the RT simulations, reasonable assumptions about the profiles of SSD parameters ( $\Lambda$  and  $N_0$ ) and particle shape have to be made. Inserting Eq. 2.2 and Eq. 3.3 into Eq. 3.4 one obtains

$$\Lambda = \left( \frac{N_0 a}{SWC} \Gamma(b+1) \right)^{\frac{1}{b+1}}. \quad (6.1)$$

Eq. 6.1 illustrates that if SWC, particle shape and one of the SSD parameters ( $\Lambda$  or  $N_0$ ) are known, the remaining parameter can be calculated. Assuming a vertically constant intercept parameter  $N_0$  and a certain particle habit, the radar derived SWC constrains the slope parameter  $\Lambda$ . The SWC is derived using the temperature dependent Z–SWC relation presented in Chapter 2, Eq. 2.1: The derived SWC profiles (Fig. 6.3) reveal SWC values up to  $0.05 \text{ gm}^{-3}$  between 1 and 5.5 km height, while the maximum of SWC of  $0.25 \text{ gm}^{-3}$  is found in the layers below 1 km height. It should be noted that the Z–SWC relation is based on scattering calculations of ice–air spheres, unlike the more realistic idealized crystals used for the MW RT here. However, the comparison of their Z–SWC relation with relations derived for the Liu particle shapes reveals it to fall well within the uncertainty range induced by the different Liu particles. The assumption of a vertically constant  $N_0$  is somewhat simplifying, since aircraft studies revealed a temperature dependence (Section 3.1) most likely due to the temperature dependent aggregation processes. Hence, the values for  $N_0$  would vary between  $2.2 \times 10^7 \text{ m}^{-4}$  and  $9.4 \times 10^8 \text{ m}^{-4}$  in the temperature range from  $-10$  to  $-45 \text{ }^\circ\text{C}$ .

Because the real snow particle habits during the snowfall event were unknown, the simulations were performed for the three idealized snow habits 6bR, SEC and DEN described in Chapter 5. The time series of SSD parameters, derived by the method described in Section 2.2.3, showed the highest values for  $N_0$  and  $\Lambda$  during the morning hours (0–5 UTC) with  $1 \times 10^6 \text{ m}^{-4}$ – $2 \times 10^7 \text{ m}^{-4}$  and  $8 \times 10^2$ – $2 \times 10^3 \text{ m}^{-1}$ , respectively. After 5 UTC both parameters remained at relatively low values of  $2 \times 10^5$ – $8 \times 10^6 \text{ m}^{-4}$  for  $N_0$  and  $3$ – $8 \times 10^2 \text{ m}^{-1}$  for  $\Lambda$ , indicating broader SSD with large particles.

### 6.1.2 Influence of liquid water distribution

Since the MWR data do not contain sufficient information about the vertical liquid water profile (*Crewell et al., 2009*) the uncertainty arising from vertically distributing the HATPRO derived LWP of up to  $0.1 \text{ kgm}^{-2}$  has to be estimated. Hence, the LWP was distributed in three different ways: (1) in the lowest model layer (100 m above ground), (2) homogeneously distributed over the total cloud depth (Fig. 6.3) and (3) concentrated at the cloud top. The cloud tops detected by the cloud radar within the selected time period varied between 4500 and 5500 m above ground level (Fig. 6.2) with temperatures ranging from  $-41$  to  $-46 \text{ }^\circ\text{C}$ . That means a temperature difference for the model liquid water between scenario (1) and (3) of 30–38 K. Scenario (3) is surely an extreme assumption because aircraft observations (e.g. *Boudala et al., 2004*) reveal that almost all liquid water is found at temperatures warmer than  $-40 \text{ }^\circ\text{C}$ . Hence, scenario (3) can rather be seen as a lower boundary assumption for the possible liquid water temperature.

In Fig. 6.4 (panel 1 and 3) the  $T_B$  simulated for the three LWP configurations are shown together with the corresponding observations for 150, 90 and 31.4 GHz. While the simulated values are averaged on a ten minute time interval, the measured  $T_B$  are shown in the original 1 s time resolution to illustrate the high temporal variability in the measurements. These

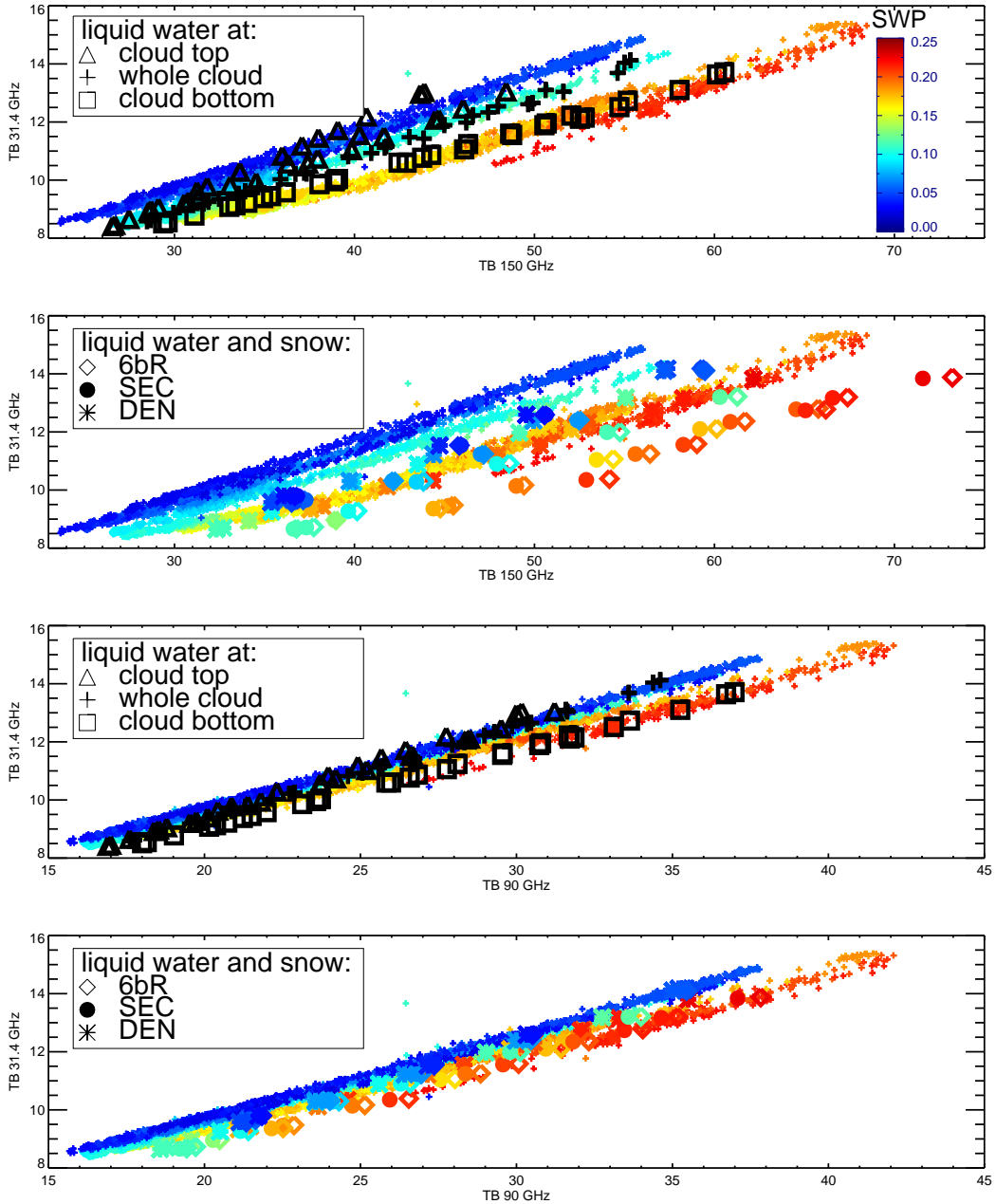


**Figure 6.4:** Comparison of measured and modeled  $T_B$  from 08. Feb. 2009, 07:30–12:40 UTC. The two upper panels show the frequency combination 31.4/150 GHz, while the lower two are for 31.4/90 GHz. The small symbols represent the measurements by the two MWR at a one second time resolution. The color shows the SWP in  $\text{kgm}^{-2}$  derived from MIRA36 measurements. Large symbols show model simulation results for ten minute averaged atmospheric input fields (details see text). Black symbols correspond to simulations with only cloud liquid water (HATPRO derived LWP:  $0\text{--}100\text{ gm}^{-2}$ ) at different cloud positions: cloud top (triangles), cloud bottom (squares) and homogeneously distributed over the total cloud (plus signs). The large colored symbols show the simulations for the scenario of homogeneously distributed liquid water together with snow for  $N_0 = 1 \times 10^7\text{ m}^{-4}$  and three different snow shapes: 6BR (diamonds), SEC (circles) and DEN (asterisks) [from *Kneifel et al. (2010)*].

simulations reveal that the signal emitted by liquid water is mainly a function of mass and temperature. The largest impact of liquid water positioning is found at higher frequencies: For the highest LWP value of  $0.1 \text{ kgm}^{-2}$  the  $T_B$  differences reaches 12 (6) K at 150 (90) GHz, while at 31.4 GHz the differences are below 1 K. Both at 150 and 90 GHz the  $T_B$  generally increase with the temperature of the liquid water layer (i.e., the highest 150 GHz  $T_B$  occur for the liquid water in the lowest layer). The low impact at 31.4 GHz is important because otherwise LWP estimates (based on 22–31 GHz channels) would not be trustworthy.

If compared to measurements, the simulated  $T_B$  agree rather well for both frequency combinations 150/31.4 GHz and 90/31.4 GHz (Fig. 6.4). Unfortunately, the uncertainty induced by the unknown liquid water temperatures is so large that the whole range of observations can be explained by variable liquid water positioning. In order to narrow down the possible range, the cloud radar observations are considered again (Fig. 6.2, panel 2). In the Doppler velocity profile one can detect a band of enhanced fall velocities between 500 and 2000 m. Changes in fall velocity are often connected to a change in particle habits and riming processes. These observations give indication that the scenario of all liquid water being concentrated close to ground is not very likely. If this scenario is excluded, there remains a “branch” of measurements in which enhanced 150 GHz  $T_B$  can not be explained by liquid water alone and are likely to be caused by scattering at snow particles (Fig. 6.4). This is supported by the fact that this branch corresponds to those times when the cloud radar observed the strongest SWP of larger than  $0.15 \text{ kgm}^{-2}$ .

### 6.1.3 $T_B$ enhancement due to snow particles

The RT simulations are repeated adding the SWC profile for different snow habits and SSD parameters. Ten minute averaged SWC profiles are determined using the temperature dependent Z–SWC relation (Eq. 2.1). The simulations have been performed for 6BR, SEC and DEN and a constant  $N_0$  of  $1 \times 10^7 \text{ m}^{-4}$ . Liquid water is assumed to be distributed homogenously in the vertical as an average of the two extreme scenarios: cloud top and base.

The additional contribution of snow causes the  $T_B$  to increase, especially at the higher frequencies (Fig. 6.4, panel 2 and 4). Again, snow particle habit strongly influences the total scattering signal: Similar to the single particle extinction (Section 5.4.2), the maximum  $T_B$  enhancement is caused by 6BR followed by SEC and DEN. At 150 GHz the measurements seem to be covered best by DEN, while at 90 GHz their scattering signals seem to be too small. As mentioned before, however, it is necessary to know the true vertical profiles of liquid water,  $N_0$  and particle habit to fully explain the real  $T_B$  patterns.

### Impact of snow particle habit and SSD

To get a better view of the signal caused by snow, the RT model results can be used to calculate the  $T_B$  differences ( $dT_B$ ) between the pure liquid and the liquid water plus snow case. Again, calculations were performed for the three different snow habits and the two  $N_0$  values (Fig. 6.5). In general, the  $dT_B$  and the snow scattering signal increase with SWP and frequency. For all frequencies and particle habits the differences are higher for lower  $N_0$  values, i.e. SSD containing larger particles. Considering the higher  $N_0$  of  $1 \times 10^7 \text{ m}^{-4}$  (i.e., the narrower SSD), the  $dT_B$  at 159 GHz vary for the largest SWP of  $0.23 \text{ kgm}^{-2}$  between 7 and 18 K depending on particle habit. At 90 GHz the snow signal is lower by a factor of 4.5 and ranges at maximum between 1.5 and 4 K. The snow signal at 31.4 GHz of 0.1–0.2 K is lower than the instrument noise and therefore negligible.



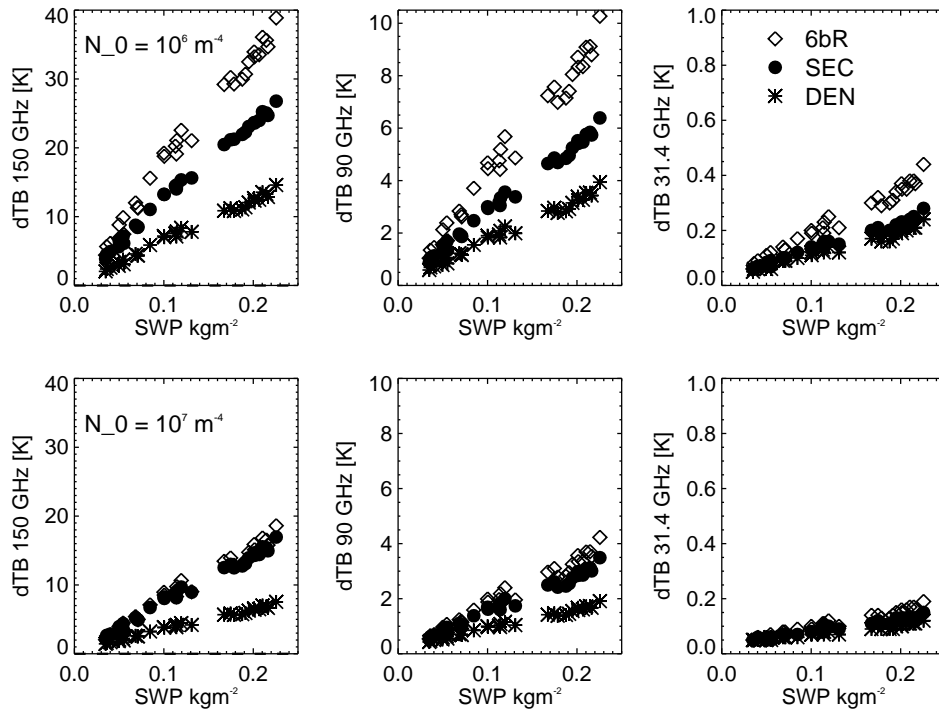


**Figure 6.5:**  $T_B$ -differences ( $dT_B$ ) for (left) 150 GHz, (middle) 90 GHz, and (right) 31.4 GHz based on the data shown in Fig.6.4 between the simulations for only homogeneously distributed liquid water and liquid water combined with snow (SWP in  $\text{kgm}^{-2}$  at the abscissas). The upper part shows the  $dT_B$  for  $N_0 = 1 \times 10^6 \text{ m}^{-4}$  (broad SSD) and the lower part for  $N_0 = 1 \times 10^7 \text{ m}^{-4}$  (narrow SSD). The different symbols correspond to different snow shapes: 6BR (diamonds), SEC (circles) and DEN (asterisks) [from *Kneifel et al. (2010)*].

If  $N_0$  is reduced by a factor of ten (i.e., broader SSD containing large particles) the  $dT_B$  are enhanced: At 150 GHz and high SWP values the  $dT_B$  range from 15 to 40 K depending on snow particle habit. This is by a factor of 2.5 higher compared to the narrower SSD. At 90 GHz the  $dT_B$  increase by a slightly higher factor of 2.75 and range between 4 and 11 K, while at 31.4 GHz the signal is still low with values between 0.2 and 0.5 K.

These sensitivity experiments illustrate the errors due to a wrong SSD or snow particle habit that would arise in a simple 1-channel retrieval even with perfect knowledge of the atmospheric environment (humidity, temperature and liquid water profile). For example, setting the snow particle habit to DEN and  $N_0 = 1 \times 10^6 \text{ m}^{-4}$ , a  $dT_B$  of 15 K at 150 GHz results in a SWP of  $0.22 \text{ kgm}^{-2}$  (Fig. 6.5). Assuming the similar particle type SEC would provide an SWP estimate of only  $0.12 \text{ kgm}^{-2}$  and thus, an error of 50 %. A similar comparison can be done by keeping the snow particle habit constant (e.g. SEC) and changing  $N_0$  from  $1 \times 10^6 \text{ m}^{-4}$  to  $1 \times 10^7 \text{ m}^{-4}$ , again assuming a  $dT_B$  of 15 K. The retrieved SWP changes from  $0.12 \text{ kgm}^{-2}$  to  $0.22 \text{ kgm}^{-2}$  due to the change of the SSD by one order of magnitude.

### Dependence on observation geometry

The observations presented in this study are entirely from ground-based sensors. As mentioned before, clear advantages of ground-based measurements are the capability to collect

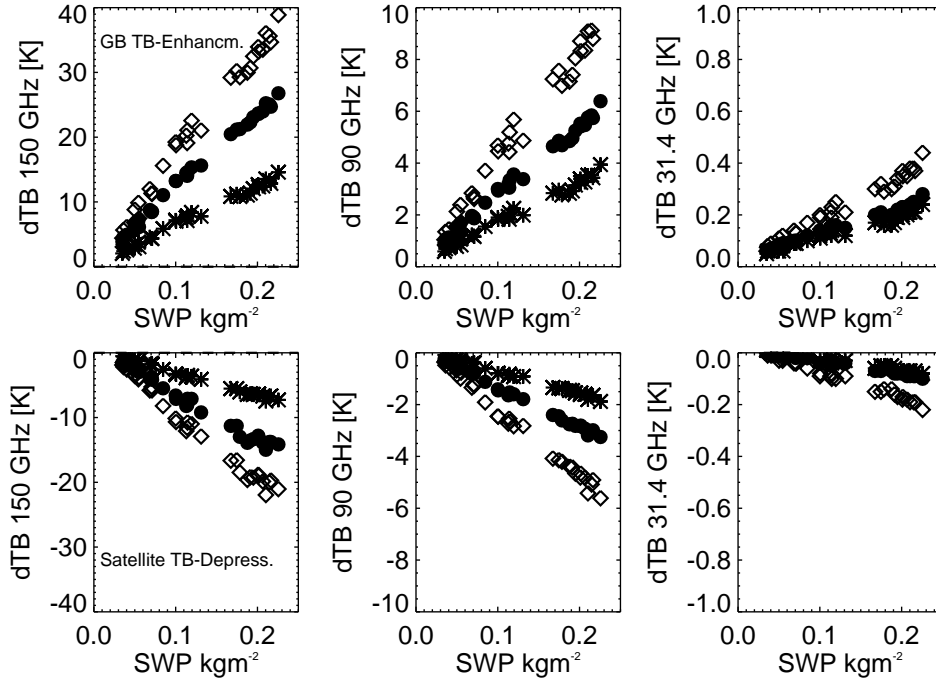


**Figure 6.6:** Same as Fig. 6.5 but only for  $N_0 = 1 \times 10^6 \text{m}^{-4}$ ; Lower panel shows  $dT_B$  for a nadir measuring MWR at 27 km height above ground.

long-term data and the combination of remote sensing data with in-situ observations. On the other hand, one of the main purposes of ground-based data is to provide a test-bed for future satellite retrievals, since only by using space-borne sensors a global coverage can be achieved. Ground-based and space-borne observations of snowfall utilize the same physical process of scattering of thermal radiation at snow particles. Due to the different measurement geometry (i.e. measuring against a cold (space) or warm (ground) background), it is important to consider the question if  $T_B$  depressions and  $T_B$  enhancements differ in terms of sensitivity to snow particle habit or SSD. The  $dT_B$  from Fig. 6.5 with an  $N_0$  of  $10^6 \text{m}^{-4}$  are presented in Fig. 6.6 together with the corresponding  $dT_B$  values simulated for a space-borne nadir measuring sensor (height = 27 km above ground). The comparison of the  $dT_B$  from both measurement geometries reveals that the  $T_B$  enhancement for the ground-based sensor is by a factor of two higher at 150 and 90 GHz compared to the  $T_B$  depression for the satellite sensor. It should be noted that the  $dT_B$  of the two measuring geometries can vary depending on cloud structure and particularly the vertical profiles of liquid water and snow. For instance, experiments with a 2 km thick cloud layer and homogeneously distributed liquid water and snow yielded  $dT_B$  between nadir and zenith measurement geometry of only 1.5 K, however, the  $T_B$  depression is still lower compared to  $T_B$  enhancement. Besides the different magnitude of  $dT_B$  for both measurement geometries the sensitivity to snow particle habit is rather similar: The relative spread of  $dT_B$  values between the three considered snow particle habits is similar to the ground-based case with factors of 2.5 for 150 GHz and 2.75 for 90 GHz.

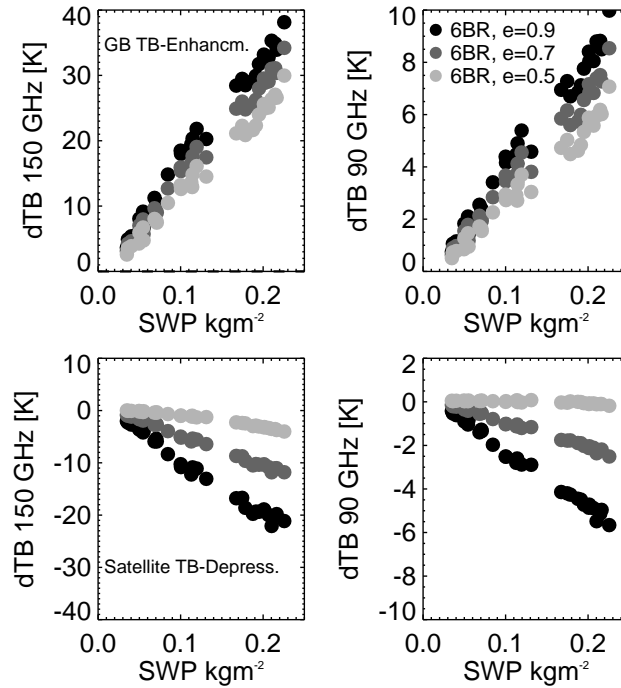


**Figure 6.7:** Same as Fig. 6.6 but only for 150 and 90 GHz and only for snow particle habit 6BR. The different grey scales indicate different ground surface emissivities: (light grey) 0.5, (mid grey) 0.7, and (black) 0.9.

### Impact of surface emissivity

As already mentioned in Section 5.1 the surface emissivity in the frequency range between 30 and 150 GHz is mainly a function of the temperature and surface properties of the ground. For the presented case study it is proven that the surface was covered by fresh fallen snow having a typical emissivity of 0.7–0.9. However, to interpret the  $T_B$  enhancement for more general conditions — e.g. ground covered by older and crustier snow or a mixture of snow and uncovered ground — one has to consider the influence of emissivity changes on the  $dT_B$ . Variability of surface emissivity is known to strongly affect satellite radiometric measurements (*Skofronick-Jackson et al., 2004; Noh et al., 2009*), but it also has an impact on ground-based measurements: the higher the ground emissivity the stronger the up-welling radiation leaving the surface and the larger the radiation scattered back to the ground by the snow.

To quantify this effect, RT simulations were performed with the exact same input fields but with surface emissivities varying from 0.5 to 0.9. For simplicity, the  $dT_B$  are only calculated for  $N_0 = 10^6 \text{m}^{-4}$  and snow particle habit 6BR. For the ground-based scenario (Fig. 6.7, upper panel) the assumption of a surface emissivity of 0.5 instead of 0.9 leads to 30 % (50 %) smaller  $T_B$  enhancements at 150 (90) GHz. The  $dT_B$  variability due to a considerably large change of surface emissivity is thus much lower compared to the uncertainties introduced by different particle habits and SSD parameterizations (Fig. 6.5). An explanation of the different sensitivities to emissivity changes at 90 and 150 GHz can be found, if a second source to the total upwelling radiation  $I_{\uparrow}$  is considered:

$$I_{\uparrow} \sim e_s B(T_{surf}) + (1 - e_s) I_{\downarrow}. \quad (6.2)$$

The total upwelling radiation  $I_{\uparrow}$  is proportional to the ground surface emission  $B(T_{surf})$  with the surface temperature  $T_{surf}$  and is multiplied with the surface emissivity  $e_s$ . The second term describes the portion of downwelling radiation  $I_{\downarrow}$  from the atmosphere that is reflected by the surface which is proportional to  $(1 - e_s)$ . For frequency regions where the atmosphere is optically thin and therefore  $I_{\downarrow}$  small, the reflected part is also small and thus  $I_{\uparrow}$  is dominated by surface emission. For higher frequencies with increasing optical thickness of the atmosphere, the second term partially compensates variability introduced by emissivity changes of the ground surface, which leads to a smaller sensitivity at 150 GHz to emissivity variations compared to 90 GHz.

Even though this study is focused on the ground-based perspective, the sensitivity of  $dT_B$  to emissivity variability is again considered for the satellite measurement geometry as well (Fig. 6.7, lower panel). The comparison reveals a bigger change of the  $dT_B$  from satellite compared to ground-based instruments. Due to the reduced ground surface emissivity, the observed  $T_B$  depression almost entirely vanishes. At 150 GHz and with the largest SWP the  $dT_B$  decreases from -21 to 4 K, while at 90 GHz the values decrease from -6 to 0 K. A thorough discussion of the differences due to observation geometry would require a more detailed analysis of the radiant flux at different height levels and is thus out of the scope of this study. However, it is clear that the different background radiation fields (i.e. warm ground surface versus cold space) and the different propagation directions for the signals at the receiver are the main reasons for the different  $dT_B$  sensitivities.

The sensitivity experiments for different snow particle habits, SSD parameterizations and ground surface emissivities revealed:

- The influence of the particle habit and changes of  $N_0$  to the snow scattering signal are in the same order of magnitude, given the chosen parameter range.
- For ground-based sensors, the uncertainty due to microphysical properties of snowfall dominates the  $T_B$  enhancement and is roughly four times larger than the effect of varying ground surface emissivities.
- Given the same surface and atmospheric state, the  $T_B$  change due to snowfall observed by a satellite is systematically lower by a factor between 1.5 and 2. Further, the sensitivity of the  $dT_B$  is much larger compared to the ground-based geometry and in a similar range as the  $dT_B$  caused by snow particle habit and SSD variability.

## 6.2 Statistical analysis of $T_B$ enhancement

The RT simulations shown in the former case study revealed that while at the lower frequencies (31 GHz) the signal is dominated by liquid water and gaseous emissions,  $T_B$  become increasingly affected by snow scattering towards higher frequencies. In *Löhnert et al. (2011, Fig. 6)*, the entire TOSCA dataset of HATPRO and DPR observations has been analyzed with respect to IWV and SWP in a similar way as it was done for the presented case study (Fig. 6.4). All observations during time periods when snowfall was detected at ground level have first been separated with respect to their radar derived SWP values. Considering all

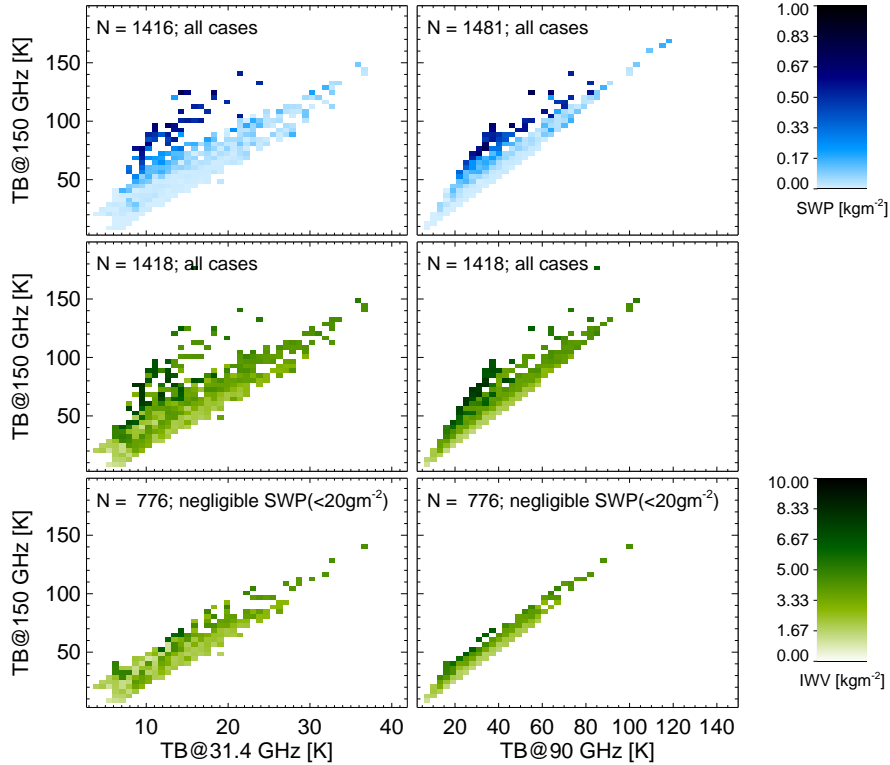


**Figure 6.8:**  $T_B$ – $T_B$  scatterplots as function of (upper) SWP and (middle/lower) IWV: (left) 31 GHz  $T_B$  versus 150 GHz  $T_B$  and (right) 90 GHz  $T_B$  versus 150 GHz  $T_B$ . For (bottom), only cases for SWP smaller than  $20 \text{ gm}^{-2}$  are shown [from *Löhnert et al. (2011)*].

cases with negligible amount of radar derived SWP ensures that the signal mainly originates from cloud liquid water and water vapor. The  $T_B$  for the almost snow-free cases lie approximately on a line when plotting the  $T_B$  values as scatter plots (Fig. 6.8). The larger variability in the 31–150 GHz combination can be attributed to the different temperature dependence of the liquid water emission at 31 and 150 GHz. At 31 GHz the same amount of liquid water gives rise to higher  $T_B$  at cooler ambient temperature than at warmer temperature, whereas this relation is opposite at 150 GHz.

When including cases with larger SWP in the analysis (Fig. 6.8, middle and upper panel) the patterns change: While in Fig. 6.8 (lower panel) the  $T_B$  are lying approximately on a straight line, the  $T_B$  scatter now includes secondary branches towards higher 150 GHz  $T_B$ . Although those areas are connected to higher IWV values, the IWV alone is not sufficient to explain the enhanced 150 GHz  $T_B$ , since the former snow-free comparison are within a similar IWV range, however, without showing the branched  $T_B$  structures. Regarding the same observations as a function of the radar derived SWP (Fig. 6.8, upper panel), it becomes evident that the enhanced  $T_B$  are correlated with SWP, especially at 150 GHz. The observed  $T_B$  enhancements at 150 GHz (90 GHz) range from a few Kelvin up to the order of about 70 K (50 K), apart from a few outliers where  $T_B$  enhancements can even be higher.

Despite the remaining uncertainties that have been discussed in this chapter, the  $T_B$  enhancement in high frequency ground-based MW observations has been shown to be a real effect that can be used for snowfall retrievals, if the residual parameters can be constrained.

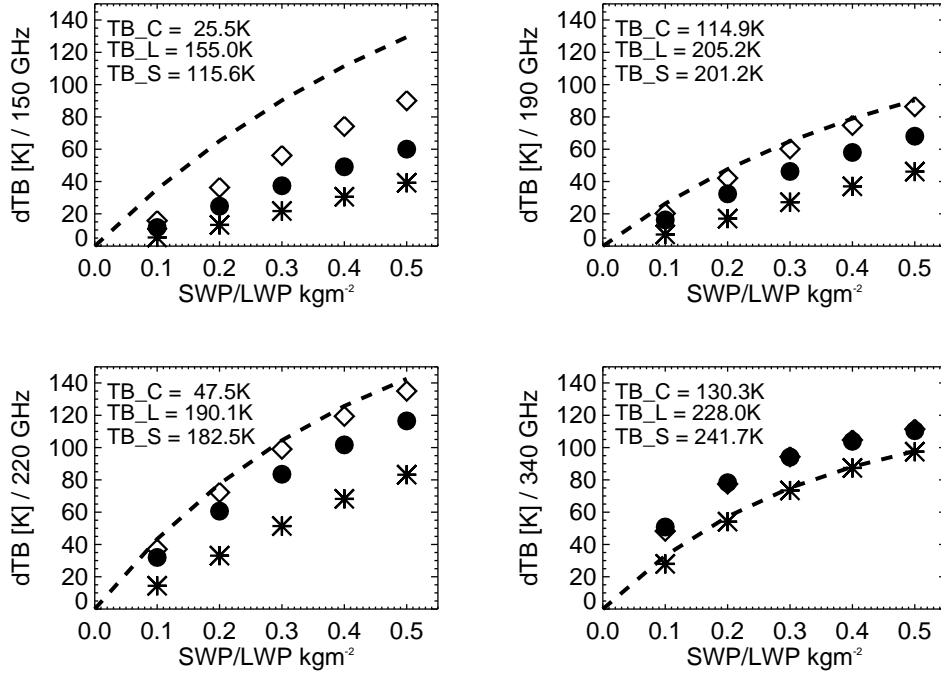


**Figure 6.9:** Simulated  $dT_B$  for (upper left) 150, (upper right) 190, (lower left) 220, and (lower right) 340 GHz. A homogenous 2 km thick cloud layer has been assumed containing (dashed line) only liquid water or only snow (symbols). Corresponding SWP and LWP values of the cloud in units of  $\text{kgm}^{-2}$  are shown at the abscissa. The maximum absolute  $T_B$  values for the scenarios ( $T_{B,C}$ ) clear sky conditions, ( $T_{B,L}$ ) only liquid water, and ( $T_{B,S}$ ) only snow water are given in the upper left corner of each subpanel. The snow particle habits indicated by the symbols are the same as in Fig. 6.6.

### 6.3 Outlook towards frequencies larger than 150 GHz

From the MW spectrum (Section 2.1, Fig. 2.2) it is obvious that the  $T_B$  enhancement can be expected to further increase at frequencies larger than 150 GHz. Measurements with airborne instruments (e.g. *Skofronick-Jackson* et al., 2003) confirm this assumption, showing significantly higher  $T_B$  depressions at 190, 220 and 340 GHz. The expected magnitude of  $T_B$  enhancement at those higher frequencies, the dependence on snow particle habit and the relation of snow scattering to liquid water emission shall be shortly discussed with help of a theoretical RT experiment: A homogenous cloud layer located 1 km above the UFS with 2 km thickness is assumed, while the atmospheric profiles are taken from the case study as shown in Fig. 6.3 — except the relative humidity which is set to 100 % within the cloud layer. Liquid water and snow are distributed homogeneously within the cloud, assuming an intercept parameter for snow of  $N_0 = 1 \times 10^6 \text{m}^{-4}$  and a ground surface emissivity of 0.9 similar to the former case study. In order to estimate the  $T_B$  changes due to liquid water and snow, the  $dT_B$  are calculated between a clear-sky atmosphere and a cloudy atmosphere containing liquid water or snow<sup>1</sup>.

In Fig. 6.9 the  $T_B$  increase due to a pure liquid water cloud and a pure snow cloud are

<sup>1</sup>Unlike here,  $dT_B$  in the former case study was calculated as difference between atmosphere + liquid water cloud and atmosphere + liquid water + snow.

shown for 150, 190, 220 and 340 GHz. The absolute  $T_B$  values for clear-sky conditions show for 190 and 340 GHz with 115 and 130 K significantly higher values compared to 150 and 220 GHz with 25.5 and 47.5 K, respectively. This can again be understood with the help of the MW spectrum (Section 2.1, Fig. 2.2) which shows that 150 and 220 GHz are far away from absorption lines, while 190 and 340 GHz are still in proximity of strong water vapor absorption lines.

At 150 GHz the liquid water emission clearly dominates the snow scattering signal. The influence of the water vapor absorption line at 183 GHz can still be observed at 190 GHz: Due to higher clear-sky opacity (warmer clear-sky background) the  $dT_B$  from liquid water are even lower compared to 150 GHz, while the snow  $dT_B$  are in a similar range. Only when moving towards 220 GHz, the snow scattering signal reaches a similar magnitude as the liquid water emission, though only for the snow particle habit 6BR. Finally, at 340 GHz, snow scattering is even slightly larger than liquid water emission. The sensitivities of snow  $dT_B$  to snow particle habit are rather similar at the different frequencies: The lowest values are obtained with DEN, followed by SEC and 6BR. Only at 340 GHz SEC and 6BR overlap and reveal the lowest differences between the snow particle habits.

The RT experiments including frequencies up to 340 GHz reveal that under low water vapor condition higher frequency channels, especially at window frequencies, provide increasing sensitivity to snowfall. It can be speculated that due to different sensitivities to snow and liquid water a combination of different frequencies allows distinguishing the signal from liquid water and snow. Unfortunately, the distinction of different snow particle habits remains a challenge even with a combination of several frequencies. However, future studies including a larger set of realistic snow particle habits might find a way to constrain SSD parameters similar to the technique developed by *Deeter and Evans* (2000) for spherical particles. It is clear that such an experiment can only give a limited insight into the different sensitivities of passive MW signals to the variety of different variables. An unambiguous conclusion about the usefulness of different frequency combinations has to include e.g. the vertical distribution of snow and liquid water content as well as SSD variability. This can only be obtained by an extensive retrieval study.





## Chapter 7

# Active Remote Sensing of Snowfall between 20 and 95 GHz

A general limitation of passive techniques is that vertical profiles can only be derived for atmospheric constituents that provide significant absorption features (e.g. the water vapor absorption line at 22 GHz or the oxygen absorption complex at 60 GHz). For liquid water, only the vertically integrated contents can be derived (*Crewell et al., 2009*), since liquid water emission increases continuously with frequency without a distinct line-structure. The same argumentation is valid for snow: The frequency dependent increase of snow extinction (Section 2.1, Fig. 2.2) caused by scattered thermal radiation at the snow particles (Chapter 6, Fig. 6.1) is found to occur without any resonance effects. A range dependent information about the hydrometeor distribution is thus usually obtained by radar systems that transmit a signal into the atmosphere and receive the backscattered power from the hydrometeors.

Precipitation radars usually operate at frequencies in the X-, C- or S- bands (3–11 cm wavelength) within which precipitating particles still adhere to the Rayleigh regime (Section 4.3) and the attenuation of the signal is comparably low. Higher frequency systems (3–8 mm wavelength, W- and K<sub>a</sub>-band) are used to investigate non-precipitating clouds and are thus often called cloud radars. Attenuation, especially due to liquid water, increases rapidly to higher frequencies and limits the use of cloud radars for the investigation of clouds containing large amounts of liquid precipitation. Since cloud radars are sufficiently sensitive to cloud ice, and since attenuation by ice is low compared to rain, cloud radars have been increasingly used to analyze ice and snow clouds (e.g. *Matrosov et al., 2008*).

In the first part of this chapter, the collocated measurements of the cloud radar MIRA36 (Section 2.2.1) and the low-power MRR (Section 2.2.2) are used to analyze the potential and limitations of the MRR for snowfall measurements. In the second part the potential of multi-frequency radar observations is explored within a theoretical simulation study.

### 7.1 Intercomparison: Cloudradar MIRA36 vs. MRR during snowfall

The deployment and operation of ground-based cloud radar systems is expensive due to the high logistic efforts of installation and maintenance as well as large power consumptions. This is particularly true for mountainous or polar regions, where snowfall measurements are of special importance. If the focus can be narrowed to the lowest 3 km, a feasible solution in

such an environment can be the use of low power radar systems such as the 24.1 GHz FM–CW Micro Rain Radar (MRR) (Section 2.2.2). The MRR was originally designed to provide vertical profiles of rain drop size distributions (DSD) by exploiting the Doppler spectra of the falling hydrometeors. It has been widely used for the observation of rain microphysics (Löffler-Mang et al., 1999; Peters et al., 2005; Tokay et al., 2009; Van Baelen et al., 2009) and the investigation of bright band properties (Cha et al., 2009). Its potential for the observation of snowfall has not yet been investigated.

The dataset of collocated measurements of the high–end cloud radar MIRA36 and the MRR collected during TOSCA was used to estimate the MRR’s capabilities to detect snowfall. This will be described in detail in the following section. In order to be able to directly compare the  $Z_e$  of the two radar systems, the MRR data had to be processed in a first step without rain specific assumptions. In order to correct for the 11 GHz frequency difference between MIRA36 and MRR, an averaged correction has been derived based on theoretical snow particle models. The  $Z_e$  measurements from both radar systems have been additionally corrected for potential biases by comparing the  $Z_e$  from the lowest range gate with calculated  $Z_e$  from an optical disdrometer (Chapter 2) during rainfall conditions — similar to the method described in Löffler-Mang and Blahak (2001).

### 7.1.1 Development of snow specific MRR data processing

In contrast to the pulsed transmission of the MIRA36, the MRR operates in a continuous mode and applies the FM–CW technique (Strauch, 1976) to obtain the range information of the backscattered signal. As a result of the MRR frequency modulation, the frequency of the received backscattered radiation deviates from the frequency of the currently transmitted signal due to the time delay caused by the distance of the backscattering particles from the radar. An additional frequency shift is produced by the Doppler shift  $f_D$  caused by the velocity of the particles relative to the radar. The MRR processing unit performs a two–dimensional Fourier analysis as described e.g. by Strauch (1976) to remove the range/Doppler ambiguity of FM–CW radars. As a result, range resolved Doppler–induced power spectra are obtained which can be related to particle distributions via size dependent fall velocities Peters et al. (2002). The operational software of the MRR automatically derives mean fall velocities, a rain DSD, a rain rate and a corresponding radar reflectivity factor  $Z$  assuming liquid hydrometeors. For solid hydrometeors like snow the pertinent assumptions are violated; thus, a simple adjustment of the operational output to snowfall is incorrect:

- 1.) The DSD for raindrops is computed from the terminal fall velocity of the raindrops based on an assumed size–terminal velocity relation (Atlas et al., 1973). For snow particles, the size dependence of the terminal fall velocity is much weaker and — in addition — depends heavily on snow particle habit and the degree of riming (e.g. Brandes et al., 2008).
- 2.) The backscattering cross section of spherical raindrops (oblate spheroids are not considered by the MRR software) can accurately be calculated via Mie theory (Section 4.3.2) (e.g. Löffler-Mang et al., 1999). Such relations are needed to derive the DSD from the observed backscattered radiation (see Peters et al. (2005) for a detailed description). Spherical and even spheroid approximations are, however, inappropriate particularly for larger snowflakes (e.g. Petty and Huang, 2010). Hence, the backscattering properties are largely dependent on snow particle habit.

- 3.) Due to the low fall velocities of dry snowfall, turbulent air motion and larger scale updrafts strongly affect the Doppler spectra and cannot be easily separated from the fall velocity signals, even if snow particle habit and the degree of riming is known.
- 4.) The output reflectivity  $Z$  of the MRR standard product<sup>1</sup> is not derived from the spectrally (according to the Doppler spectrum) resolved reflectivity, but from the inferred DSD via the 6th moment of the DSD (Eq. 4.41). This relation cannot be used mainly because of 1.) and 3.).

The arguments given in 1.) to 4.) reveal that a SSD from the Doppler spectra can not be derived analogously to the rain case. To avoid any rain specific assumptions, the effective reflectivity factor  $Z_e$  [ $\text{mm}^6\text{m}^{-3}$ ] (Eq. 4.42) is used instead, which is derived from the Doppler spectra using

$$Z_e = 10^{18} \frac{\lambda^4}{\pi^5 |K|^2} \sum_{i=1}^{64} \eta_i(f_{D,i}). \quad (7.1)$$

For  $|K|^2$  a constant value of 0.92 has been assumed according to the dielectric refractive index of liquid water at the considered frequencies (Section 4.5, Eq. 4.40);  $\eta_i(f_{D,i})$  is the spectral reflectivity [ $\text{m}^{-1}$ ] in dependence of the  $i$ th Doppler frequency bin  $f_{D,i}$  stored in the MRR standard data product. Since attenuation of the radar signal by dry snowfall is negligible at  $K/K_a$ -band (e.g. *Matrosov, 2007*) no attenuation correction has to be applied to  $\eta_i(f_{D,i})$ . In the current MRR software version  $\eta$  are corrected for attenuation assuming liquid rain; this correction has to be disabled for snowfall observations.

### 7.1.2 Dealiasing of the Doppler spectrum

Due to the Fourier transformation procedures performed by the MRR firmware, the frequency resolution is limited to 30.52 Hz, which corresponds to a terminal fall velocity resolution of  $0.189 \text{ ms}^{-1}$ ; thus, the maximum number of 64 frequency bins limits the fall velocity range between 0 and  $11.93 \text{ ms}^{-1}$ . The MRR assumes only positive fall velocities (defined here as movements towards the radar). This assumption is not always applicable to snowfall due to its much higher sensitivity to turbulence and related particle motions. In fact, the MIRA36 Doppler velocity measurements during TOSCA revealed frequent occurrences of upward particle motions particularly at lower height levels, while significant downward motions could not be identified. Such updrafts (or negative fall velocities) are currently misinterpreted by the MRR software as extremely high fall velocities due to the well-known velocity-range aliasing typical for FM-CW Doppler radars (e.g. *Strauch, 1976*). Such artifacts are corrected by the assumption, that dry snowflakes do not exceed fall velocities of  $5.87 \text{ ms}^{-1}$ . Thus, the part of the spectrum corresponding to velocities above  $5.87 \text{ ms}^{-1}$  (frequency bins 33 to 64) is transferred to the negative fall velocity range ( $6.06$  to  $-0.189 \text{ ms}^{-1}$ ) of the succeeding (higher) range gate (Fig. 7.1). The FM-CW principle requires an appropriate filtering of signals with time independent phase. As a consequence, the original frequency bins  $i = 64, 1, 2$  were disturbed and were omitted. However, due to the dealiasing of the spectrum the disturbed bins move from the border to the center of the spectrum and are reconstructed by linear interpolation

<sup>1</sup>The MRR standard product is named *Instantaneous Data* or – averaged over an arbitrary time – *Average Data*.

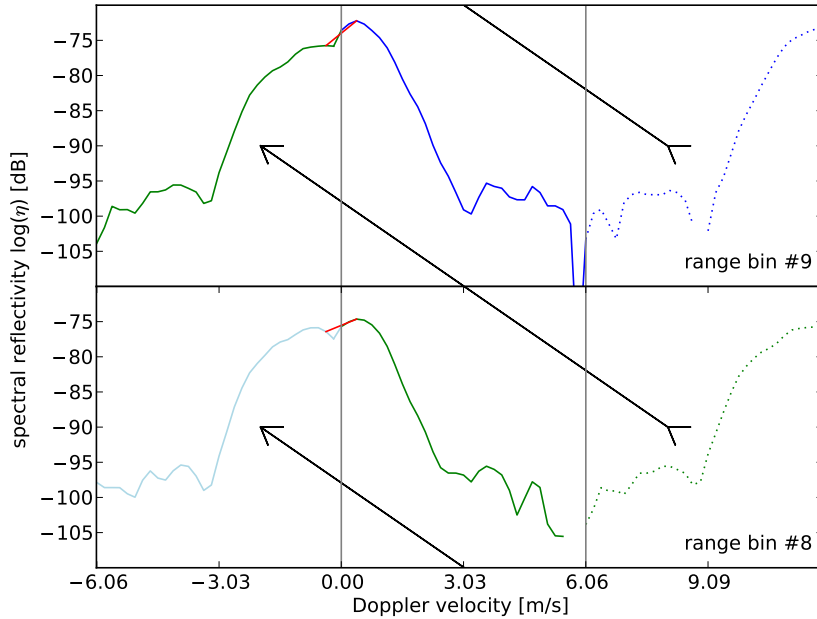


**Figure 7.1:** Dealiasing and interpolation of the MRR Doppler spectrum for an exemplary case with upward and downward moving particles. The reflectivities measured at the eighth range bin with a Doppler velocity between  $6.06$  and  $11.93 \text{ ms}^{-1}$  (green dotted) have in fact a Doppler velocity between  $-6.06$  and  $-0.189 \text{ ms}^{-1}$  and originate from the ninth height bin (green solid). The original frequency bins 0, 1, 63 around  $0 \text{ ms}^{-1}$  have been linearly interpolated (red) [after *Kneifel et al. (2011b)*].

(Fig. 7.1). Following the definition used in the MRR standard product, the mean Doppler velocity ( $W$ ) is derived as the first moment of the dealiased Doppler spectrum.

### 7.1.3 Frequency related $Z_e$ conversion based on simulations

The two radar systems operate at wavelengths of  $12.4 \text{ mm}$  (MRR) and  $8.4 \text{ mm}$  (MIRA36); thus the Rayleigh approximation (Section 4.3.1) cannot be applied to snowflakes. Scattering properties of three theoretical snow particle models 6BR, SEC, and DEN (Section 5.4) are used to investigate and quantify the differences of snowfall backscattering properties at the two radar frequencies and their dependency on particles size, SSD and SWC. The backscattering properties of the chosen particles and especially their deviations from the Rayleigh approximation are illustrated in Fig. 7.2. When the backscattering cross sections at  $35.5$  and  $24.1 \text{ GHz}$  are multiplied by  $\lambda^4$ , the size dependency for all particles within the Rayleigh approximation will follow the diagonal (see Eq. 4.27). As expected, the particles fit very well to the Rayleigh approximation up to particle sizes of  $\sim 2.5 \text{ mm}$ . For further increasing particle sizes, the backscattering behavior approaches the Mie regime where particularly DEN show deviations of up to one order of magnitude. Due to the higher frequency, the backscattering values at  $35.5 \text{ GHz}$  reach the first Mie anomalies at larger sizes; hence the  $35.5 \text{ GHz}$  backscattered signal becomes lower than  $24.1 \text{ GHz}$  signal.

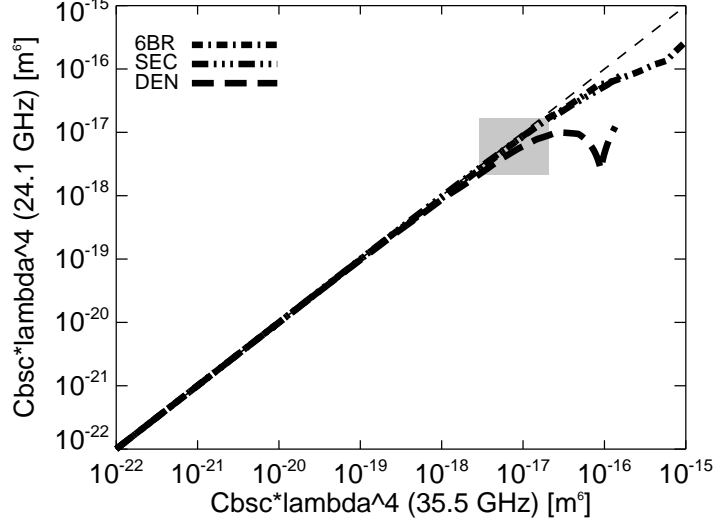


**Figure 7.2:** Backscattering cross section  $C_{b,sc}$  [ $\text{m}^{-2}$ ] multiplied with 24.1/35.5 GHz wavelength  $\lambda$  to the power of four [ $\text{m}^{-6}$ ] for snow particle types: (dashed–dotted) 6BR, (dashed–triple–dotted) SEC, and (long dashed) DEN. The thin dashed line denotes the direct line. The corresponding particles have maximum geometrical sizes between  $100\ \mu\text{m}$  and  $10\ \text{mm}$ . The grey shaded area marks values for associated particle size of  $2.5\ \text{mm}$ . [from *Kneifel et al. (2011b)*].

Following the discussion about typical SSD parameters (Section 3.1), an exponential SSD with a  $N_0$  range between  $10^6$  and  $10^8$  has been assumed. With the minimum/maximum size limitations of the Liu database (Section 5.4.1) Eq. 4.42 for calculating  $Z_e$  changes to

$$Z_e = 10^{18} \frac{\lambda^4}{\pi^5 |K|^2} \int_{D_{min}}^{D_{max}} \sigma_b(D) N(D) dD. \quad (7.2)$$

$|K|^2$  is again set to 0.92 in order to be consistent with the assumptions made in the MIRA36 and MRR data processing. The results of the simulations for different sets of SWC,  $N_0$  and particle habits in terms of  $Z_e$  are shown in Fig. 7.3. As expected,  $Z_e$  values for 24.1 and 35.5 GHz deviate most for SSD with a high number of large particles (i.e. the smallest  $N_0$ ). The largest differences of up to 7 dB are again obtained for DEN. These results imply not only that  $Z_e$  differ considerably for the two frequencies, but also that a simple relation between  $Z_e$  at 35.5 GHz and  $Z_e$  at 24.1 GHz can be obtained. Fig. 7.3 demonstrates that distinct power law relations can be derived for every particle shape and  $N_0$  combination. Knowing the real SSD and predominant particle shape (e.g. from optical particle probes), the appropriate coefficients can then be applied to the measured MRR  $Z_e$ . However, even with 2DVD data it is difficult to classify the true particle type, since natural snowfall usually consists of a mixture of habits (Section 3.2).

Taking the observed variability into account, an average relation by combining all different snowfall realizations seems to be the most reasonable assumption, if accepting the fact that individual snowfall events can deviate from the average relation. Based on the simulations, the following power law relation (transferred into a linear relation when using dBz units) has been derived to convert the MRR  $Z_e$  into equivalent 35.5 GHz  $Z_e$

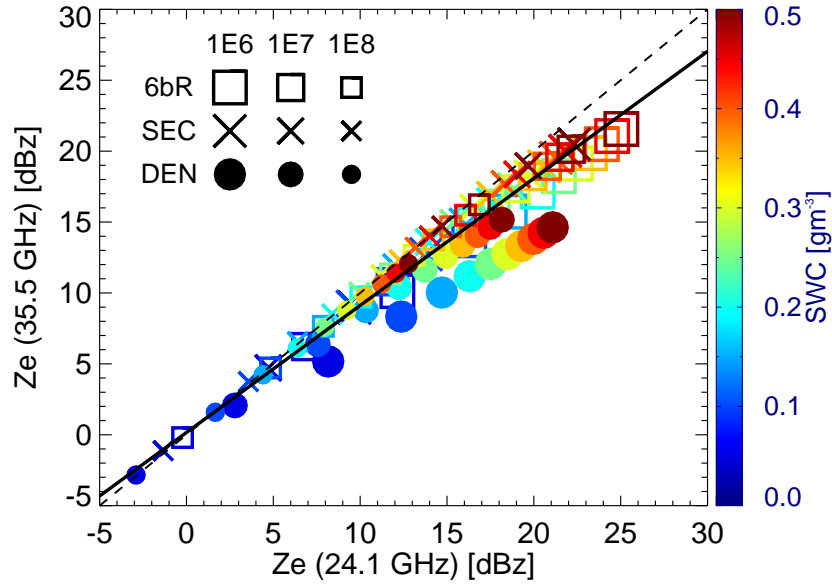


**Figure 7.3:**  $Z_e$  in dBz simulated for 35.5 and 24.1 GHz. The symbols denote the different snow particle types: (squares) 6BR, (crosses) SEC, and (filled circles) DEN. The symbol size indicates the related  $N_0$  value [ $\text{m}^{-4}$ ] of the underlying snow size distribution ranging from (smallest)  $10^8$ , (middle)  $10^7$  to (largest)  $10^6$ . The color coding shows the snow water content (SWC,  $\text{gm}^{-3}$ ) of the related simulation. The dashed line denotes the direct line; the solid line results from a linear regression of combining all snowfall realizations [from *Kneifel et al. (2011b)*].

$$10 \log(Z_{e,35.5\text{GHz}}) = \alpha 10 \log(Z_{e,24.1\text{GHz}}) + \beta. \quad (7.3)$$

The derived coefficients for Eq. 7.3 are  $\alpha = 0.896$  and  $\beta = 0.161$ . Those can then be applied e.g. to standard  $Z_e$ -SR relations to derive surface SR from MRR observations.

#### 7.1.4 Bias correction and noise level estimation

In order to test the calibration of the MRR and the MIRA36, their estimates of  $Z$  for liquid precipitation at 600 m height (lower range gates are potentially affected by near-field effects) were compared with  $Z$  estimated by a PARSIVEL optical disdrometer (*Löffler-Mang and Joss, 2000*). All three instruments derive  $Z$  from the estimated DSD using the sixth moment of the DSD (Eq. 4.41). The dataset from summer 2008 includes 54 rainy days with a total rain amount of 290 mm and a melting layer height above 800 m from the ground. To exclude impacts both of shallow precipitation and of attenuation effects, the comparison was limited to the reflectivity interval 5–20 dBz. For this interval, a stable mean offset of -5 dBz for the MRR and +2.5 dBz for the MIRA36 was found, which are considered as calibration offsets of the used instruments during TOSCA and are corrected accordingly.

Besides calibration biases, electronic and thermal noise always cause an artificial background input power at any radar receiver even under clear-sky conditions. This noise is removed dynamically by the MRR (*METEK, 2010*). Even with a perfect estimate of the

**Table 7.1:** Noise thresholds (NTH) using 99% quantile of the MRR clear-sky noise: Thresholds are derived from the 35.5 GHz equivalent  $Z_e$  values. The heights in km indicate the distance from the radar.

Height [km]	0.5	0.6	0.7	0.8	0.9	1.0	1.1	1.2	1.3	1.4	1.5
NTH [dBz]	-2.1	-1.7	-1.6	-1.4	-1.3	-1.0	-1.1	-0.9	-1.0	-0.8	-0.9
Height [km]	1.6	1.7	1.8	1.9	2.0	2.1	2.2	2.3	2.4	2.5	
NTH [dBz]	-0.6	-0.7	-0.4	-0.6	-0.4	-0.2	0.0	-0.1	0.4	1.0	

mean noise level, the remaining  $\eta$  would fluctuate around zero. Integrating the negative and positive  $\eta$  over the entire frequency range according to (Eq. 7.1) should result in  $Z_e$  values around zero (linear scale). Deviations from the white noise assumption and uncertainties of the noise level estimate, however, result in remaining non-zero  $Z_e$ .

As a first guess assumption, the 99% quantile of the resulting  $Z_e$  distribution is assumed as a reasonable threshold to separate physical signal from noise. The noise thresholds used in this study are shown in Table 7.1 as  $Z_e$ . Using the 99.5(99.9)% quantile instead raises the threshold merely by 0.2 (0.6) dBz (35.5 GHz equivalent). The noise thresholds were obtained from an analysis of 17 clear-sky periods identified by ceilometer and cloud radar observations during the TOSCA period. The detectability is highest close to the ground with -2 dBz (35.5 GHz equivalent) at 500 m, but is decreasing with height to 3 dBz at 3000 m. Due to variations in the electronic components of MRR instruments, the detectability profile is unique for each MRR. Since  $\eta$  is stored logarithmically in the standard MRR product, an additional systematic positive bias in the derived  $Z_e$  is generated due to the omission of negative  $\eta$  for clear-sky cases. However, it has been found (*Maahn, 2010, 25 pp*) that this correction improves the detectability by merely 0.2-0.3 dBz and thus, this step is omitted in this study.

During the six months period, no significant temporal noise drift was observed. The  $Z_e$  probability density distribution is exemplarily presented for the 600 m height level in Fig. 7.4. In general, the width of the noise distribution depends on the total number of spectra and the averaging time used to calculate  $Z_e$ . Here, an averaging time of 60 seconds was chosen; larger averaging times result in an even lower detectability threshold but at a loss of resolved temporal variability.

### 7.1.5 Comparison of $Z_e$ and mean vertical fall velocities

In this part Eq. 7.3 is applied to real MRR data that were processed in the way described in Section 7.1.1. The applicability of the clear-sky noise level estimate and  $Z_e$  conversion method is tested by comparing collocated measurements from the MRR and MIRA36. The whole six months TOSCA period, which contains — after data quality checks — 59 days with snowfall has been analyzed. It is assumed that all precipitation particles are frozen, since the 2m-temperatures during the observation time were always below -5 °C.

The MIRA36 data have a range resolution of 30 m and a temporal resolution of 15 s, while the MRR data have a range/temporal resolution of 100 m and 60 s, respectively. To reduce differences that can arise from the different temporal/vertical resolution and different beam widths of the two instruments (Tab. 2.2), the MIRA36 data have been averaged onto

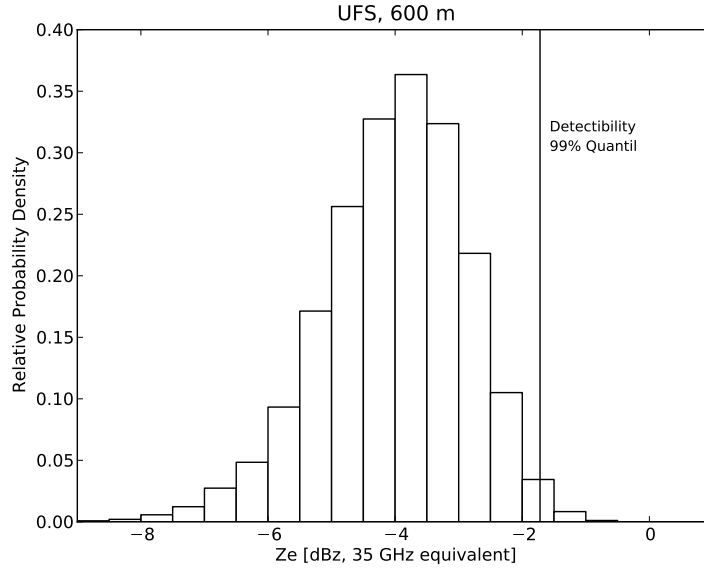


**Figure 7.4:** Histogram of MRR clear-sky noise at 600 m height based on 17 clear-sky days derived from the temporal averaged (60 s) Doppler spectra in dBz (converted into 35.5 GHz equivalent  $Z_e$ ). The vertical lines denote the noise threshold in dBz (35.5 GHz equivalent) defined as the 99% quantile. [from *Kneifel et al. (2011b)*].

the MRR spatio-temporal grid. It is mentioned by the manufacturer of the MRR that the lowest 2–3 radar range gates are particularly influenced by instrument errors and near field effects. It was found that data at heights above 500 m and below 2500 m are sufficiently free of disturbing effects and all data outside this interval were discarded. All comparisons are presented as functions of MIRA36- $Z_e$  and height above ground. The  $Z_e$  values derived directly from the Doppler spectra are first compared without any frequency correction as mean differences ( $dZ_e$ ) between MRR and MIRA36 (Fig.7.5(a)). The comparison reveals two main patterns:

The values of  $Z_e$  larger than the clear-sky noise level show a mean  $dZ_e$  of 0–2 dB that is greatest at the lower height levels (600–1300 m). If the  $Z_e$  values fall below 5 dBz the  $dZ_e$  values increase significantly with a slight dependence on height. This behaviour is a result of the quiet different sensitivity ranges of the two radars. While MIRA36 measures reflectivity factors down to -44 dBz, the MRR reaches its noise level around 0 dBz. Reflectivity factors below that level will thus result in increasing  $dZ_e$ . This explanation is corroborated by the fact that the 99% quantile (Tab. 7.1) as a clear-sky noise level (black dashed line) fits generally well with the region of strongly increasing  $dZ_e$  values; therefore, choosing the lower 99% quantile seems to be a reasonable assumption.

For values of  $Z_e$  above 12 dBz, a slight increase of  $dZ_e$  values in the range of 1–2 dBz is found. These larger  $dZ_e$  values agree well with the predicted  $dZ_e$  increase in the simulations (Section 7.1.3) caused by a higher number of large snow particles. If the simulations represent the backscattering properties of natural snowfall, this enhancement should disappear when applying (Eq. 7.3). Fig.7.5(b) shows the resulting  $dZ_e$  after converting the MRR  $Z_e$  into 35.5 GHz equivalent values. The former  $dZ_e$  increase at higher  $Z_e$  values disappears and the



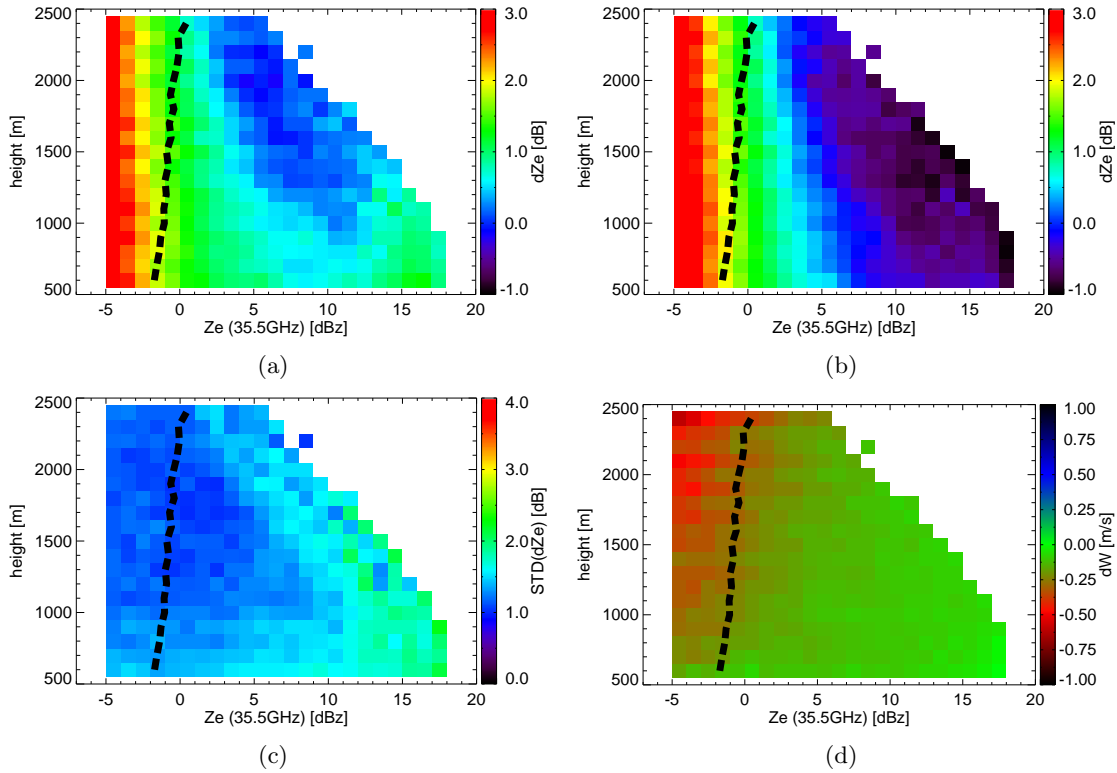


**Figure 7.5:** Comparison of MRR and MIRA36 observations during TOSCA for a six-month winter time period in 2008/2009. (a) Mean  $Z_e$  differences of MRR (24.1 GHz) – MIRA36 (35.5 GHz) ( $dZ_e$ ) in dB as a function of height [m AGL] and MIRA36– $Z_e$  value. The dashed black line denotes the MRR noise level derived from clear-sky days (converted into 35.5 GHz equivalent values). (b) same as (a) but MRR  $Z_e$  are converted into 35.5 GHz equivalent values. (c) Standard deviation of  $dZ_e$  in (b). (d) Mean difference of  $W$  between MRR and MIRA36 in  $\text{ms}^{-1}$ . Each pixel in (a)–(d) contains a minimum number of 200 observations [from *Kneifel et al. (2011b)*].

$dZ_e$  reduces to  $< 1$  dB for the  $Z_e$  region larger than 2 dBz. Close to the noise level (below 3 dBz) the  $dZ_e$  are found somewhat higher around 2 dB. This effect cannot be fully explained so far, however, it seems that the MRR noise correction algorithm underestimates the noise level which particularly affects the lower  $Z_e$  values.

In addition to the mean  $dZ_e$  values, Fig.7.5(c) shows the variability of  $dZ_e$  for single profiles expressed as the standard deviation of  $dZ_e$ . The values increase almost continuously from 1.0 to 1.5 dB at 0–8 dBz up to 2.5 dB at 15 dBz. The increasing variability of  $dZ_e$  is consistent with the simulation results: The natural snow particle habit diversity has an increasing impact on  $dZ_e$  at larger  $Z_e$  values, i.e. larger snow particle sizes. It is thus important to take this variability into account when using the  $Z_e$  values for  $Z_e$ –SR relations.

The mean velocity differences ( $dW$ ) of the two radars are found to be between 0 and  $-0.3 \text{ ms}^{-1}$  (Fig.7.5(d)). Larger differences are found at larger heights and lower  $Z_e$ , where noise becomes a dominant part of the signal. Below the MRR noise level the  $dW$  values are probably noise artefacts. The standard deviations of  $dW$  (not shown) are below  $0.5 \text{ ms}^{-1}$  for the entire  $Z_e$  and height range, indicating a high agreement of the two velocity measurements

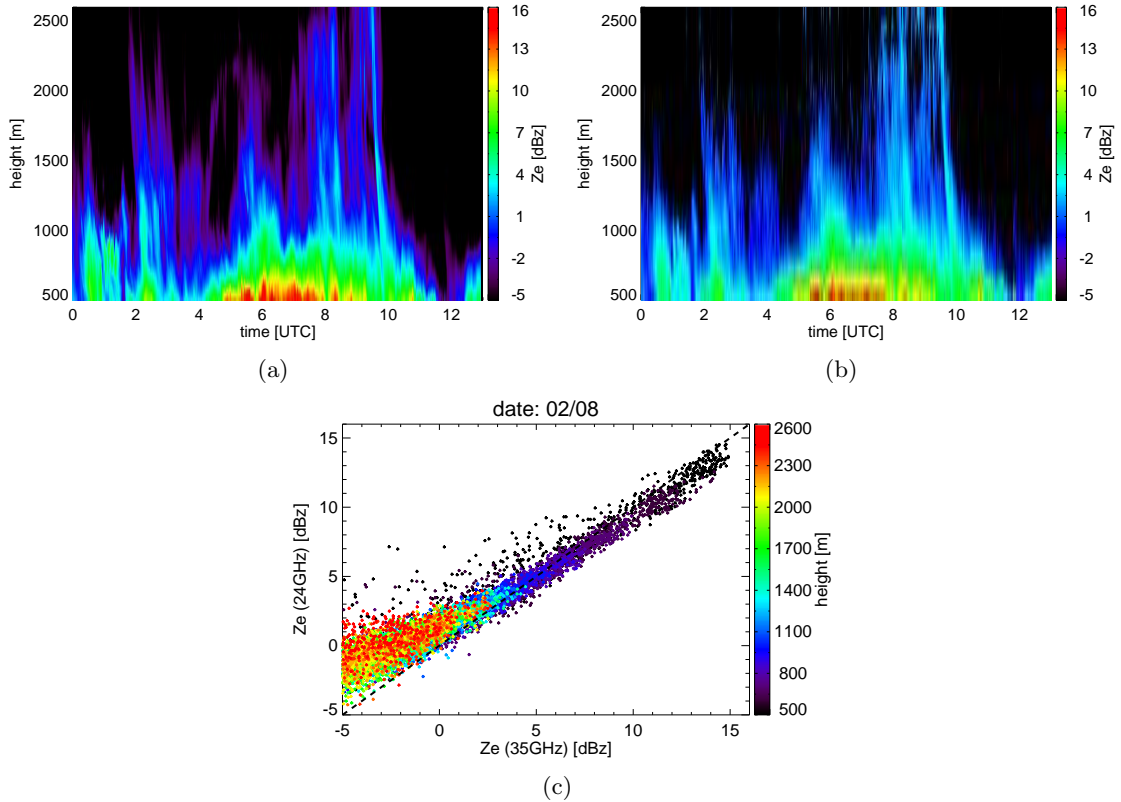


**Figure 7.6:** Time–height cross sections of  $Z_e$  [dBz] for (a) MIRA36 and (b) MRR on 08. Feb. 2009.  $Z_e$  values from both radar systems and for all heights (color code) are plotted as scatter plot in (c); direct line is dashed. All MRR values have been converted into 35.5 GHz equivalent  $Z_e$  according to Eq. 7.3. Note, that the MIRA36 reflectivity values have been reduced to the MRR  $Z_e$ –range [from *Kneifel et al. (2011b)*].

even for single profiles. An example for a typical snowfall event apparent in both the MRR and the MIRA36 data is presented in Fig. 7.6. The time–height cross sections of the MIRA36 (Fig. 7.6(a)) and the frequency corrected MRR (Fig. 7.6(b)) observations reveal a very high structural agreement<sup>2</sup>. The MRR reveals even small scale structures up to its maximum height. For better comparison of the  $Z_e$  values, they are displayed also as a scatter plot in Fig. 7.6(c). The larger values between 5 and 15 dBz agree very well as expected from the former statistical analysis (Fig. 7.5). At the lowest  $Z_e$  values the MRR  $Z_e$  reach the noise level and remain between 0 and -4 dBz.

### 7.1.6 Snowfall rates and total snow accumulation

The MRR–MIRA36 comparison confirmed the reliability of both the clear–sky noise level estimate and the applicability of the  $Z_e$  conversion (Eq. 7.3). The effects of the limitations of the MRR on the derived SR and the amount of snow accumulated over a certain time will be evaluated in this section. To this goal, three recently published  $Z_e$ –SR relations for 35 GHz

<sup>2</sup>Note that for better comparison the MIRA36  $Z_e$  values have been limited to the  $Z_e$  range, which can be captured by the MRR.

**Table 7.2:** Prefactor  $c$  and exponent  $d$  (Eq. 7.4) for published  $Z_e$ -SR relations for dry snowfall and 35 GHz (see text for details).

Refernce	$c$	$d$
<i>Kulie and Bennartz</i> (2009), LR3	24.04	1.51
<i>Kulie and Bennartz</i> (2009), HA	313.29	1.85
<i>Kulie and Bennartz</i> (2009), SS	19.66	1.74
<i>Matrosov</i> (2007)	56.00	1.20
<i>Noh et al.</i> (2006)	88.97	1.04

have been selected. Usually,  $Z_e$ -SR relations are formulated as power laws in the form

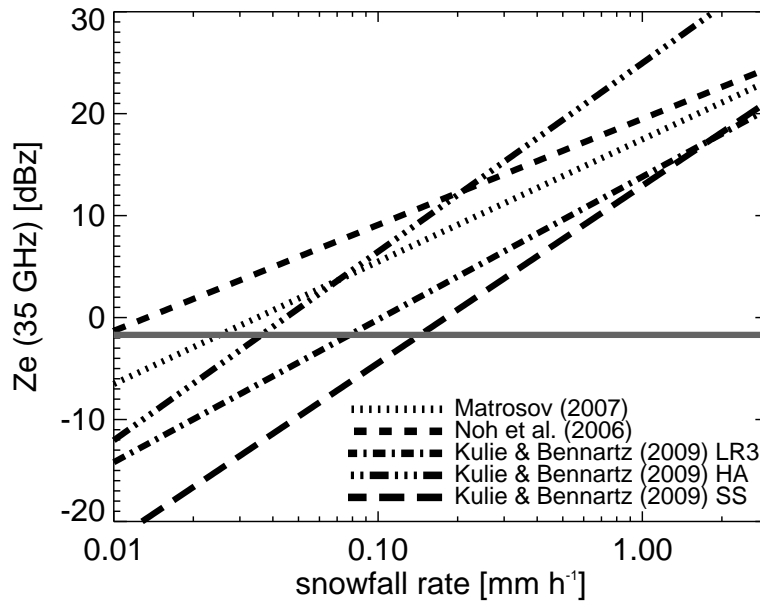
$$Z_e = cSR^d, \quad (7.4)$$

with  $Z_e$  in  $\text{mm}^6\text{m}^{-3}$ , the liquid equivalent SR in  $\text{mmh}^{-1}$ , and  $c$ ,  $d$  coefficients which are summarized in Tab. 7.2 for several relations.

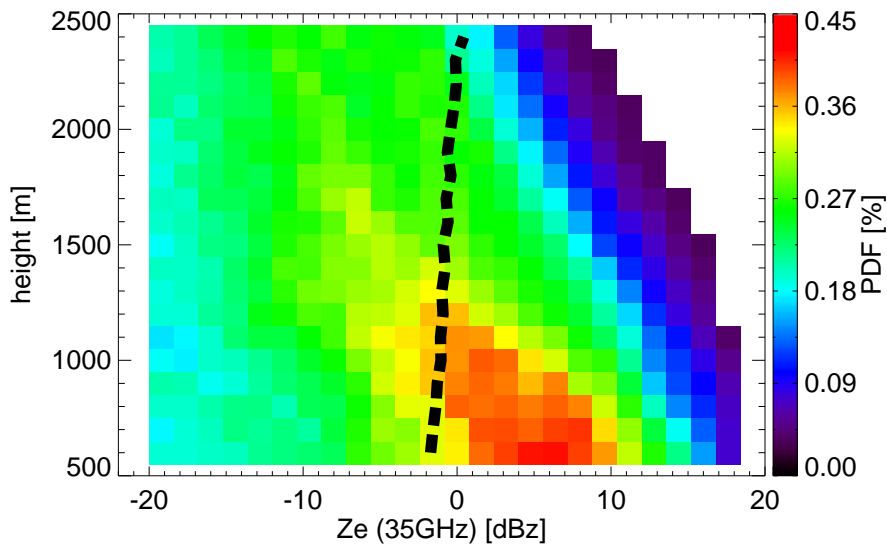
The  $Z_e$ -SR relations are extremely sensitive to the chosen snow particle habit and SSD, which can be seen in the large variability of the  $c$  and  $d$  coefficients. The selected relations in Tab. 7.2 cover the variability of a large set of different particle habits and SSD realizations: *Kulie and Bennartz* (2009) compared in their studies 22 different snow particle habits using the SSD parameterization by *Field et al.* (2005). They identify the  $Z_e$ -SR relation for the three-bullet rosette (LR3) as an average of the different relations. Furthermore, they select the aggregate ice particle (HA) and the low-density spherical snow particle (SS) to represent the variability of the different relations. *Matrosov* (2007) found for horizontally aligned soft ellipsoids with an aspect ratio of 0.6 that their scattering properties are representative for natural snow aggregates. *Noh et al.* (2006) derive their  $Z_e$ -SR relation with an average of SEC and DEN that are also used in this study (Section 5.4.1).

Fig. 7.7 shows the resulting SR, which can differ up to one order of magnitude depending on the chosen relation. Taking into account the MRR noise level (at 600 m height), it can be found that values of SR below  $0.01$ – $0.15 \text{ mmh}^{-1}$  are likely to be missed by the MRR. The retrieval quality of snow accumulation by the MRR can only be estimated if the probability density function (PDF) of the SR (or  $Z_e$  values) is known. From the TOSCA dataset the  $Z_e$ -PDF using the MIRA36 observations has been derived for a six months time period (Fig. 7.8). It should be noted that the PDF might only be valid for this particular location, since clouds and precipitation processes can significantly be influenced by the surrounding orography. However, a comparison with recently published  $Z_e$ /SR distributions for northern mid-latitudes based on CloudSat observations (*Kulie and Bennartz*, 2009) reveals that the UFS data show a more general behavior and are not so much dependent on the specific conditions of the UFS site.

The probability of large  $Z_e$  values decreases with increasing height and is largest close to the ground, as expected. In the lowest 1500 m the  $Z_e$  values range mostly between  $-10$  and  $10 \text{ dBz}$ . At 600 m height level (used for estimating the surface SR) about 50% of the MIRA36  $Z_e$  values are larger than the MRR noise level. When a minimum  $Z_e$  threshold of  $-10 \text{ dBz}$  is assumed for precipitating clouds — which would exclude SR up to a maximum of about  $0.05 \text{ mmh}^{-1}$  according to Fig. 7.7 — the MRR would still detect about 70% of the precipitation cases.



**Figure 7.7:**  $Z_e$  [dBz] at 35 GHz, as a function of SR [ $\text{mmh}^{-1}$ ] for five different  $Z_e$ -SR relations from literature (see also details in the text). The grey solid line denotes the estimated clear-sky noise threshold of the MRR at 600 m height (converted to 35 GHz equivalent values) [from *Kneifel et al. (2011b)*].



**Figure 7.8:** 2D probability density function (percentage color coded, total number of measurements is 749,686 taking into account all bins) of MIRA36  $Z_e$  [dBz] depending on  $Z_e$  and height above ground level. Each pixel contains a minimum number of 200 observations. The dashed black line denotes the clear-sky noise level of the MRR (converted into 35 GHz equivalent  $Z_e$ ) [from *Kneifel et al. (2011b)*].

Fig. 7.9 illustrates how the different SR contribute to the snow accumulation. The  $Z_e$ -SR relation from *Matrosov (2007)* has been exemplarily applied to the six months MIRA36 data

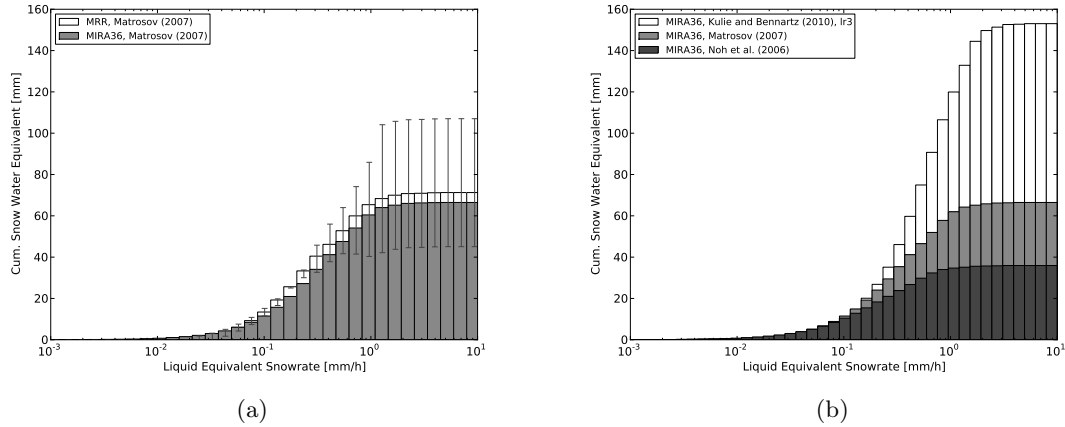


**Figure 7.9:** (a) The *Matrosov* (2007)  $Z_e$ -SR relation has exemplarily been applied to the MIRA36 dataset (light grey) and to the simultaneous MRR measurements (white bars) at 600 m height. The MRR values have been converted into 35 GHz equivalent values. The cumulative snow water equivalent [mm] is shown as a function of SR ( $\text{mmh}^{-1}$ ). The error bars indicate the uncertainty in the estimated cumulative snow water equivalent due to the standard deviation of  $dZ_e$  at 600 m height (see Fig. 7.5(c)). (b) Similar to (a) however, three different  $Z_e$ -SR relations are applied only to the MIRA36 data at 600 m height [from *Kneifel et al.* (2011b)].

set and to the converted MRR, since it is close to the mean of the  $Z_e$ -SR relations shown in Fig. 7.7, particularly for larger SR. It should be noted that the actual snow accumulation for the considered time period is probably higher, since 46 % of the data have been filtered out in quality checks (mainly due to snow/ice covered radar antennas). The total snow accumulation (liquid equivalent) estimated from the MIRA36 (MRR) observations is 66 (71) mm. The 7 % higher MRR snow accumulation estimate can be related to the slight  $Z_e$  overestimation of the MRR at  $Z_e$  between 0 and 5 dBz (see also Fig 7.5(b) and discussion). When the standard deviation of the  $dZ_e$  is applied as a rough uncertainty estimate for the MRR observations, the obtained values in terms of total snow accumulation vary between 45 and 107 mm (63 % and 151 % of the mean). For comparison, the estimated precipitation rate based on the standard MRR retrieval for liquid rain would result in a total amount of precipitation of 164 mm, which illustrates the necessity to modify the retrieval for snowfall observations.

Obviously, the smaller SR ignored by the MRR do not significantly contribute to the snow accumulation for this period because the largest contribution stems from SR between 0.1 and 0.8  $\text{mmh}^{-1}$  which corresponds to a  $Z_e$  range between 5 and 16 dBz. These findings are in general agreement with results based on CloudSat observations at 1300 m height level where SR between 0.1 and 1.0  $\text{mmh}^{-1}$  have been found to contribute most to the average snow amount (*Kulie and Bennartz, 2009*).

Three hourly manual snow accumulation observations are available at the nearby summit of mountain Zugspitze by the DWD. These observations are probably affected by wind drift and orographic effects. Nevertheless, their measured value of 65 mm for the six-months period (observation periods restricted to the considered radar time periods) confirms that the order of magnitude of the derived radar estimates is reasonable. Besides the uncertainty introduced by different radar sensitivities, however, one of the largest sources of uncertainty remains the

uncertainty of the  $Z_e$ -SR relations. Fig. 7.9(b) illustrates this variability by showing the results of three exemplary  $Z_e$ -SR relations applied to the  $Z_e$ -PDF of the MIRA36 at 600 m height: the estimated total snow accumulation varies due to the different relations between 36 and 153 mm snow water equivalent. This variability is about a factor two larger than the uncertainty of the two different radar systems.

## 7.2 Single- and dual- frequency approach for snowfall

In the first part of this chapter, two single-frequency radars have been compared in order to explore the practical capabilities of a “low-end” radar for snowfall observations which is usually used for rainfall. Besides the technical differences of various radar systems, there is a principal challenge for deriving physical quantities from the radar observables like  $Z_e$ : Similar to the  $T_B$  for passive MWR (Chapter 6),  $Z_e$  depends on several unknown parameters (Eq. 4.42) such as the scattering properties of the single particles, the SSD and the mass-size relation. Usually, ground-based observations of SR or accumulation are used as additional constraints in order to determine the best average fitting parameter set. As a result of the varying assumptions on input parameters the derived single-frequency relations contain a high degree of uncertainty (e.g. *Kulie and Bennartz, 2009; Kulie et al., 2010*). An example of the expected uncertainty range has been given in Fig. 7.7: Assuming for example that a 35.5 GHz cloud radar (like MIRA36) measures a  $Z_e$  value of 1 dBz, the derived SR span from 0.02 to 0.2 mmh<sup>-1</sup> which is a factor of ten difference.

The most common approach to overcome this ambiguity is to extent from single-frequency observations towards multi-frequency measurements — similar to the passive microwave approaches (Chapter 6). The basis for potential improvements due to multi-frequency use is based on the fact that various input parameters change the radiative properties (i.e. for example the multi-frequent  $Z_e$  values) differently at different frequencies.

In the following sections the well established dual-wavelength approach will be discussed and the method will be tested with non-spherical snow particle models. Subsequently, the dual-frequency approach will be extended towards a third frequency that has potential to separate different particle models and to further constrain snowfall radar retrievals. The dual- and triple-frequency approach are illustrated at the frequencies 13.4, 36.5 and 89 GHz (i.e. wavelength of 2.2 cm, 8.2 mm and 3.4 mm that corresponds to K<sub>a</sub>-, K<sub>u</sub>- and W-bands, respectively). Longer wavelength radar (e.g., X-, S-, or C-band) could provide advantages over the longest wavelength (K<sub>u</sub>-band) used in this study, as non-Rayleigh scattering effects will not be an issue at these wavelengths for typical snowflake sizes. Such wavelengths have been used in multi-frequency radar studies e.g. for the retrieval of liquid and ice water content by *Gaussiat et al. (2003)*. However, the frequency selection in this study is primarily motivated by its similarity to several ground-based cloud radar systems (e.g., at the Atmospheric Radiation Measurement (ARM) Climate Research Facility sites) that operate at similar frequencies and are currently upgraded to multi-frequency systems. In recent years, mobile integrated triple-frequency radar systems (*McLinden, 2010*) have also been developed and are available for field campaigns to provide simultaneous measurements at K<sub>u</sub>-, K<sub>a</sub>- and W-bands. Finally, the upcoming Global Precipitation Measurement (GPM) mission (including active 13.4 and 35.6 GHz observations) combined with 94 GHz measurements from platforms such as CloudSat will provide additional triple-frequency data of snowfall.

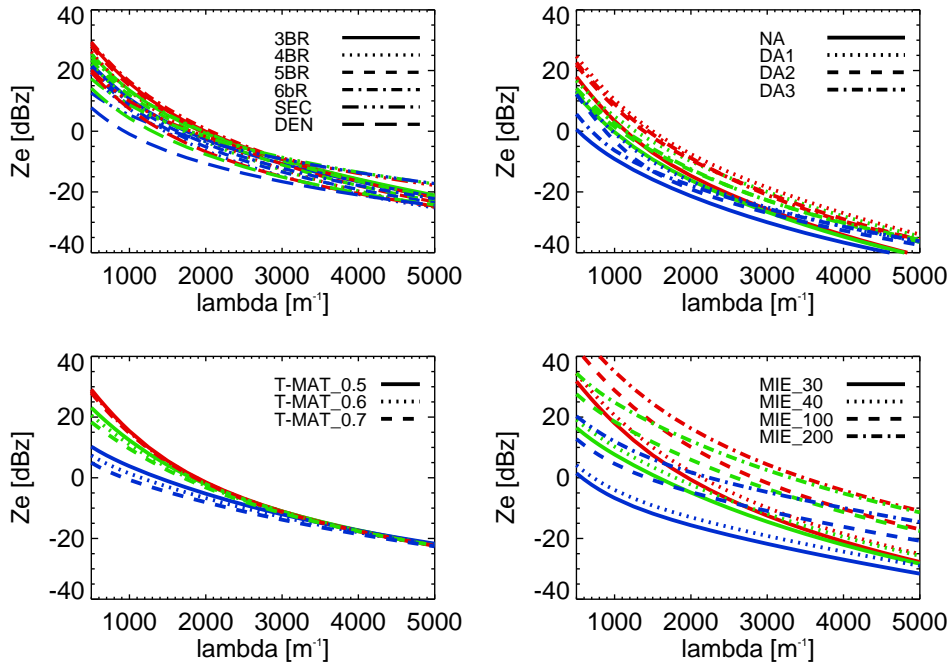


**Figure 7.10:**  $Z_e$  [dBz] as a function of the slope parameter  $\Lambda$  [ $m^{-1}$ ] for different snow particle models: LIU (upper left), AGG (upper right), T-MAT (lower left) and MIE (lower right). Particle types are the same as Fig. 3.5 except MIE particles are shown for different snow densities: (solid) 30, (dotted) 40, (dashed) 100 and (dashed-dotted) 200  $kgm^{-3}$ . T-MAT particles have different aspect ratios: (solid) 0.5, (dotted) 0.6, and (dashed) 0.7. The intercept parameter for all simulations is  $N_0 = 10^6 m^{-4}$ . The color indicates the radar frequency: (red) 13.4 GHz, (green) 36.5 GHz, and (blue) 89 GHz [after *Kneifel et al. (2011a)*].

### Dual-frequency approach

The classical dual-frequency approach is based on the fact that  $Z_e$  is a monotonic function of the SSD parameter  $\Lambda$  (Eq. 3.1) and that these functions are different for different frequencies (*Matrosov, 1992*). Fig. 7.10 illustrates the obtained  $Z_e$  range for the three frequencies and the different particle models using exemplarily an intercept parameter  $N_0 = 10^6 m^{-4}$  (increasing/decreasing  $N_0$  by a factor of ten increases/decreases  $Z_e$  by the same factor). As expected, the  $Z_e$  values increase with decreasing  $\Lambda$  and frequency for all models. However, the slope and the absolute range of the different habits are quite different especially comparing MIE and the other models. These different dependencies of  $Z_e$  on frequency and  $\Lambda$  imply that a combination of two  $Z_e$  measurements at different frequencies can be used to derive  $\Lambda$ . Note that instead of  $\Lambda$  the median volume diameter  $D_0$  has often been used to describe the SSD.  $D_0$  is defined as the characteristic size that partitions the SSD into two equal volume parts. In order to make our results more comparable to former studies, the relation between  $\Lambda$  and  $D_0$  for the different particle models is shown in Fig. 7.11. Depending on the maximum particle size included in the SSD,  $D_0$  varies from 0.5 to 6.2 mm (10 mm maximum size) and 0.5 to 3.8 mm (5 mm maximum size). The deviations between the different habits are largest for the lowest  $\Lambda$  values with up to 2 mm.

Usually, the dual wavelength ratio (DWR) is defined for two wavelengths  $\lambda_1, \lambda_2$  as

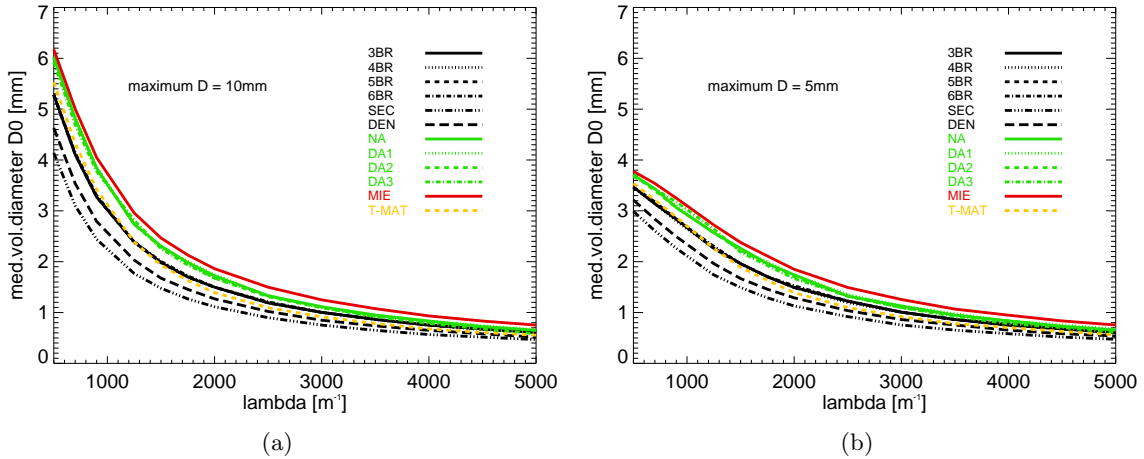


**Figure 7.11:** Median volume diameter  $D_0$  [mm] as function of the slope parameter  $\Lambda$  [ $\text{m}^{-1}$ ] for SSD with maximum particle sizes of (a) 10 mm and (b) 5 mm. Particle model description same as Fig. 3.5. Note that the different bullet rosette habits almost completely overlap [from (Kneifel et al., 2011a)].

$$DWR_{\lambda_1, \lambda_2} = 10 \log\left(\frac{Z_{e, \lambda_1}}{Z_{e, \lambda_2}}\right) \quad (7.5)$$

or simply as the difference of the  $Z_e$  values in units of dBz. For simplicity, we avoid using the actual radar wavelength as index and refer to DWR with the corresponding radar band in the following discussion. Note that considering the definition of  $Z_e$  (Eq. 4.42) and inserting the exponential SSD, the DWR is found to be independent of  $N_0$ .

Many studies that used DWR to derive snowfall quantities approximated the backscattering properties of snow with soft spheres (Matrosov, 1992; Liao et al., 2005, 2008) or spheroids (Matrosov, 1998; Matrosov et al., 2005a). Matrosov (1992) and Matrosov (1998) first showed that the relation between DWR and  $D_0$  is almost independent of the assumed snow density. This lack of sensitivity to snow density allows  $D_0$  to be derived directly from the measured DWR. The critical question is, however, how strongly the DWR– $D_0$  relation changes, if non-spherical snow particle models are used. In an attempt to take non-sphericity of snow particles into account, Matrosov (1998) used spheroids with an aspect ratio of 0.6 to represent snow scattering at 34.6 and 94 GHz. Based on polarization observations, he further assumed that those spheroids are horizontally oriented with a standard deviation of  $9^\circ$  from the perfect horizontal orientation. This spheroid model was then used to calculate the DWR at 9.6 and 94 GHz (Matrosov et al., 2005a). The study revealed that the DWR is sensitive to the chosen aspect ratio, which can be interpreted as a kind of snow particle shape sensitivity of DWR.

In addition to the soft sphere approach (MIE) and the spheroid method (T-MAT), the DWR have been derived for the particle shape models that are based on DDA calculations (Section 5.4) (LIU and AGG)<sup>3</sup>. The  $DWR_{K_u, K_a}$  in Fig. 7.12 is shown as a function of the slope parameter  $\Lambda$ . The results are consistent with the former studies that show,  $DWR_{K_u, K_a}$  for

<sup>3</sup>Compared to Kneifel et al. (2011a) an updated version of the LIU database and an improved Mie-code have been used within this study.



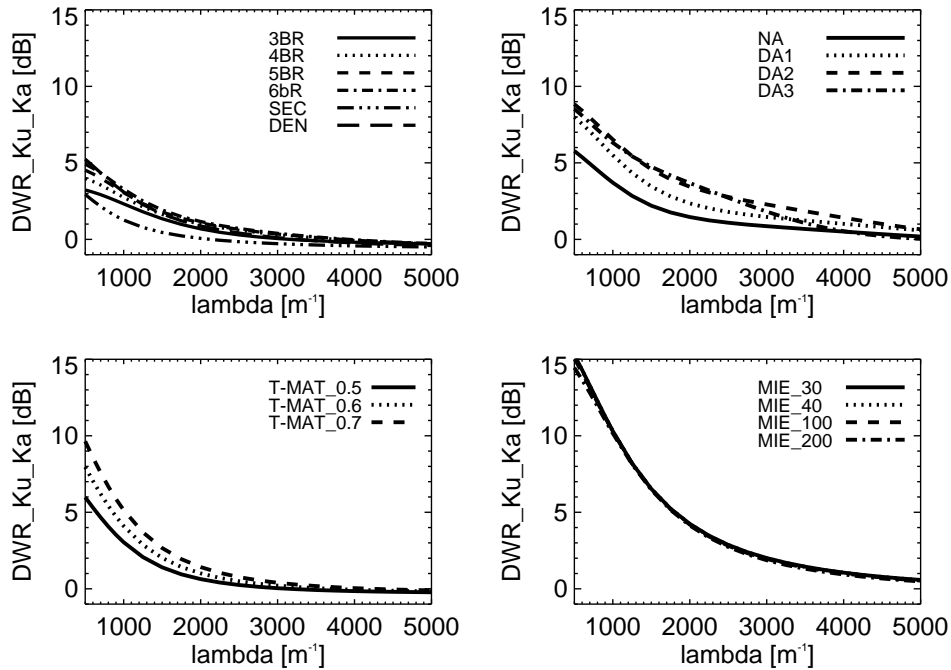


**Figure 7.12:** Dual wavelength ratio (DWR) in dB for 13.4 GHz ( $K_u$ -band) and 36.5 GHz ( $K_a$ -band) as a function of the slope parameter  $\Lambda$  [ $\text{m}^{-1}$ ]. Note that DWR is independent of the intercept parameter  $N_0$ . Particle model descriptions are the same as Fig. 7.10 [after *Kneifel et al. (2011a)*].

MIE is almost independent of the chosen snow density. However, for other particle models like AGG or LIU, DWR is found to be considerably shape-dependent: In general, the  $\text{DWR}_{K_u, K_a}$  values for the different particle habits increase towards lower  $\Lambda$  values (larger particle sizes) and range for  $\Lambda = 600 \text{ m}^{-1}$  from 3–15 dB. However, similarities between particle habits can be also found. For instance,  $\text{DWR}_{K_u, K_a}$  for T-MAT are similar to the AGG particles that are comprised of dendrites (DA1–3). In contrast to the LIU, AGG and T-MAT snow models that show similarities in absolute values and dependence of  $\text{DWR}_{K_u, K_a}$  on  $\Lambda$ , the  $\text{DWR}_{K_u, K_a}$  values are found to be up to 10 dBz higher for MIE soft spherical models — especially at the lower  $\Lambda$  range.

The  $\text{DWR}_{K_a, W}$  values for two other common cloud radar frequencies (36.5 and 89 GHz<sup>4</sup>) are shown in a similar way in Fig. 7.13. For these frequencies, LIU and most of the AGG particles show an almost constant or even decreasing  $\text{DWR}_{K_a, W}$  towards lower  $\Lambda$  values. In contrast,  $\text{DWR}_{K_a, W}$  values for the MIE and T-MAT particles increase. This is mainly a result of the different complex backscattering behavior at 36.5 and 89 GHz and the different mass-size relations. As a result of implementing the  $Z_e$  at 89 GHz<sup>5</sup>, the shape dependence of the different snow realizations becomes more pronounced, especially for T-MAT and MIE. The T-MAT and MIE models reveal 5–10 dB higher  $\text{DWR}_{K_a, W}$  values compared to LIU and AGG, and this difference is accentuated at the lower  $\Lambda$  range. The almost independence of

<sup>4</sup>Usually, 94 GHz is considered for W-band applications, however, only 89 GHz is included in the AGG dataset

<sup>5</sup>If 94 GHz is used instead of 89 GHz, the  $\text{DWR}_{K_a, W}$  for LIU differs up to 0.5 dB, while for MIE and the lowest  $\Lambda$  values the  $\text{DWR}_{K_a, W}$  for 94 GHz are 1.2 dB larger.

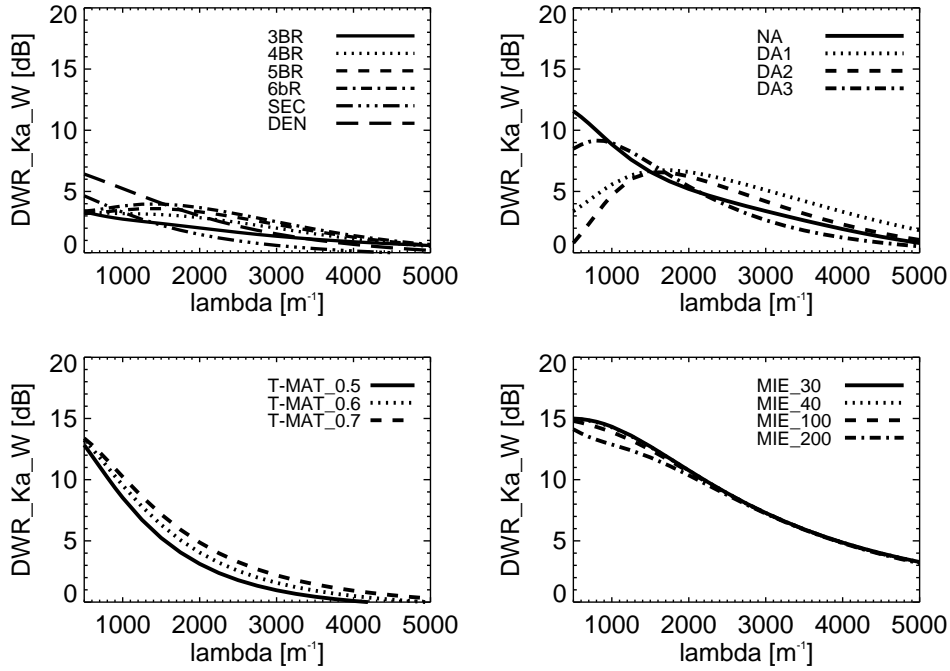


**Figure 7.13:** Same as Fig. 7.12, but DWR is for 36.5 GHz ( $K_a$ -band) and 89 GHz (W-band) [after *Kneifel et al. (2011a)*].

the  $MIE-DWR_{K_a,W}$  values of snow density can also be found at this frequency combination. It is important to note that even if clear similarities between certain particle models can be found for a specific variable and frequency combination (e.g., between AGG and T-MAT at  $DWR_{K_a,K_a}$ ), this does not appear to be simply transferable to other frequency combinations.

The  $DWR-\Lambda$  considerations reveal that when only spherical particles are assumed, the SSD parameter  $\Lambda$  can be directly derived with the DWR even without information about snow density. The derived  $\Lambda$  value can then be used to derive mass-related snow quantities like SWC or, as shown by *Matrosov (1998)*, the SR. For this methodology, the ratio of one of the two  $Z_e$  measurements and the snow quantity (in this study SWC) is needed as a function of  $\Lambda$  (Fig. 7.14). Note that similar to the DWR, the ratio  $Z_e/SWC$  is also independent of the intercept parameter  $N_0$  and only a function of  $\Lambda$  and particle type. Since SWC is related to the mass-size relation (or for spheres to the snow density), the information of the particle type is needed in order to derive SWC with  $Z_e$  and the formerly derived  $\Lambda$ . Compared to AGG, T-MAT and low density spheres, some of the LIU particles (except DEN) display  $Z_e/SWC$  values up to a factor of six higher. This high variability again illustrates the high uncertainty range in radar-based snowfall retrievals introduced by unknown particle habit and/or mass-size relation.

### 7.3 Triple – frequency approach

The above DWR results show that the derivation of  $\Lambda$  using the DWR depends on snow particle type, and only for soft spheres will the DWR be independent of density. Thus, for actual estimates of e.g., SWC, an identification of the particle type is still needed. Depending on the frequency used, the overall dependence on particle type and the differences between

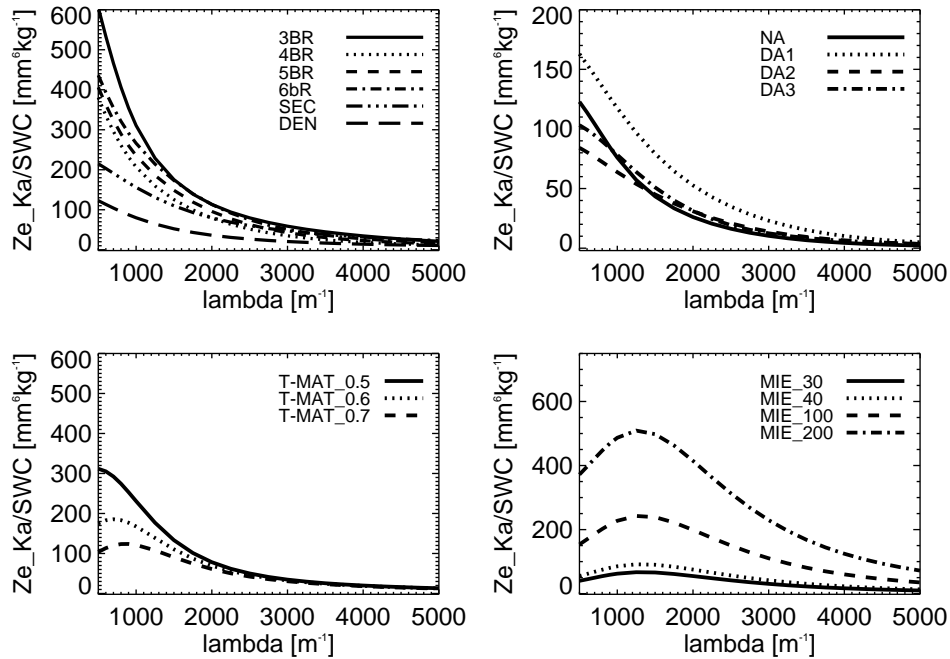


**Figure 7.14:** Ratio of  $Z_e$  over SWC [ $\text{mm}^6\text{kg}^{-1}$ ] at 36.5 GHz as a function of  $\Lambda$  [ $\text{m}^{-1}$ ]. Note that the ratio  $Z_e/\text{SWC}$  is independent of the intercept parameter  $N_0$ . Note further the different scaling for the y-axis for (upper right) AGG and (lower right) MIE. Particle model descriptions are the same as Fig. 7.10 [after *Kneifel et al. (2011a)*].

different particle models can be significant. The question at this point arises, whether a method can be found to determine the particle type. This will be especially important in the low  $\Lambda$  range, i.e. at high SWC with significant contributions from larger particles.

Considering the increasing snow particle type sensitivity at increasing frequency (Fig. 5.3), the idea arises of using a third (higher) frequency for the particle type discrimination. This triple–frequency approach has been investigated for ice and mixed phase clouds e.g. by *Seckelsky et al. (1999)*; *Gaussiat et al. (2003)*; *Yoshida et al. (2006)*. The authors in *Yoshida et al. (2006)* consider ice spheres and hexagonal ice particles with aspect ratios varying from 0.2–5 and volume equivalent sphere radii up to  $500 \mu\text{m}$ .  $\text{DWR}_{X,K_a}$  and  $\text{DWR}_{X,W}$  for their simulated ice particles (see their Fig.5) revealed that it is principally possible to distinguish between ice spheres and the other ice particle habits.

### 7.3.1 Separability of different particle models

In Fig. 7.15 the previously described idea is applied to the different snow particle models and shown as  $\text{DWR}_{K_u,K_a}$  versus  $\text{DWR}_{K_a,W}$ . Since both DWR values are independent of the intercept parameter  $N_0$ , the two DWR measurements are only dependent on  $\Lambda$  and particle type. Fig. 7.15 reveals that especially for large  $\text{DWR}_{K_u,K_a}$  values (related to small  $\Lambda$  values and hence SSD with large fraction of large particles) different particle types can be distinguished. For LIU one generally finds low values ( $< 6$  dB) for both DWR. Note that high  $\text{DWR}_{K_u,K_a}$  values ( $> 6$  dB) together with  $\text{DWR}_{K_a,W}$  values below 10 dB can only be explained with the dendritic AGG models DA1–3. On the other hand, high  $\text{DWR}_{K_u,K_a}$  values ( $> 5$  dB) together with high  $\text{DWR}_{K_a,W}$  values ( $> 10$  dB) are related to needle AGG (NA), spherical

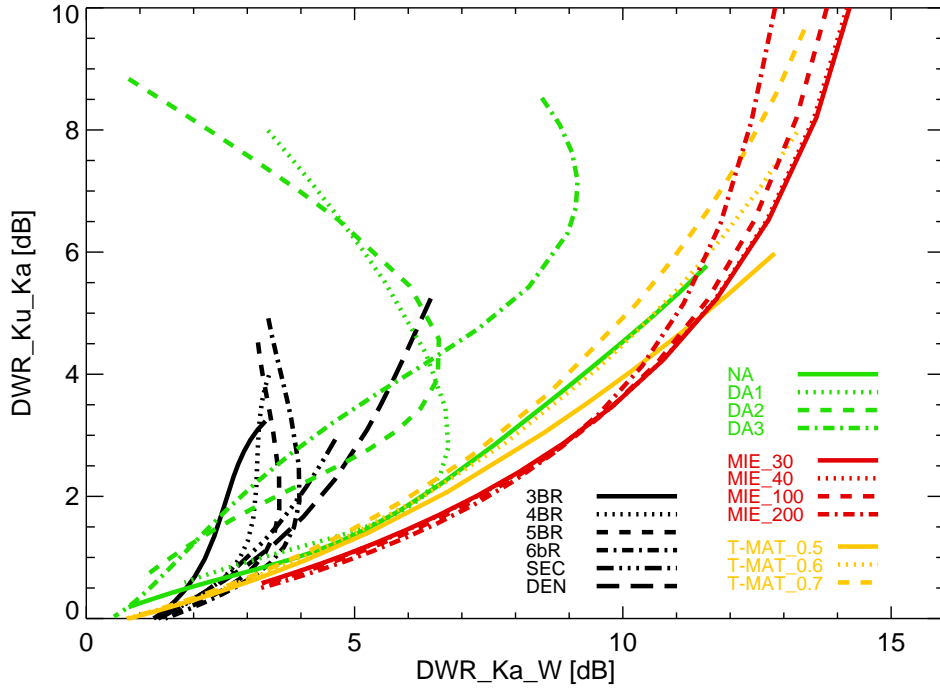


**Figure 7.15:**  $DWR_{Ku,Ka}$  against  $DWR_{Ka,W}$  in dB. Line and color coding are the same as Fig. 7.11 with additional aspect ratios (0.5–0.7) for the T–MAT model and different density assumptions for the MIE soft spheres (30–200  $\text{kgm}^{-3}$ ). Note that all DWR values are independent of the intercept parameter  $N_0$  [after *Kneifel et al. (2011a)*].

and spheroid particles. The spherical models again display a considerably low dependence on the assumed snow density except for the lowest  $\Lambda$  range. Using  $DWR_{Ka,W}$  instead of  $DWR_{Ku,W}$  results in significantly higher DWR values (approx. factor of two) but the overall structure seen in Fig. 7.15 is nearly the same. The triple–frequency approach thus allows different snow particle types to be distinguished — especially for small  $\Lambda$  values. However, the separation of similar particle types with different densities (e.g. soft spheres) remains a challenge. As shown in Fig. 7.12 and 7.13, insensitivity to density is of minor importance for the determination of  $\Lambda$ . In contrast, erroneous assumptions about particle type have large implications for the derived  $\Lambda$ , particularly at the lower  $\Lambda$  range.

### 7.3.2 Separability of mass–size relation

In order to derive mass related quantities like SWC (Fig. 7.14), the mass–size relation becomes critical. For ice particles with well–known mass–size relations (e.g., the pristine LIU particles), the particle type determination implicitly includes the selection of appropriate mass–size parameters  $a$  and  $b$  (Eq. 3.3). However, the particle type determination is not sufficient, if for a given particle shape the parameters  $a$  and  $b$  can vary considerably. For example, it has been observed that the exponent  $b$  is close to two for aggregates (*Field et al., 2005*, and references therein) but the prefactor  $a$  can vary due to e.g., different pristine basis elements that formed the aggregate. Another example would be graupel with different densities: Using the triple–frequency technique, graupel can clearly be distinguished from LIU particles, thereby improving the accuracy of the retrieved  $\Lambda$ . However, since all graupel particles —

regardless of their density — will populate only one region of the triple–frequency diagram, the density–dependent SWC estimate will remain uncertain.

Therefore, in the context of single DWR studies using soft spheres, the addition of a third frequency cannot replace the need for a tuning parameter. However, if one considers actual observations, different particle types are at least to some degree connected to different mass–size relations so that with the aforementioned caveats, the triple–frequency approach should be able to improve both the estimate of  $\Lambda$  and of SWC.

### 7.3.3 Impact of attenuation

Using  $Z_e$  measurements at higher frequencies (especially W–band) implicates that attenuation has to be considered. The attenuation due to atmospheric gases (mainly  $O_2$ ,  $N_2$  and water vapor) at high–latitude winter conditions and at the considered frequencies is considerably low: Given a standard US winter atmosphere with a ground temperature of 273 K and an IYW of  $10 \text{ kgm}^{-2}$ , the total atmospheric (one–way, vertically pointing) attenuation is calculated to be 0.06, 0.27 and 0.59 dB for 13.4, 36.5 and 89 GHz, respectively. Cloud liquid water and snow cause in general higher attenuation especially at radar frequencies above 35 GHz. Knowing the extinction cross section of a certain hydrometeor and its size distribution, the attenuation coefficient  $\alpha$  can be derived according to Eq. 4.45.

*Hiley et al.* (2011) note from a combined active–passive spaceborne perspective that many regions around the globe commonly experience snowfall coincident with non–negligible amounts of cloud liquid water. Assuming an LWC range up to  $0.5 \text{ gm}^{-3}$  and a constant temperature of 268 K, liquid water attenuation is found for 13.4 GHz to be almost negligible with maximum values of  $0.2 \text{ dBkm}^{-1}$ . At 36.5 GHz  $\alpha$  extends  $1 \text{ dBkm}^{-1}$  for the largest LWC values while at 89 GHz the signal is with up to  $4 \text{ dBkm}^{-1}$  considerably attenuated. Note that attenuation by liquid water is dependent on temperature. The reflectivity signal of cloud liquid water (LWC lower than  $0.5 \text{ gm}^{-3}$ ) is lower than  $-20 \text{ dBz}$  and thus can be neglected for the comparisons in this study.

Similar calculations have been performed for the different snow particle models considering SWC values up to  $1 \text{ gm}^{-3}$ . Since the overall patterns are very similar and attenuation at 13.4 and 36.5 GHz is for all models below  $0.1 \text{ dBkm}^{-1}$  and  $1 \text{ dBkm}^{-1}$  respectively, the detailed attenuation signatures in Fig. 7.16 are only discussed for 89 GHz. The different particle models reveal for the same SWC very different absolute values. The pristine LIU particles attenuate the radar signal by up to  $4 \text{ dBkm}^{-1}$  while MIE soft spheres are even exceeding this value. The lowest attenuation values are found with up to  $2 \text{ dBkm}^{-1}$  for AGG and lower than  $1 \text{ dBkm}^{-1}$  for T–MAT. There are two main reasons for the considerably large differences between the particle models: First, the differences of the extinction properties for the single particles tend to increase with increasing frequency and particle size (Fig. 5.2). Second, due to the different mass–size relations (Fig. 3.5) of the different particle models, the related SSD for a specific SWC — and thus the relative amount of large and small particles — can be very different.

Using the triple–frequency approach to estimate particle type and SSD, it should also be possible to derive the related snow attenuation. This could be done successively, starting at the closest range bin and integrating snow attenuation vertically in every step. However, it must be noted that such an attenuation correction should optimally include an integral constraint on the total attenuation and is probably best suited for airborne or spaceborne instruments, that can readily provide total attenuation estimates. For ground–based obser-

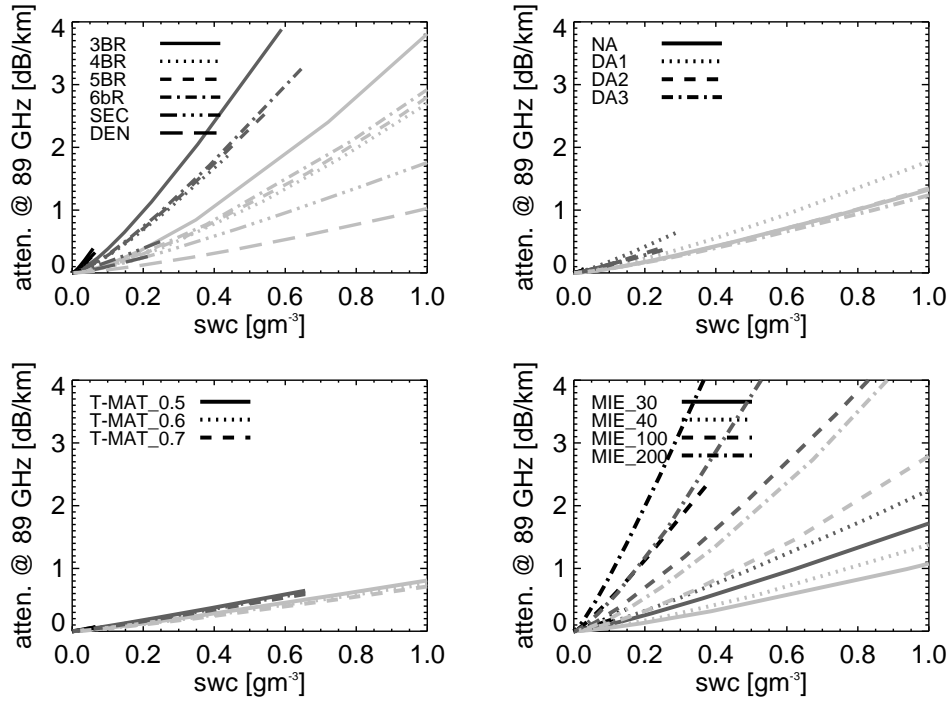


**Figure 7.16:** Two-way attenuation coefficient  $\alpha$  [dBkm<sup>-1</sup>] as a function of SWC [gm<sup>-3</sup>] at W-band. Particle model descriptions are the same as Fig. 7.10. The grey scale indicates  $N_0$  values: (black) 10<sup>5</sup>, (dark grey) 10<sup>6</sup>, and (light grey) 10<sup>7</sup> m<sup>-4</sup> [after *Kneifel et al. (2011a)*].

vations integral constraints for IWV and LWP can be derived e.g. from collocated passive MWR measurements. As shown in chapter (Chapter 6) higher MW observations (e.g. 90 and 150 GHz) could be used in a combined passive-radar retrieval to further constrain the SWP.

In order to investigate the impact of snow attenuation on the particle type separability in Fig. 7.15, a dry 1 km homogeneous snow cloud with a  $N_0$  value of 10<sup>6</sup> m<sup>-4</sup> between the radar and the measured volume is assumed. The resulting attenuated DWR values are shown in Fig. 7.17. Since snow attenuation is dominant at W-band, the largest impact is found for  $DWR_{K_a,W}$  values that increase by 1–4 dB compared to the results without attenuation (Fig. 7.15), especially at the lower  $\Lambda$  range. On the other hand, the changes in  $DWR_{K_u,K_a}$  values are below 1 dB due to the low snow attenuation at the two lower frequencies. Given the large dynamic range observed in the  $DWR_{K_a,W}$ , these results imply that the ice particle model separability of the triple-frequency method is only moderately affected by snow attenuation at W-band. Nevertheless, attenuation will potentially have to be accounted for, when thick precipitating clouds exist.

### 7.3.4 Impact of limited and extended particle size range

As mentioned before, the results might be sensitive to the value of  $D$  at which the SSD integration is terminated. To investigate this issue, the calculations were repeated with the same set of habits and  $\Lambda$  parameters, but the SSD integration was terminated at 5 mm instead of 10 mm. The effect of this different maximum size on the particle type discrimination using  $DWR_{K_u,K_a}$  and  $DWR_{K_a,W}$  is shown in Fig. 7.18(a). As a result of the absence of larger

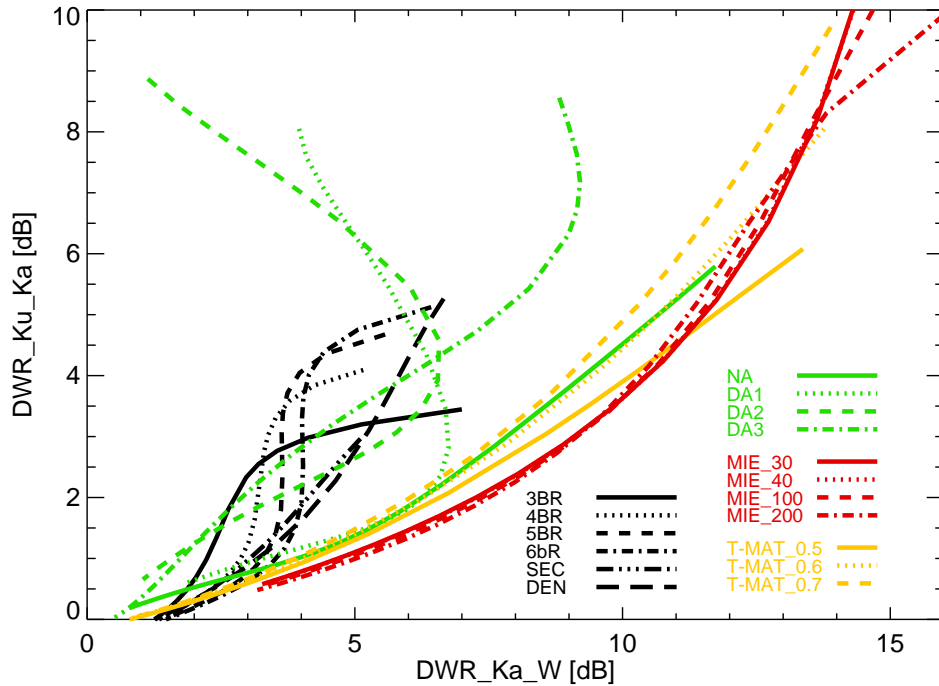


**Figure 7.17:** Same as (a) but including attenuation of a 1 km thick snow cloud with  $N_0 = 10^6 m^{-4}$  [after *Kneifel et al. (2011a)*].

particles, especially the  $DWR_{Ku,Ka}$  values are considerably lower ( $< 6$  dB). However, even though the total DWR range is smaller, particle type discrimination is still possible. The overall patterns also persist, with higher  $DWR_{Ku,Ka}$  values for AGG compared to LIU, and the higher DWR values for MIE at both frequency combinations.

For the AGG model, scattering calculations exist up to particle sizes of 16–25 mm. In order to investigate the effect of larger aggregate sizes, the calculations for every particle type and set  $D$  were repeated up to the maximum available particle size (Fig. 7.18(b)). A comparison of Fig. 7.15 and Fig. 7.18(b) reveals that the increased particle size leads to a 1–2 dB increase of  $DWR_{Ku,Ka}$  (especially for NA and DA3) and a 1–3 dB decrease of  $DWR_{Ka,W}$  values. Therefore, increasing the particle size range towards realistic snow sizes further improves the habit separability with the triple–frequency approach.

It has been shown in this chapter that existing low–end FM–CW radar systems like the MRR are able to provide valuable measurements during snowfall if the considered height and sensitivity range can be narrowed e.g. for the observation of snowfall close to the ground instead of observing the whole snow cloud system. Such low–maintenance systems can be an important addition to current cloud radar systems if e.g. the measuring site is unable to provide the necessary power and maintenance supply needed for high end systems. In the second part, multi–frequency approaches have been explored with respect to their potential to constrain microphysical assumptions like SSD or particle habit that are the two main reasons for uncertainties in current radar snowfall retrievals. It could be shown that the density independence for the dual–frequency approach and its advantage to derive  $\Lambda$  is only valid for spherical particles. For non–spheroid particle habits the information about the habit is still needed. The dual–frequency approach was thus extended towards a third frequency. That

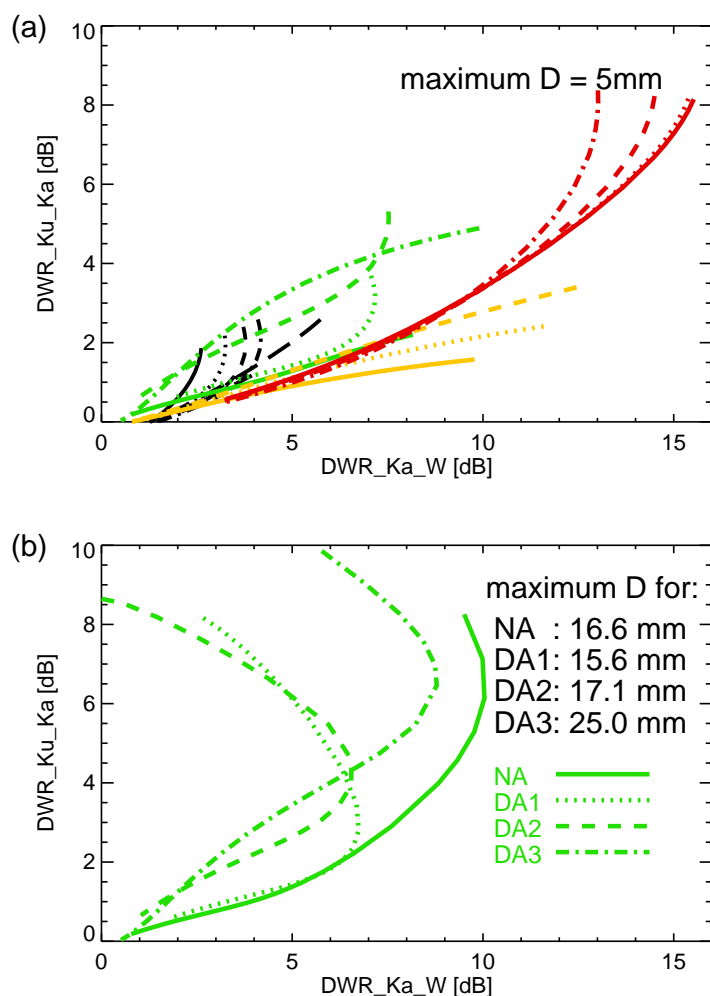


**Figure 7.18:** Same as Fig. 7.15 but for (a) SSD with maximum particle sizes  $D$  of 5 mm and (b) for only AGG but SSD up to the maximum available size [after *Kneifel et al. (2011a)*].

was shown to be able to allow a first separation of different particle habits and thus enables to reduce the ambiguity for the derivation of  $\Lambda$ . Future developments of these techniques will rely on the extension of realistical snow scattering databases including large aggregates as well as combined measurements of in-situ snowfall properties and multi-frequency radar quantities.



# Chapter 8

## Conclusions and Outlook

### 8.1 Conclusions

The overall question of this thesis was which information content about snow clouds can be gained by ground-based MW remote sensing observations. In order to answer this question, radiative transfer simulations were performed for active and passive MW sensors. The simulations included various state-of-the-art snow particle models that allowed analyzing the impact of the different snow habits on passive and active scattering signals. Other relevant parameters like SSD, ground surface emissivity and vertical liquid water profile were included in the sensitivity analysis in order to compare their impacts on snow particle habit. In order to compare the RT simulations to real measurements, a six-months winter time period of snowfall observations by passive and active remote sensors has been analyzed. These data were obtained at an alpine site during the TOSCA project.

#### **Ground-based passive MW observations reveal snowfall scattering signal**

The scattering effect of snowfall ( $T_B$  depression) in the passive MW has so far only been shown for downward measuring satellite and airborne sensors. RT simulations predicted an analogous  $T_B$  enhancement in ground-based zenith measurements. This effect could be proven for the first time to be real by analyzing the TOSCA dataset (Chapter 6). The proposed snow scattering effect of a  $T_B$  enhancement in ground-based measurements could be identified at 90 and 150 GHz with the help of a 35 GHz cloud radar. Within a snowfall case study, the  $T_B$  enhancement effect was quantified: The radar derived SWP values (up to  $0.2 \text{ kgm}^{-2}$ ) lead to a  $T_B$  enhancement of about 8 K at 150 GHz and 4 K at 90 GHz, while at 31.4 GHz the signal change was below 1 K. The latter is particularly important, since derived LWP and IWV values from low-frequency channels would else be contaminated by snow scattering.

Significant amounts of liquid water (LWP up to  $100 \text{ gm}^{-2}$ ) were detected during the investigated snow fall event. Their vertical distribution and, thus, their temperature dependent emission were simulated for extreme cloud positions. The simulations revealed that the uncertainty in the liquid water profile is able to totally obscure the snow scattering signal.

Since non-negligible amounts of super-cooled liquid water have also been found in several aircraft studies as well as in the entire TOSCA dataset, the accurate modelling of the radiative properties of super-cooled water is essential for every snow retrieval algorithm using microwave frequencies for both ground-based and satellite observations. The observed  $T_B$

enhancement can be reproduced by simulations using idealized snow crystals with realistic assumptions on SWP and SSD taken from radar and disdrometer measurements. In the given parameter range, the snow scattering signal depends in similar order on varying SWP, shape and  $N_0$ . Hence, the question, if the scattering properties of the idealized crystals are representative for natural snow, could not be answered due to the uncertainty in SSD and SWP. For the analysed case, the amplitude of the  $T_B$  enhancement observed by a ground-based sensor is by a factor of two higher than that of the  $T_B$  depression measured by a nadir viewing sensor, while showing similar sensitivities to SSD and particle shape. In addition, ground-based observations are less affected by the unknown ground surface emissivity.

### **Snowfall observations are possible with a MRR**

The other major focus of the presented study was snowfall observation with active remote sensors (Chapter 7). Collocated measurements of a MRR and a MIRA36 cloud radar during TOSCA were used to analyze the capabilities of the MRR of snowfall observations (Section 7.1). An MRR data processing algorithm suited for snowfall was developed, since the original processing is only valid for rainfall. The two radar systems operate at frequencies already in the Mie scattering regime. Due to the 11.4 GHz frequency difference, a relation to convert the 24.1 GHz  $Z_e$  into 35.5 GHz equivalent  $Z_e$  was derived utilizing different snow particle habits and SSD parameterizations. This conversion allowed to directly compare the observations of the two radar systems. The differences in the mean Doppler velocity were found to be below  $0.3 \text{ ms}^{-1}$ . The  $Z_e$  differences were below 1 dBz for  $Z_e$  greater than 3 dBz, after applying the frequency conversion. The direct comparison of the MRR to MIRA36 clearly revealed a transition of the MRR reflectivities from signal into the noise floor at lower values. The noise level found in this direct comparison agrees well with the noise levels estimated by an analysis of several clear-sky observations. Thus, the MRR noise level can also be easily estimated without a high-end system for direct comparison. In order to answer the question whether the limited sensitivity of the MRR has a significant impact on the estimated snow accumulation, the dataset of MIRA36  $Z_e$  observations of the whole time period were used and recently published  $Z_e$ -SR relations were applied to the data. Due to the limited sensitivity of the MRR, snowfall rates below  $0.01$ – $0.15 \text{ mmh}^{-1}$  are probably missed by the MRR, depending on snow particle habit and snow particle size distributions. The effect of such low snowfall rates on total snow accumulation was, however, surprisingly low. It is important to note, however, that these results are only representative for locations with similar  $Z_e$  distributions. The remaining 7% difference in the estimated total snow accumulation from both instruments is mainly due to the slight  $Z_e$  overestimation of the MRR at low  $Z_e$  values. In addition, considerable variability is also introduced by the various snow particle types that cause deviations from the mean  $Z_e$  conversion relation.

Overall, the MRR was found to be a valuable instrument to observe mid-latitude snowfall at heights below 3 km. The MRR provides great advantages for dry snowfall observations in remote areas due to its relatively low power consumption, maintenance, and size under the restriction of limited sensitivity and height resolution.

### **Triple-frequency radar observations reveal a potential to distinguish between snow particle classes**

In accordance to former studies, this thesis confirmed that the various microphysical snowfall parameters can only be disentangled with a combination of active and passive techniques at

multiple frequencies. Considering radar-only approaches, several dual and triple-frequency methods have already been developed in the last few years. However, these studies mostly considered spheroid particle models for their simulations. The results in this thesis revealed that e.g. the density-independence of the dual-wavelength ratio (Section 7.2) is no longer valid when realistic particle models are applied. This implicates that the “classical” dual wavelength approach has to be expanded in order to achieve the necessary information about the particle habit. The combination of three radar frequencies was identified within this study to be a possible approach. The use of W-band in addition to the more traditional  $K_u/K_a$ -band combination adds significant physical information, especially for SSD with low size distribution slope parameter  $\Lambda$  values, when larger particles dominate the backscatter signal. The resulting W-band signature is dominated by Mie-scattering, thus allowing different snow particle habits to be separated in concurrent  $K_u/K_a$ -band and  $K_a/W$ -band DWR and also yielding a reduction of the uncertainty in the determination of the slope parameter  $\Lambda$ . Despite this improvement, it has to be noted that for particles with similar shape but variable mass-size relations (e.g., graupel) the unknown mass-size relation still significantly affects retrieved mass-related quantities such as SWC. This uncertainty will be reduced by the proposed approach only to the extent to which the mass-size relation is implicitly determined by particle habit.

Ongoing analysis of airborne triple-frequency radar observations during the Wakasa Bay campaign (Lobl et al., 2007) shows encouraging results: Despite the disadvantageous beam widths of the three radar instruments, the proposed “aggregate area” is clearly distinguishable from the spheroid mode in the data<sup>1</sup>. Additional future triple-frequency observation will thus shed light on the question what can be gained from triple-frequency radar observations.

## 8.2 Outlook

### Low-power systems for snowfall observations in remote areas

If the noise level of the MRR can further be reduced (e.g. by using the raw data and improving the mean noise level estimation technique) thus enhancing the MRR sensitivity to low SR, the MRR could be used for climatological studies e.g. in the polar regions. The much lower costs of the MRR (only 1/20 of the MIRA36) makes it particularly attractive for radar network applications. Data from already existing MRR networks for rain observations could be reprocessed for dry snowfall observations. Even if the quantitative estimation of SR using a single-frequency radar is affected by large uncertainties, the MRR observations can be used to distinguish between snow/ice, rain and melting layer region within the cloud. Particularly in polar regions, the discrimination between blowing snow and snowfall is a critical issue and impossible to achieve with in-situ disdrometers or snow accumulation measurements. Using the vertical information of the MRR this discrimination can be achieved, since blowing snow is limited to the lowest height levels, while snowfall is usually connected to a vertically extended column of hydrometeors.

---

<sup>1</sup>Simulations similar to Section 7.3 were contributed to a study by Leinonen et al. (in preparation for submission to Geophys. Res. Lett.)

### Polarization and higher frequency radar

Polarization measurements from passive MWR can deliver information whether the snow particles are oriented. Ongoing studies (*Xie et al., 2011*) reveal that even larger snowflakes show polarization signals that can only be explained by particle orientation. Future projects focussing on snow particle type distinction could also potentially include polarization measurements from active sensors as, e.g., the depolarization ratio at K<sub>a</sub>-band which can be used to distinguish between drizzle, pristine and irregular shaped ice particles (*Reinking et al., 2002*). Other studies have proposed using polarimetric signatures at higher frequencies (e.g., 94 and 220 GHz) to differentiate ice crystal habits of up to 2 mm in size (*Aydin and Walsh, 1999*), so similar studies can be performed using complex aggregate models at larger particle sizes to further assess the potential of polarimetric data for snowfall applications. Similarly, higher frequency radar (e.g. 150 GHz, 220 GHz) might be useful for cloud observations, especially from the differential attenuation perspective. Initial scattering calculations performed at 160 GHz revealed that the increasing Mie oscillation effects of the mass backscattering lead to an increasing overlap of the particle types in the DWR plane. This will potentially reduce the effectiveness of additional higher frequency radar observations for habit distinction. A more rigorous analysis of this topic is required, however, before any definite conclusions can be drawn about whether higher frequency radar observations will enable improved particle type determination.

### Improvement of in-situ techniques

Improved ground-based in-situ techniques are needed for any measurement scenario in order to capture the complex parameters of snowfall. Current optical 2D techniques (e.g. the 2DVD) should further be developed to be able to measure the full 3D structure of snow particles. In addition to the optical information, a direct measure of physical quantities like snow particle mass is essential. Those sensors would be predominant compared to current methods that relate 2D particle projections to integrated snow mass.

Any snowfall — spaceborne or ground-based — retrieval will not only depend on the appropriate description of snowfall microphysics and its radiative properties but also on the characterization of SLW. Laboratory measurements of the refractive index of SLW in the MW region are highly desirable. In-situ techniques, like the balloon-borne LWC sensor developed by *Hill (1994)* should be refined in order to validate e.g. dual-frequency radar LWC retrievals (*Hogan et al., 2005*) and MWR LWP retrievals.

### Single scattering databases for complex snow particles

Very few scattering datasets currently exist for complex snow particles and aggregates. The aggregate models presented by *Petty and Huang (2010)* used in this study have been generated based on observations and certain basic crystals (dendrites, needles). While these aggregate particles mark a significant step forward in our understanding of scattering properties, it will be important to include aggregates generated using other methods, e.g., fractal particles (*Ishimoto, 2008*) in future studies. Special emphasis should be taken to construct aggregates consistent with observed mass-size relations (Section 3.3, Eq. 3.3) (e.g., the  $b$  exponent in the mass-size relations should be close to two). Model results for a larger variety of aggregates would especially be helpful to further investigate the dependence of scattering parameters on aggregate habit properties (e.g., fractal dimension).

### Combined active/passive multi-frequency observations

Several ground-based cloud radar systems (e.g., at the ARM sites) are currently upgraded to multi-frequency systems. In recent years, mobile integrated triple-frequency radar systems (*McLinden*, 2010) have also been developed and are available for field campaigns to provide simultaneous measurements at  $K_u$ -,  $K_a$ -, and  $W$ -bands. These observations will provide further insight whether different particle habits can be separated. This would give a unique possibility to observe snowfall microphysics, e.g. the interaction of snow particle habits in the vicinity of super-cooled liquid water. An important future effort will also be to perform detailed information content analysis including available sensors and microphysical parameters e.g. within an optimal estimation approach (e.g. *Löhnert et al.*, 2009). Those analyses can deliver important information about which instruments contribute most or least to a certain microphysical parameter. Such an approach, however, extremely depends on the characterization of the a priori fields, e.g. the vertical distribution of snow and liquid water. Further, the analysis can only deliver valid results, if appropriate scattering and emission databases for the various atmospheric constituents are available.

In future studies it will be important to perform simultaneous observation of microphysical snowfall parameters and remote sensing measurements. Mountainous sites — like the UFS — can provide particular advantages for such an effort: In-situ measurements can be performed at a higher elevation (summit) while the remote sensors are placed several hundred meters lower. In such a way, the in-situ data can be matched to the first usable range gate of a radar systems (usually a few hundred meters apart from the radar). This setup allows in-situ and remote sensing information from approximately the same atmospheric volume or at least the same atmospheric height level. Such long-term datasets from various climatic regions can then be used to develop appropriate snow particle models and can help to improve microphysical parameterizations.



# List of Acronyms

2DVD .....	<b>2D</b> -Video <b>D</b> isdrometer
AMSR .....	<b>A</b> dvanced <b>M</b> icrowave <b>S</b> canning <b>R</b> adiometer
AMSU .....	<b>A</b> dvanced <b>M</b> icrowave <b>S</b> ounding <b>U</b> nits
ARM .....	<b>A</b> tmospheric <b>R</b> adiation <b>M</b> easurement
CPR .....	<b>C</b> loud <b>P</b> rofilng <b>R</b> adar
DDA .....	<b>D</b> iscrete <b>D</b> ipole <b>A</b> pproximation
DMSP .....	<b>D</b> efense <b>M</b> eteorological <b>S</b> atellite <b>P</b> rogram
DPR .....	<b>D</b> ual <b>P</b> olarization <b>R</b> adiometer
DWD .....	<b>D</b> eutscher <b>W</b> etter <b>D</b> ienst
DWR .....	<b>D</b> ual <b>W</b> avelength <b>R</b> atio
FM-CW .....	<b>F</b> requency <b>M</b> odulated – <b>C</b> ontinuous <b>W</b> ave
GCM .....	<b>G</b> lobal <b>C</b> limate <b>M</b> odel
GPM .....	<b>G</b> lobal <b>P</b> recipitation <b>M</b> easurement mission
HATPRO .....	<b>H</b> umidity and <b>T</b> emperature <b>P</b> ROfiler
HPBW .....	<b>H</b> alf <b>P</b> ower <b>B</b> eam <b>W</b> idth
IWP .....	<b>I</b> ce <b>W</b> ater <b>P</b> ath
LIDAR .....	<b>L</b> ight <b>D</b> etection and <b>R</b> anging
LWC .....	<b>L</b> iquid <b>W</b> ater <b>C</b> ontent
MHS .....	<b>M</b> icrowave <b>H</b> umidity <b>S</b> ounder
MRR .....	<b>M</b> icro <b>R</b> ain <b>R</b> adar
MW .....	<b>M</b> icrowave
MWR .....	<b>M</b> icrowave <b>R</b> adiometer
NWP .....	<b>N</b> umerical <b>W</b> eather <b>P</b> rediction
PDF .....	<b>P</b> robability <b>D</b> ensity <b>F</b> unction
RTE .....	<b>R</b> adiative <b>T</b> ransfer <b>E</b> quation
RTM .....	<b>R</b> adiative <b>T</b> ransfer <b>M</b> odel
SLW .....	<b>S</b> uper-cooled <b>L</b> iquid <b>W</b> ater
SR .....	<b>S</b> nowfall <b>R</b> ate
SR .....	<b>S</b> nowfallrate
SSD .....	<b>S</b> now <b>S</b> ize <b>D</b> istribution
SSM/I .....	<b>S</b> pecial <b>S</b> ensor <b>M</b> icrowave <b>I</b> mager
SWC .....	<b>S</b> now <b>W</b> ater <b>C</b> ontent
SWP .....	<b>S</b> now <b>W</b> ater <b>P</b> ath
TOSCA .....	<b>T</b> owards an <b>O</b> ptimal estimation based <b>S</b> now <b>C</b> haracterization <b>A</b> lgorithm
TRMM .....	<b>T</b> ropical <b>R</b> ainfall <b>M</b> easurement <b>M</b> ission
UFS .....	<b>U</b> mweltforschungsstation <b>S</b> chneefernerhaus





# Bibliography

- Atlas, D., R. C. Srivasta, and R. S. Sekhon, Doppler radar characteristics of precipitation at vertical incidence, *Rev. Geophys.*, 11, 1–35, 1973.
- Auer, A. H. and D. L. Veal, Dimension of ice crystals in natural clouds, *J. Atmos. Sci.*, 27, 919–&, 1970.
- Austin, R. T., A. J. Heymsfield, and G. L. Stephens, Retrieval of ice cloud microphysical parameters using the CloudSat millimeter-wave radar and temperature, *J. Geophys. Res.*, 114, D00A23, 2009.
- Aydin, K. and T. Walsh, Millimeter wave scattering from spatial and planar bullet rosettes, *IEEE Trans. Geosci. Remote Sensing*, 37, 1138–1150, 1999.
- Barber, P. and C. Yeh, Scattering of electromagnetic waves by arbitrarily shaped dielectric bodies, *Appl. Opt.*, 14, 2864–2872, 1975.
- Barnett, T. P., L. Dümenil, U. Schliese, and E. Roeckner, The effect of Eurasian snow cover on global climate, *Science*, 239, 504–507, 1988.
- Battaglia, A., S. Tanelli, S. Kobayashi, D. Zrnica, R. J. Hogan, and C. Simmer, Multiple-scattering in radar systems: A review, *J. Quant. Spectrosc. Radiat. Transf.*, 111, 917–947, 2010.
- Bennartz, R. and P. Bauer, Sensitivity of microwave radiances at 85–183 GHz to precipitating ice particles, *Radio Sci.*, 38, 8075, 2003.
- Bennartz, R. and G. W. Petty, The sensitivity of microwave remote sensing observations of precipitation to ice particle size distributions, *J. Appl. Meteorol.*, 40, 345–364, 2001.
- Bertolini, D., M. Cassettari, and G. Salvetti, The dielectric relaxation time of supercooled water, *J. Chem. Phys.*, 76, 3285–3290, 1982.
- Böhme, T., N. Van Lipzig, L. Delobbe, E. Goudenhoofdt, and A. Seifert, Evaluation of microphysical assumptions of the COSMO model using radar and rain gauge observations, *Meteorol. Z.*, 20, 133–144, 2011.
- Bohren, C. F. and D. R. Huffman, *Absorption and Scattering of Light by Small Particles*, John Wiley & Sons, Inc., 1983.
- Botta, G., K. Aydin, and J. Verlinde, Modeling of Microwave Scattering From Cloud Ice Crystal Aggregates and Melting Aggregates: A New Approach, *IEEE Geosci. Remote Sens. Lett.*, 7, 572–576, 2010.

- Boudala, F. S., G. A. Isaac, S. G. Cober, and Q. Fu, Liquid fraction in stratiform mixed-phase clouds from in situ observations, *Q. J. R. Meteorol. Soc.*, 130, 2919–2931, 2004.
- Braham, R. R., Snow particle-size spectra in lake effect snows, *J. Appl. Meteorol.*, 29, 200–207, 1990.
- Brandes, E. A., K. Ikeda, G. Thompson, and M. Schönhuber, Aggregate terminal velocity/temperature relations, *J. Appl. Meteorol. Climatol.*, 47, 2729–2736, 2008.
- Brandes, E. A., K. Ikeda, G. Zhang, M. Schönhuber, and R. M. Rasmussen, A statistical and physical description of hydrometeor distributions in Colorado snowstorms using a video disdrometer, *J. Appl. Meteorol. Climatol.*, 46, 634–650, 2007.
- Cadeddu, M. P. and D. D. Turner, Evaluation of water permittivity models from ground-based observations of cold clouds at frequencies between 23 and 170 GHz, *IEEE Trans. Geosci. Remote Sensing*, 49, 2999–3008, 2011.
- Cha, J.-W., K.-H. Chang, S. S. Yum, and Y.-J. Choi, Comparison of the Bright Band Characteristics Measured by Micro Rain Radar (MRR) at a Mountain and a Coastal Site in South Korea, *Adv. Atmos. Sci.*, 26, 211–221, 2009.
- Crewell, S., K. Ebell, U. Löhnert, and D. Turner, Can liquid water profiles be retrieved from passive microwave zenith observations?, *Geophys. Res. Lett.*, 36, 2009.
- Crewell, S. and U. Löhnert, Accuracy of cloud liquid water path from ground-based microwave radiometry 2. Sensor accuracy and strategy, *Radio Sci.*, 38, 2003.
- Crewell, S. and U. Löhnert, Accuracy of boundary layer temperature profiles retrieved with multifrequency multiangle microwave radiometry, *IEEE Trans. Geosci. Remote Sensing*, 45, 2195–2201, 2007.
- Deeter, M. N. and K. F. Evans, A novel ice–cloud retrieval algorithm based on the millimeter-wave imaging radiometer (MIR) 150– and 220–GHz channels, *J. Appl. Meteorol.*, 39, 623–633, 2000.
- Draine, B. T. and P. J. Flatau, Discrete-dipole approximations for scattering calculations, *Journal of the Optical Society of America A*, 11, 1491–1499, 1994.
- Draine, B. T. and P. J. Flatau, *User Guide to the Discrete Dipole Approximation Code DDSCAT 7.1*, 2010, available at <http://arXiv.org/abs/1002.1505v1>.
- Eliasson, S., S. A. Buehler, M. Milz, P. Eriksson, and V. O. John, Assessing observed and modelled spatial distributions of ice water path using satellite data, *Atmos. Chem. Phys.*, 11, 375–391, 2011.
- Ellison, W. J., Permittivity of pure water, at standard atmospheric pressure, over the frequency range 0–25 THz and the temperature range 0–100 degrees C, *J. Phys. Chem. Ref. Data*, 36, 1–18, 2007.
- Evans, K. F. and G. L. Stephens, A new polarized atmospheric radiative–transfer model, *J. Quant. Spectrosc. Radiat. Transf.*, 46, 413–423, 1991.

- Evans, K. F. and G. L. Stephens, Microwave radiative-transfer through clouds composed of realistically shaped ice crystals. Part II: Remote-sensing of ice clouds, *J. Atmos. Sci.*, 52, 2058–2072, 1995.
- Evans, K. F., J. R. Wang, P. E. Racette, G. Heymsfield, and L. H. Li, Ice cloud retrievals and analysis with the compact scanning submillimeter imaging radiometer and the cloud radar system during CRYSTAL FACE, *J. Appl. Meteorol.*, 44, 839–859, 2005.
- Field, P. R., A. J. Heymsfield, and A. Bansemer, Shattering and particle interarrival times measured by optical array probes in ice clouds, *J. Atmos. Ocean. Technol.*, 23, 1357–1371, 2006.
- Field, P. R., A. J. Heymsfield, and A. Bansemer, Snow size distribution parameterization for midlatitude and tropical ice clouds, *J. Atmos. Sci.*, 64, 4346–4365, 2007.
- Field, P. R., R. J. Hogan, P. R. A. Brown, A. J. Illingworth, T. W. Choullarton, and R. J. Cotton, Parametrization of ice-particle size distributions for mid-latitude stratiform cloud, *Q. J. R. Meteorol. Soc.*, 131, 1997–2017, 2005.
- Garnett, J. C. M., Colours in metal glasses and in metallic films, *Philosophical Transactions of the Royal Society of London. Series A*, 203, pp. 385–420, 1904.
- Gasiewski, A. J., Numerical sensitivity analysis of passive EHF and SMMW channels to tropospheric water-vapor, clouds, and precipitation, *IEEE Trans. Geosci. Remote Sensing*, 30, 859–870, 1992.
- Gaussiat, N., H. Sauvageot, and A. J. Illingworth, Cloud liquid water and ice content retrieval by multiwavelength radar, *J. Atmos. Ocean. Technol.*, 20, 1264–1275, 2003.
- Gosset, M. and H. Sauvageot, A dual-wavelength radar method for ice water characterization in mixed-phased clouds, *J. Atmos. Ocean. Technol.*, 9, 538–547, 1992.
- Greco, M. and W. S. Olson, Precipitating snow retrievals from combined airborne cloud radar and millimeter-wave radiometer observations, *J. Appl. Meteorol. Climatol.*, 47, 1634–1650, 2008.
- Groisman, P. Y., T. R. Karl, and R. W. Knight, Observed impact of snow cover on the heat-balance and the rise of continental spring temperatures, *Science*, 263, 198–200, 1994.
- Gunn, K. L. S. and J. S. Marshall, The distribution with size of aggregate snowflakes, *J. Meteorol.*, 15, 452–461, 1958.
- Han, Y. and E. R. Westwater, Analysis and improvement of tipping calibration for ground-based microwave radiometers, *IEEE Trans. Geosci. Remote Sensing*, 38, 1260–1276, 2000.
- Hanesch, M., Fall velocity and shape of snowflakes, PhD Thesis, Swiss Federal Institute Of Technology Zürich, 1999.
- Harlow, R. C., Millimeter microwave emissivities and effective temperatures of snow-covered surfaces: Evidence for Lambertian surface scattering, *IEEE Trans. Geosci. Remote Sensing*, 47, 1957–1970, 2009.

- Haynes, J. M., R. T. Marchand, Z. Luo, A. Bodas-Salcedo, and G. L. Stephens, A multipurpose radar simulation package: QuickBeam, *Bull. Amer. Meteorol. Soc.*, 88, 1723–1727, 2007.
- Hewison, T. J. and S. J. English, Airborne retrievals of snow and ice surface emissivity at millimeter wavelengths, *IEEE Trans. Geosci. Remote Sensing*, 37, 1871–1879, 1999.
- Heymsfield, A. J., A. Bansemer, P. R. Field, S. L. Durden, J. L. Stith, J. E. Dye, W. Hall, and C. A. Grainger, Observations and parameterizations of particle size distributions in deep tropical cirrus and stratiform precipitating clouds: Results from in situ observations in TRMM field campaigns, *J. Atmos. Sci.*, 59, 3457–3491, 2002.
- Heymsfield, A. J., A. Protat, R. T. Austin, D. Bouniol, R. J. Hogan, J. Delanoe, H. Okamoto, K. Sato, G.-J. van Zadelhoff, D. P. Donovan, and Z. Wang, Testing IWC retrieval methods using radar and ancillary measurements with in situ data, *J. Appl. Meteorol. Climatol.*, 47, 135–163, 2008.
- Hiley, M. J., M. S. Kulie, and R. Bennartz, Uncertainty Analysis for CloudSat Snowfall Retrievals, *J. Appl. Meteorol. Climatol.*, 50, 399–418, 2011.
- Hill, G. E., Analys of supercooled liquid water measurements using microwave radiometer and vibrating-wire devices, *J. Atmos. Ocean. Technol.*, 11, 1242–1252, 1994.
- Hobbs, P. V., S. Chang, and J. Locatteli, Dimensions and aggregation of ice crystals in natural clouds, *J. Geophys. Res.*, 79, 2199–2206, 1974.
- Hogan, R. J., N. Gaussiat, and A. J. Illingworth, Stratocumulus liquid water content from dual-wavelength radar, *J. Atmos. Ocean. Technol.*, 22, 1207–1218, 2005.
- Hogan, R. J., A. J. Illingworth, and H. Sauvageot, Measuring crystal size in cirrus using 35- and 94-GHz radars, *J. Atmos. Ocean. Technol.*, 17, 27–37, 2000.
- Hogan, R. J., M. P. Mittermaier, and A. J. Illingworth, The retrieval of ice water content from radar reflectivity factor and temperature and its use in evaluating a mesoscale model, *J. Appl. Meteorol. Climatol.*, 45, 301–317, 2006.
- Hong, G., Parameterization of scattering and absorption properties of nonspherical ice crystals at microwave frequencies, *J. Geophys. Res.*, 112, D11208, 2007a.
- Hong, G., Radar backscattering properties of nonspherical ice crystals at 94 GHz, *J. Geophys. Res.*, 112, D22203, 2007b.
- Hosler, C. L. and R. E. Hallgren, The aggregation of small ice crystals, *Discussions of the Faraday Society*, pages 200–207, 1960.
- Hosler, C. L., D. C. Jensen, and L. Goldshlak, On the aggregation of ice crystals to form snow, *J. Meteorol.*, 14, 415–420, 1957.
- Houze, R. A., P. V. Hobbs, P. H. Herzegh, and D. B. Parsons, Size distributions of precipitation particles in frontal clouds, *J. Atmos. Sci.*, 36, 156–162, 1979.
- Iguchi, T., T. Kozu, R. Meneghini, J. Awaka, and K. Okamoto, Rain-profiling algorithm for the TRMM precipitation radar, *J. Appl. Meteorol.*, 39, 2038–2052, 2000.

- IPCC, Climate change 2007: The physical science basis., Contribution of working group I to the Fourth Assessment Report of the Intergovernmental Panel on Climate Change, Cambridge University Press, Cambridge, United Kingdom and New York, NY, USA, 2007.
- Ishimoto, H., Radar backscattering computations for fractal-shaped snowflakes, *J. Meteorol. Soc. Jpn.*, 86, 459–469, 2008.
- Kajikawa, M., Observations of the falling motion of plate-like snow crystals Part1: The free-fall patterns and velocity variations of unrimed crystals, *J. Meteorol. Soc. Jpn.*, 70, 1–9, 1992.
- Katsumata, M., H. Uyeda, K. Iwanami, and G. S. Liu, The response of 36-and 89-GHz microwave channels to convective snow clouds over ocean: Observation and modeling, *J. Appl. Meteorol.*, 39, 2322–2335, 2000.
- Kim, M.-J., Single scattering parameters of randomly oriented snow particles at microwave frequencies, *J. Geophys. Res.*, 111, D14201, 2006.
- Kim, M.-J., M. S. Kulie, C. O’Dell, and R. Bennartz, Scattering of ice particles at microwave frequencies: A physically based parameterization, *J. Appl. Meteorol. Climatol.*, 46, 615–633, 2007.
- Kneifel, S., M. S. Kulie, and R. Bennartz, A triple-frequency approach to retrieve microphysical snowfall parameters, *J. Geophys. Res.*, 116, D11203, 2011a.
- Kneifel, S., U. Löhnert, A. Battaglia, S. Crewell, and D. Siebler, Snow scattering signals in ground-based passive microwave radiometer measurements, *J. Geophys. Res.*, 115, D16214, 2010.
- Kneifel, S., M. Maahn, G. Peters, and C. Simmer, Observation of snowfall with a low-power FM-CW K-band radar (Micro Rain Radar), *Meteorol. Atmos. Phys.*, 113, 75–87, 2011b.
- Korolev, A. and G. A. Isaac, Shattering during sampling by OAPs and HVPS. Part I: Snow particles, *J. Atmos. Ocean. Technol.*, 22, 528–542, 2005.
- Korolev, A. V., E. F. Emery, J. W. Strapp, S. G. Cober, G. A. Isaac, M. Wasey, and D. Marcotte, Small ice particles in tropospheric clouds: fact or artifact? Airborne Icing Instrumentation Evaluation Experiment, *Bull. Amer. Meteor. Soc.*, 2011, [Early Online release].
- Kruger, A. and W. F. Krajewski, Two-dimensional video disdrometer: A description, *J. Atmos. Ocean. Technol.*, 19, 602–617, 2002.
- Kulie, M. S. and R. Bennartz, Utilizing spaceborne radars to retrieve dry snowfall, *J. Appl. Meteorol. Climatol.*, 48, 2564–2580, 2009.
- Kulie, M. S., R. Bennartz, T. J. Greenwald, Y. Chen, and F. Weng, Uncertainties in microwave properties of frozen precipitation implications for remote sensing and data assimilation, *J. Atmos. Sci.*, 67, 3471–3487, 2010.
- Kummerow, C., W. S. Olson, and L. Giglio, A simplified scheme for obtaining precipitation and vertical hydrometeor profiles from passive microwave sensors, *IEEE Trans. Geosci. Remote Sensing*, 34, 1213–1232, 1996.

- Kusunoki, K., M. Murakami, N. Orikasa, M. Hoshimoto, Y. Tanaka, Y. Yamada, H. Mizuno, K. Hamazu, and H. Watanabe, Observations of quasi-stationary and shallow orographic snow clouds: Spatial distributions of supercooled liquid water and snow particles, *Mon. Weather Rev.*, 133, 743–751, 2005.
- Lhermitte, R., A 94-GHz Doppler radar for cloud observations, *J. Atmos. Ocean. Technol.*, 4, 3648, 1987.
- Lhermitte, R., Attenuation and scattering of millimeter wavelength radiation by clouds and precipitation, *J. Atmos. Ocean. Technol.*, 7, 464–479, 1990.
- Liao, L., R. Meneghini, T. Iguchi, and A. Detwiler, Use of dual-wavelength radar for snow parameter estimates, *J. Atmos. Ocean. Technol.*, 22, 1494–1506, 2005.
- Liao, L., R. Meneghini, L. Tian, and G. A. Heymsfield, Retrieval of snow and rain from combined X- and W-band airborne radar measurements, *IEEE Trans. Geosci. Remote Sensing*, 46, 1514–1524, 2008.
- Libbrecht, K. G., The physics of snow crystals, *Rep. Prog. Phys.*, 68, 855–895, 2005.
- Liebe, H. J., G. H. Hufford, and T. Manabe, A model for the complex permittivity of water at frequencies below 1 THz, *J. Infrared Mill. Waves*, 12, 659–675, 1991.
- Liljegren, J. C., S. A. Boukabara, K. Cady-Pereira, and S. A. Clough, The effect of the half-width of the 22-GHz water vapor line on retrievals of temperature and water vapor profiles with a 12-channel microwave radiometer, *IEEE Trans. Geosci. Remote Sensing*, 43, 1102–1108, 2005.
- Liu, G., A Database of microwave single-scattering properties for nonspherical ice particles, *Bull. Amer. Meteorol. Soc.*, 89, 1563–1570, 2008a.
- Liu, G., Deriving snow cloud characteristics from CloudSat observations, *J. Geophys. Res.*, 113, D00A09, 2008b.
- Liu, G. S., Approximation of single scattering properties of ice and snow particles for high microwave frequencies, *J. Atmos. Sci.*, 61, 2441–2456, 2004.
- Liu, G. S. and J. A. Curry, Precipitation characteristics in Greenland-Iceland-Norwegian Seas determined by using satellite microwave data, *J. Geophys. Res.*, 102, 13987–13997, 1997.
- Lobl, E. S., K. Aonashi, B. Griffith, C. Kummerow, G. Liu, M. Murakami, and T. Wilheit, Wakasa Bay - An AMSR precipitation validation campaign, *Bull. Amer. Meteorol. Soc.*, 88, 551–, 2007.
- Locatelli, J. D. and P. V. Hobbs, Fall speeds and masses of solid precipitation particles, *J. Geophys. Res.*, 79, 2185–2197, 1974.
- Löffler-Mang, M. and U. Blahak, Estimation of the equivalent radar reflectivity factor from measured snow size spectra, *J. Appl. Meteorol.*, 40, 843–849, 2001.
- Löffler-Mang, M. and J. Joss, An optical disdrometer for measuring size and velocity of hydrometeors, *J. Atmos. Ocean. Technol.*, 17, 130–139, 2000.

- Löffler-Mang, M., M. Kunz, and W. Schmid, On the performance of a low-cost K-band Doppler radar for quantitative rain measurements, *J. Atmos. Ocean. Technol.*, 16, 379–387, 1999.
- Löhnert, U., S. Crewell, C. Simmer, and A. Macke, Profiling cloud liquid water by combining active and passive microwave measurements with cloud model statistics, *J. Atmos. Ocean. Technol.*, 18, 1354–1366, 2001.
- Löhnert, U., S. Kneifel, A. Battaglia, M. Hagen, L. Hirsch, and S. Crewell, A multisensor approach toward a better understanding of snowfall microphysics: The TOSCA project, *Bull. Amer. Meteorol. Soc.*, 92, 613–628, 2011.
- Löhnert, U., D. D. Turner, and S. Crewell, Ground-based temperature and humidity profiling using spectral infrared and microwave observations: Part 1. Retrieval performance in clear sky conditions, *J. Appl. Meteorol. Climatol.*, 48, 1017–1032, 2009.
- Lorenz, L. V., Lysbevaegelsen i og uder en plane lysbolger belyst kugle, *Det Kongelige Danske Videnskabernes Selskabs Skrifter*, 6, 1–62, 1890.
- Lynn, B. H., A. P. Khain, J. Dudhia, D. Rosenfeld, A. Pokrovsky, and A. Seifert, Spectral (Bin) microphysics coupled with a mesoscale model (MM5). Part I: Model description and first results, *Mon. Weather Rev.*, 133, 44–58, 2005.
- Maahn, M., Measuring Precipitation with Micro Rain Radars in Svalbard, Diploma Thesis, Meteorological Institute, Rheinische Friedrich-Wilhelms-Universität Bonn, Bonn, 2010.
- Magono, C. and C. W. Lee, Meteorological classification of natural snow crystals, *Journal of the Faculty of Science, Hokkaido University*, 7, 321–335, 1966.
- Magono, C. and S. Tazawa, Design of snow crystal sondes, *J. Atmos. Sci.*, 23, 618–&, 1966.
- Matrosov, S. Y., Radar reflectivity in snowfall, *IEEE Trans. Geosci. Remote Sensing*, 30, 454–461, 1992.
- Matrosov, S. Y., A dual-wavelength radar method to measure snowfall rate, *J. Appl. Meteorol.*, 37, 1510–1521, 1998.
- Matrosov, S. Y., Modeling backscatter properties of snowfall at millimeter wavelengths, *J. Atmos. Sci.*, 64, 1727–1736, 2007.
- Matrosov, S. Y., A. J. Heymsfield, and Z. Wang, Dual-frequency radar ratio of nonspherical atmospheric hydrometeors, *Geophys. Res. Lett.*, 32, 2005a.
- Matrosov, S. Y., R. F. Reinking, and I. V. Djalalova, Inferring fall attitudes of pristine dendritic crystals from polarimetric radar data, *J. Atmos. Sci.*, 62, 241–250, 2005b.
- Matrosov, S. Y., M. D. Shupe, and I. V. Djalalova, Snowfall retrievals using millimeter-wavelength cloud radars, *J. Appl. Meteorol. Climatol.*, 47, 769–777, 2008.
- Mätzler, C., *Thermal microwave radiation: applications for remote sensing*, Inst. Eng. Technol. London, U.K., 2006, 431–455.

- Mätzler, C., P. W. Rosenkranz, and J. Cermak, Microwave absorption of supercooled clouds and implications for the dielectric properties of water, *J. Geophys. Res.*, 115, D23208, 2010.
- McLinden, M. L., Calibration of the UMASS advanced multi-frequency radar, Masters Thesis, University of Massachusetts, Amherst, 2010.
- Melchionna, S., M. Bauer, and G. Peters, A new algorithm for the extraction of cloud parameters using multiplex analysis of cloud radar data - First application and preliminary results, *Meteorol. Z.*, 17, 613–620, 2008.
- METEK, *MRR Physical Basics*, 2010, Version 5.2.0.3.
- Mie, G., Beiträge zur Optik trüber Medien, speziell kolloidaler Metallösungen, *Annalen der Physik*, 25, 377–445, 1908.
- Mitchell, D. L., R. Zhang, and R. L. Pitter, Mass-dimensional relationships for ice particles and the influence of riming on snowfall rates, *J. Appl. Meteorol.*, 29, 153–163, 1990.
- Muramoto, K., K. Matsuura, and T. Shiina, Measuring the density of snow particles and snowfall rate, *Electron. Commun. Jpn. Pt. III-Fundam. Electron. Sci.*, 78, 71–79, 1995.
- Nešpor, V., W. F. Krajewski, and A. Kruger, Wind-induced error of raindrop distribution measurement using a two-dimensional video disdrometer, *J. Atmos. Ocean. Technol.*, 17, 1483–1492, 2000.
- Noh, Y.-J., G. Liu, A. S. Jones, and T. H. V. Haar, Toward snowfall retrieval over land by combining satellite and in situ measurements, *J. Geophys. Res.*, 114, 2009.
- Noh, Y.-J., G. Liu, E.-K. Seo, J. R. Wang, and K. Aonashi, Development of a snowfall retrieval algorithm at high microwave frequencies, *J. Geophys. Res.*, 111, D22216, 2006.
- Peters, G., B. Fischer, and T. Andersson, Rain observations with a vertically looking Micro Rain Radar (MRR), *Boreal Environment Research*, 7, 353–362, 2002.
- Peters, G., B. Fischer, H. Münster, M. Clemens, and A. Wagner, Profiles of raindrop size distributions as retrieved by microrain radars, *J. Appl. Meteorol.*, 44, 1930–1949, 2005.
- Petty, G. W., Frequencies and Characteristics of global oceanic precipitation from shipboard present-weather reports, *Bull. Amer. Meteorol. Soc.*, 76, 1593–1616, 1995.
- Petty, G. W., Physical and microwave radiative properties of precipitating clouds. Part II: A parametric 1D rain-cloud model for use in microwave radiative transfer simulations, *J. Appl. Meteorol.*, 40, 2115–2129, 2001.
- Petty, G. W., *A First Course in Atmospheric Radiation, Second Edition*, Sundog Publishing, Madison, Wisconsin, 2006.
- Petty, G. W. and W. Huang, Microwave Backscatter and Extinction by Soft Ice Spheres and Complex Snow Aggregates, *J. Atmos. Sci.*, 67, 769–787, 2010.
- Petty, G. W. and W. Huang, The Modified Gamma Size Distribution Applied to Inhomogeneous and Nonspherical Particles: Key Relationships and Conversions, *J. Atmos. Sci.*, 68, 1460–1473, 2011.



- 
- Pruppacher, H. R. and J. D. Klett, *Microphysics of clouds and precipitation*, Kluwer Academic Publishers, 1997, Second Edition.
- Ray, P. S., Broad-band complex refractive indexes of ice and water, *Appl. Optics*, 11, 1836–1844, 1972.
- Reinking, R., S. Matrosov, R. Kropfli, and B. Bartram, Evaluation of a 45 degrees slant quasi-linear radar polarization state for distinguishing drizzle droplets, pristine ice crystals, and less regular ice particles, *J. Atmos. Ocean. Technol.*, 19, 296–321, 2002.
- Reitter, S., K. Fröhlich, A. Seifert, S. Crewell, and M. Mech, Evaluation of ice and snow content in the global numerical weather prediction model GME with CloudSat, *Geoscientific Model Development*, 4, 579–589, 2011.
- Rose, T., S. Crewell, U. Löhnert, and C. Simmer, A network suitable microwave radiometer for operational monitoring of the cloudy atmosphere, *Atmos. Res.*, 75, 183–200, 2005.
- Rosenberg, R., Why is ice slippery?, *Phys. Today*, 58, 50–55, 2005.
- Rosenkranz, P. W., Water vapor microwave continuum absorption: A comparison of measurements and models, *Radio Sci.*, 33, 919–928, 1998.
- Rothman, L. S. and Coauthors, The HITRAN 2008 molecular spectroscopic database, *J. Quant. Spectrosc. Radiat. Transf.*, 110, 533–572, 2009.
- Ryan, B. F., A bulk parameterization of the ice particle size distribution and the optical properties in ice clouds, *J. Atmos. Sci.*, 57, 1436–1451, 2000.
- Seifert, A. and K. D. Beheng, A two-moment cloud microphysics parameterization for mixed-phase clouds. Part 1: Model description, *Meteorol. Atmos. Phys.*, 92, 45–66, 2006.
- Sekelsky, S. M., W. L. Ecklund, J. M. Firda, K. S. Gage, and R. E. McIntosh, Particle size estimation in ice-phase clouds using multifrequency radar reflectivity measurements at 95, 33, and 2.8 GHz, *J. Appl. Meteorol.*, 38, 5–28, 1999.
- Seo, E. K. and G. S. Liu, Retrievals of cloud ice water path by combining ground cloud radar and satellite high-frequency microwave measurements near the ARM SGP site, *J. Geophys. Res.*, 110, D14203, 2005.
- Sevruk, B., M. Ondras, and B. Chvila, The WMO precipitation measurement intercomparisons, *Atmos. Res.*, 92, 376–380, 2009.
- Siebler, D., Bestimmung von Größen- und Formfaktoren von Schnee anhand von Messungen am Schneefernerhaus, Diploma Thesis, Meteorological Institute, Universität München, 2010.
- Skofronick-Jackson, G. M., M. J. Kim, J. A. Weinman, and D. E. Chang, A physical model to determine snowfall over land by microwave radiometry, *IEEE Trans. Geosci. Remote Sensing*, 42, 1047–1058, 2004.

- Skofronick-Jackson, G. M., J. R. Wang, G. M. Heymsfield, R. Hood, W. Manning, R. Meneghini, and J. A. Weinman, Combined radiometer-radar microphysical profile estimations with emphasis on high-frequency brightness temperature observations, *J. Appl. Meteorol.*, 42, 476–487, 2003.
- Smith, P. L. and D. V. Kliche, The bias in moment estimators for parameters of drop size distribution functions: Sampling from exponential distributions, *J. Appl. Meteorol.*, 44, 1195–1205, 2005.
- Stephens, G. L., D. G. Vane, R. J. Boain, G. G. Mace, K. Sassen, Z. E. Wang, A. J. Illingworth, E. J. O'Connor, W. B. Rossow, S. L. Durden, S. D. Miller, R. T. Austin, A. Benedetti, C. Mitrescu, and the CloudSat Science Team, The CloudSat mission and the A-train - A new dimension of space-based observations of clouds and precipitation, *Bull. Amer. Meteorol. Soc.*, 83, 1771–1790, 2002.
- Stogryn, A. P., H. T. Bull, K. Rubayi, and S. Iravanchy, The microwave permittivity of sea and fresh water, Airojet Internal Report, Airojet, Sacramento, Calif., 1995.
- Strauch, R. G., Theory and application of the FM–CW Doppler radar, PhD Thesis, Electrical Engineering, University of Colorado, 1976.
- Su, H., J. H. Jiang, J. Teixeira, A. Gettelman, X. Huang, G. Stephens, D. Vane, and V. S. Perun, Comparison of regime-sorted tropical cloud profiles observed by CloudSat with GEOS5 analyses and two general circulation model simulations, *J. Geophys. Res.*, 116, D09104, 2011.
- Sun, W., Y. Hu, B. Lin, Z. Liu, and G. Videen, The impact of ice cloud particle microphysics on the uncertainty of ice water content retrievals, *J. Quant. Spectrosc. Radiat. Transf.*, 112, 189–196, 2011.
- Surussavadee, C. and D. H. Staelin, Comparison of AMSU millimeter-wave satellite observations, MM5/TBSCAT predicted radiances, and electromagnetic models for hydrometeors, *IEEE Trans. Geosci. Remote Sensing*, 44, 2667–2678, 2006.
- Taflove, A. and S. C. Hagness, *Computational Electrodynamics: The Finite-Difference Time-Domain Method*, Artech House Publishers, 2005.
- Takahashi, T., T. Endoh, G. Wakahama, and N. Fukuta, Vapor diffusional growth of free-falling snow crystals between  $-3^{\circ}\text{C}$  and  $-23^{\circ}\text{C}$ , *J. Meteorol. Soc. Jpn.*, 69, 15–30, 1991.
- Tokay, A., P. Hartmann, A. Battaglia, K. S. Gage, W. L. Clark, and C. R. Williams, A field study of reflectivity and Z–R relations using vertically pointing radars and disdrometers, *J. Atmos. Ocean. Technol.*, 26, 1120–1134, 2009.
- Turner, D. D., U. Löhnert, M. Cadetdu, S. Crewell, and A. Vogelmann, Modifications to the water vapor continuum in the microwave suggested by ground-based 150 GHz observations, *IEEE Trans. Geosci. Remote Sensing*, 47, 3326–3337, doi:10.1109/TGRS.2009.202262, 2009.
- Tyynelä, J., J. Leinonen, D. Moisseev, and T. Nousiainen, Radar backscattering from snowflakes: comparison of fractal, aggregate, and soft-spheroid models, *J. Atmos. Oceanic Technol.*, 2011, [Early Online release].

- Van Baelen, J., F. Tridon, and Y. Pointin, Simultaneous X-band and K-band study of precipitation to derive specific Z-R relationships, *Atmos. Res.*, 94, 596–605, 2009.
- Vavrus, S., The role of terrestrial snow cover in the climate system, *Clim. Dyn.*, 29, 73–88, 2007.
- Waliser, D. E., J. L. F. Li, T. S. L’Ecuyer, and W. T. Chen, The impact of precipitating ice and snow on the radiation balance in global climate models, *Geophys. Res. Lett.*, 38, L06802, 2011.
- Waliser, D. E., J.-L. F. Li, C. P. Woods, R. T. Austin, J. Bachmeister, J. Chern, A. Del Genio, J. H. Jiang, Z. Kuang, H. Meng, P. Minnis, S. Platnick, W. B. Rossow, G. L. Stephens, S. Sun-Mack, W.-K. Tao, A. M. Tompkins, D. G. Vane, C. Walker, and D. Wu, Cloud ice: A climate model challenge with signs and expectations of progress, *J. Geophys. Res.*, 114, D00A21, 2009.
- Warren, S. G. and R. E. Brandt, Optical constants of ice from the ultraviolet to the microwave: A revised compilation, *J. Geophys. Res.*, 113, D14220, 2008.
- Weng, F. Z., L. M. Zhao, R. R. Ferraro, G. Poe, X. F. Li, and N. C. Grody, Advanced microwave sounding unit cloud and precipitation algorithms, *Radio Sci.*, 38, 2003.
- Westbrook, C. D., R. C. Ball, P. R. Field, and A. J. Heymsfield, Universality in snowflake aggregation, *Geophys. Res. Lett.*, 31, L15104, 2004.
- Wiscombe, W. J., Improved Mie scattering algorithms, *Appl. Opt.*, 19, 1505–1509, 1980.
- Woods, C. P., M. T. Stoelinga, and J. D. Locatelli, Size spectra of snow particles measured in wintertime precipitation in the pacific northwest, *J. Atmos. Sci.*, 65, 189–205, 2008.
- Xie, X., U. Löhnert, S. Kneifel, and S. Crewell, Snow particle orientation observed by ground-based microwave radiometry, *J. Geophys. Res.*, 117, D02206, 2011.
- Yan, B., F. Weng, and H. Meng, Retrieval of snow surface microwave emissivity from the advanced microwave sounding unit, *J. Geophys. Res.*, 113, D19206, 2008.
- Yoshida, Y., S. Asano, and K. Iwanami, Retrieval of microphysical properties of water, ice, and mixed-phase clouds using a triple-wavelength radar and microwave radiometer, *J. Meteorol. Soc. Jpn.*, 84, 1005–1031, 2006.
- Zawadzki, I., F. Fabry, and W. Szyrmer, Observations of super-cooled water and secondary ice generation by a vertically pointing X-band Doppler radar, *Atmos. Res.*, 59, 343–359, 2001.
- Zikmunda, J. and G. Vali, Fall patterns and fall velocities of rimed ice crystals, *J. Atmos. Sci.*, 29, 1334–1347, 1972.
- Zink, M., Verbesserte Flüssigwasseralgorithmen durch Kombination passiver Zentimeter- und Millimeterwellenfernerkundung, Diploma Thesis, Meteorological Institute, Universität München, 2010.



# Danksagung

- This work has been funded within the TOSCA project by the German Science Foundation (DFG) under grant LO 901/3-1.
- Ich möchte mich an dieser Stelle bei allen genannten und nicht genannten Personen bedanken die mich während der Doktorarbeit begleitet und unterstützt haben.
- Mein Dank gilt der ganzen Besatzung der UFS für die vielseitige Hilfe während der ganzen TOSCA Kampagne. Ich möchte mich auch bei Herrn Dr. Schönhuber und Herrn Lammer von Joanneum Graz für ihre Hilfe und die Bereitstellung des 2DVD bedanken. Desweiteren gilt mein Dank den anderen Teilnehmern der TOSCA Kampagne, Dr. Martin Hagen (DLR), Dr. Lutz Hirsch (MPI-Hamburge) und Dr. Matthias Wiegner (LMU).
- I am also grateful to Dr. Alessandro Battaglia for many fruitful discussions and comments on my work.
- Ich möchte ganz herzlich den Münchner Kollegen Meinhard Seefeldner und Anton Lex danken, die uns in den letzten Wochen vor Weihnachten so selbstverständlich geholfen haben, den neuen DPR-Blower zum Laufen zu bekommen.
- Max Maahn, Gerhard Peters und Clemens Simmer möchte ich ganz herzlich für die Zusammenarbeit bei dem MRR-Vergleich danken.
- I heartily thank all people that I met during my stay in Madison, WI. I felt very welcome and enjoyed living and working with you. My special thanks go to Ralf Bennartz for inviting me to Madison and to Erin and Tim Wagner for hosting me at their home during that time.
- Liebe Infernos (auch die Ehemaligen), ich hab mich in unserem Gang immer sehr wohl gefühlt und es macht einfach Spaß in einer AG mit solchen Leuten sein zu dürfen!
- Liebe Susanne, ich möchte Dir ganz herzlich dafür danken, dass Du mich nach meiner Diplomarbeit nach Köln “gelockt” hast und stets für meine Anliegen ein offenes Ohr hattest. Auch möchte ich hier gerne noch einmal festhalten, wie dankbar ich Dir für die Möglichkeit bin während der Doktorarbeit neben den vielen interessanten Tagungen nach Madison und in die Antarktis zu fahren.
- Lieber Uli, ohne Dich wäre diese Arbeit sicher nicht möglich gewesen. Ich denke sehr gerne an die vielen Gespräche und Bastel-Stunden nördlich und südlich der Aschaffener Sprachgrenze zurück. Hoffentlich schaffen wir es noch irgendwann einmal nur so zum Spaß und zu Fuß auf die Zugspitze zu gehen, und ein schönes Weißbier auf der Terasse im 5.OG der UFS zu genießen!

- Ganz besonders möchte ich mich bei meiner Familie bedanken. Lieber Papa, Du hast großen Anteil daran, dass sich mein Interesse für Naturwissenschaft entwickelt hat. Ich rechne es Dir sehr hoch an, daß Du mich immer bei meinen Ideen und Vorhaben unterstützt hast, auch wenn Du bereits ahntest, dass einiges davon vielleicht schief gehen wird.
- Liebe Heike, Du hast ganz bestimmt den letzten und damit wichtigsten Platz in dieser Liste verdient. Ohne Deine Liebe, Deine aufbauende und motivierende Art hätte ich so manche schwierige Phasen während der Diss nicht durchgehalten. Natürlich hast Du auch den Hauptanteil daran, dass sich diese Arbeit in lesbares Englisch verwandelt hat und das nach Deinem sowieso schon viel zu langen Klinikarbeitstag. Ich würde ohne Zögern wieder die drei Jahre mit Dir auf den 28  $m^2$  verbringen wollen!

# Erklärung

Ich versichere, dass ich die von mir vorgelegte Dissertation selbständig angefertigt, die benutzten Quellen und Hilfsmittel vollständig angegeben und die Stellen der Arbeit - einschließlich Tabellen, Karten und Abbildungen -, die anderen Werken im Wortlaut oder dem Sinn nach entnommen sind, in jedem Einzelfall als Entlehnung kenntlich gemacht habe; dass diese Dissertation noch keiner anderen Fakultät oder Universität zur Prüfung vorgelegen hat; dass sie - abgesehen von unten angegebenen Teilpublikationen - noch nicht veröffentlicht worden ist sowie, dass ich eine solche Veröffentlichung vor Abschluss des Promotionsverfahrens nicht vornehmen werde. Die Bestimmungen dieser Promotionsordnung sind mir bekannt. Die von mir vorgelegte Dissertation ist von Prof. Dr. S. Crewell betreut worden.

Köln, den 19.09.2011

Stefan Kneifel

## Teilveröffentlichungen

- Kneifel, S., U. Löhnert, A. Battaglia, and S. Crewell, and D. Siebler, Snow scattering signals in ground-based passive microwave radiometer measurements, *J. Geophys. Res.*, 115, D16214, 2010.
- Kneifel, S., M. Maahn, G. Peters, and C. Simmer: Observation of snowfall with a low-power FM-CW K-band radar (Micro Rain Radar), *Meteorol. Atmos. Phys.*, 113, 75–87, 2011.
- Kneifel, S., M. S. Kulie, and R. Bennartz: A triple-frequency approach to retrieve microphysical snowfall parameters, *J. Geophys. Res.*, 116, D11203, 2011.
- Löhnert, U., S. Kneifel, A. Battaglia, M. Hagen, L. Hirsch, and S. Crewell, 2011: A Multisensor Approach Toward a Better Understanding of Snowfall Microphysics: The TOSCA Project. *Bull. Amer. Meteor. Soc.*, 92, 613–628, 2011.





# Lebenslauf

## Angaben zur Person

---

Name, Vorname: Kneifel, Stefan Josef  
Anschrift: Nauheimerstraße 13  
50969 Köln  
Geburtsdatum, -ort: 26.12.1981, Wolfratshausen  
Familienstand: ledig  
Staatsangehörigkeit: deutsch

## Ausbildung

---

1989 – 1992 Grundschule Weidach, Wolfratshausen  
1992 – 2001 Gymnasium Icking, Icking  
Abschluss Allgemeine Hochschulreife (Juni 2001)  
2002 – 2008 Diplomstudium Meteorologie,  
Ludwig-Maximilians-Universität München  
Abschluss Diplom (16.04.2008) Thema: *Modellierung  
und Beobachtung von horizontalen Wasserdampf-  
homogenitäten mit Hilfe von Mikrowellenradiometrie*  
2008 – 2011 Promotionsstudium Meteorologie,  
Universität zu Köln

## Berufliche Tätigkeit

---

06/2001 – 04/2002 Zivildienst beim Bund Naturschutz in Bayern e.V.  
06/2002 – 07/2002 Praktikum, Deutscher Wetterdienst (DWD),  
Hohenpeißenberg, Project: VERTICATOR

09/2002 – 10/2002	Werkstudent, Deutsches Zentrum für Luft- und Raumfahrt: <i>Entwicklung und Aufbau von Feldmühlen zur Beobachtung des elektrstatischen Feldes von Gewittern</i>
11/2004 – 01/2006	Studentische Hilfskraft am Meteorologischen Institut der Universität München im Rahmen des DWD – Projektes: <i>HUBOLA – Comparison of humidity data from the ATOVS and SEVIRI systems with ground-based radiosondes, microwave radiometers and GPS measurements</i> , Scientific Report, DWD, 05/2005
04/2006 – 09/2006	Werkstudent, Universität Bergen, Norwegen: <i>Aufbau und Entwicklung von Sensorik und Datenerfassungssystem zur Beobachtung von Wind, Temperatur und relativer Feuchte mit einem Modellflugzeug.</i>
10/2006 – 05/2008	Studentische Hilfskraft am Meteorologischen Institut der Universität München
seit 05/2008	Wissenschaftlicher Angestellter am Institut für Geophysik und Meteorologie, Universität zu Köln

### **Auszeichnungen**

---

2002	5. Platz beim Bundeswettbewerb Jugend Forscht mit dem Thema: <i>Messung des quasi-statischen atmosphärischen elektrischen Feldes mit Hilfe einer selbst entwickelten Feldmühle.</i>
2008	Best Poster Award, <i>10th Specialist Meeting on Microwave Radiometry and Remote Sensing of the Environment</i> , Florenz, Italien.

Köln, den 19.09.2011